

國立交通大學  
材料科學與工程學研究所  
博士論文

一維氧化鋅奈米結構之製備及其應用  
Synthesis of One Dimensional Zinc Oxide  
Nanostructure and their Applications



研究生：姚奕全

指導教授：曾俊元 博士

林 鵬 博士

中華民國一百零一年四月

一維氧化鋅奈米結構之製備及其應用

**Synthesis of One Dimensional Zinc Oxide Nanostructure and their Applications**

研 究 生：姚奕全

Student : I-Chuan Yao

指 導 教 授：曾俊元 博士

Advisor : Dr. Tseung-Yuen Tseng

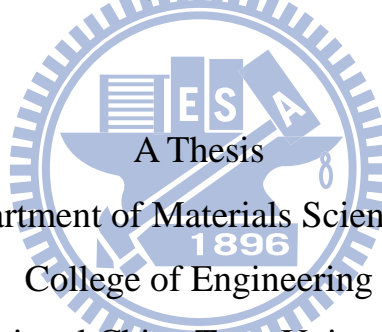
林 鵬 博士

Advisor : Dr. Pang Lin

國立交通大學

材料科學與工程學系

博士論文



Submitted to Department of Materials Science and Engineering  
College of Engineering

National Chiao Tung University

in Partial Fulfillment of the Requirements

for the Degree of

Doctor of Philosophy

in

Materials Science and Engineering

April 2012

Hsinchu, Taiwan, Republic of China

中華民國一百零一年四月

# 一維氧化鋅奈米結構之製備及其應用

研究生：姚奕全

指導教授：曾俊元 博士

指導教授：林 鵬 博士

國立交通大學

材料科學與工程學系博士班

## 摘 要

一維奈米材料由於其卓越的物理與化學特性使其成為近幾年重要之研究領域，在許多一維材料中，氧化鋅由於獨特的光、電及壓電特性而具有廣泛的應用性，成為近年來受矚目的研究方向，於本論文中，我們加入新的製程方法或技術改善一維氧化鋅奈米結構之應用。實驗中，利用掃描式電子顯微鏡(SEM)和穿透式電子顯微鏡(TEM)研究材料之微結構，並使用發光光譜儀(PL)與電流-電壓量測系統分析其光性與電性。本論文依氧化鋅奈米結構之應用與實驗設計分成四部份。第一部分，我們所提出的一個簡單的方法製備氧化鋅奈米尖錐陣列，使奈米尖錐於 25-100 °C 的環境中具備有低的啟動電場、高的場效增益因子與穩定的場發射特性。而優異的場發射特性主要來自於降低氧化鋅發射子本身的氧空缺濃度與小角度的尖錐角度，此簡單的製程方法展現了極大的潛力應用於場發射元件與發光元件上。第二部份，我們所提出的一個有趣的方法來製作氧化鋅-氧化錫核-殼奈米線結構應用於氣體感測器上，此氧化鋅-氧化錫核-殼奈米線具備高的氫氣感測特性，如在溫度 250 °C 時通入 200 ppm 的氫氣其敏感度高達 89%，而高敏感性主要來自於氧化錫膜對於氫氣的完全反應所造成，我們認為利用兩階段成長的方式

所製備的氧化鋅-氧化錫核-殼奈米線具備在氣體感測使用的潛力。第三部份，成功的製備垂直佳且分布均勻的氧化鋅奈米柱於低成本、可撓的聚對苯二甲酸乙二酯(PET)基板上，該元件能夠重複且穩定操作於強度  $25-70 \mu\text{W}/\text{cm}^2$  的紫外光的照射且具備有快的反應時間與回覆時間。此外，元件具備機械可撓性、高可靠度與不同層級的光反應，因而具備有極大的潛力應用於紫外光感測器上。第四部份，成功的製備緻密且均勻的的鎵摻雜氧化鋅奈米柱薄膜/金/鈦/二氧化矽/p-型矽基板的電阻式記憶體元件，此種記憶體元件具備可逆與穩定的操作於開/關狀態間且具備有超過一百次的穩定度特性，而元件的轉態機制主要跟鎵摻雜氧化鋅奈米柱與柱之間的氧空位細絲形成與斷裂有關。結果顯示，此一緻密的鎵摻雜氧化鋅奈米柱薄膜在電阻式記憶體的研究中具備有極高的應用價值。





# Synthesis of One Dimensional Zinc Oxide Nanostructure and their Applications

Student: I-Chuan Yao

Advisor: Dr. Tseung-Yuen Tseng

Advisor: Dr. Pang Lin

Department of Materials Science and Engineering

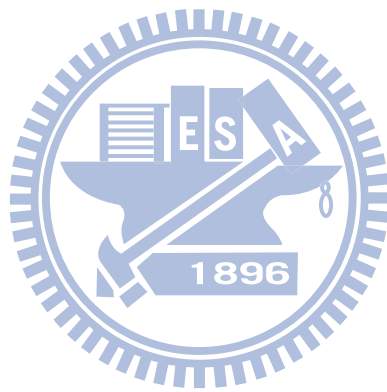
National Chiao Tung University

## ABSTRACT

One-dimensional nanostructures are a new class of advanced materials that have been receiving a lot of research interest in the last decade due to their superior physical and chemical properties. Among one-dimensional materials, zinc oxide (ZnO) is one of the most important materials and has attracted much interest in recent years, due to its unique optical, electrical, and piezoelectric properties and versatile applications. In this dissertation, we propose new methods or technologies to improve the applications of 1D ZnO nanostructure. Macrostructure of the samples was characterized by scanning electron microscopy (SEM) and high resolution transmission electron microscopy (HRTEM). The optical and electrical properties were investigated by photoluminescence (PL) and current–voltage (I–V) characterization. The main focus of this dissertation can be divided into four parts. In first part, we demonstrate a simple method to fabricate ZnO nanotip array, which exhibit low turn-on field, high field enhancement factor and stable field emission properties at 25-100 °C. The good field emission properties are attributed to reduced oxygen vacancy concentration and small tip angle of ZnO emitters, which shows good

potential for developing field emission and light emitting devices. In the second part, we provide another interesting route of fabricating ZnO-SnO<sub>2</sub> core-shell nanowires for gas sensor applications. The ZnO-SnO<sub>2</sub> core-shell nanowires exhibited good hydrogen sensor performance, such as the sensitivity is up to 89% against 200 ppm hydrogen at 250°C. Such high sensitivity was believed to be controlled by the nanoscale SnO<sub>2</sub> layer, which was determined from pinch-off and fully conductive state. The ZnO-SnO<sub>2</sub> core-shell nanostructures made by two-step chemical growth have high potential for gas sensor application. In the third part, vertical well-aligned and uniform ZnO nanorods were successfully prepared on low cost and flexible PET polymer substrate by aqueous solution method under various growth conditions. The photocurrents can be repeatedly and reproducibly switched by modulating UV exposure with power densities of 25-70 μW/cm<sup>2</sup>. The fast response time (100 sec) and rapid recovery time (120 sec) are achieved in UV turn-on/off switching measurements. Owing to the mechanical flexibility, nondestructive properties, high reliability and multilevel photoresponse, the well-aligned ZnO nanorods grown on transparent and flexible PET polymer substrates have high potential for UV photodetector applications. In the fourth part, vertically well-aligned and uniform Ga-doped ZnO (GZO) nanorod thin films were successfully grown on Au/Ti/SiO<sub>2</sub>/p-Si substrates, which used to make resistive switching memory devices. Such memory devices can be reversibly switched between ON and OFF states, with a stable resistance ratio of 10 times, narrow dispersion of ON and OFF voltages, and good endurance performance of over 100 cycles. The resistive switching mechanism in this design is related to the formation and rupture of conducting filaments consisting of oxygen vacancies, occurred at interfaces between GZO nanorods (grain boundaries). Results show that the resulting compact GZO nanorod thin films have a high potential for

resistive memory applications.



# Acknowledgements

時光飛逝，求學的生涯轉眼間就告一段落，回首求學之路，心中沒有不捨，有的只是說不盡的感激與祝福。因人生道路上所經歷的人、事、物的影響與引領，逐步建構出現在與未來的我。

首先衷心地感謝指導教授曾俊元博士，在我求學的過程中所給予的教導和鼓勵，並提供良好的學習環境與自由的空間，使我得以開拓視野學習新知，除了在學識上有所增長之外，對於人生的規劃及待人處事的態度方面，亦受益良多，僅此表達最誠摯的感謝與敬意。另外，也特別感謝另一位指導教授林鵬博士在不同思考邏輯方面的啟發指導，增加我個人的思考層面與研究邏輯，使我能順利完成學業。也感謝百忙之中抽空參加我論文口試的委員們，有了委員們專業的建議與熱心的指導，才能使我的論文更佳的完備。

本篇論文之所以能順利完成，心中最想感謝的人是交大奈米中心的鍾怡娟小姐除了在 TEM 上的教導之外，對於我遭遇困難與煩惱時給予我最大的幫助與建議，著實讓我博士班的生涯中充滿許多能量與衝勁，對於妳的幫助心中充滿無限的感謝之意；另外也要感謝交大奈米科技中心提供了一流的分析儀器與充滿歡笑的研究團隊：劉翊筑小姐、李良箴小姐、賴良一先生與徐武達先生，有你們的陪伴真的讓我的求學生涯中充滿了許多的歡笑與回憶。

此外，感謝 TTY LAB 與材料所的學長、同學與學弟妹在生活上與研究上的協助，令我在交通大學的學生生活更加地豐富。群傑、志洋、孟漢學長與岱螢同學在研究上的經驗與日常生活中的相處使我受惠良多；材料所的國璋、峻彥、雲閔學長與伊茹學姐在實驗的討論與教導令我能更順利進行相關研究；博班的崇榮、文碩與駿揚學弟希望你們多加把勁，早日聽到你們的好消息；TTY LAB 的宏全、啟翔、志文、昱廷、盈賢、政漢、聖和與佑書等碩士班學弟妹們，求學生涯中你們的陪伴都是我最珍貴的回憶；材料所的車牧龍、謙昱涵、徐明義、王智、涂弘恩、李孝謙、許書豪、蔡沁穎、陳奎岳、胡勝翔及邱維剛等球友們，在生活中所

帶給我的歡笑與陪伴，我都銘記在心，也衷心的祝福你們凡事順利、心想事成，並願我們的友誼長存。同時也要感謝所有曾經幫助及關心我的朋友們，謝謝你們的幫忙。

再者感謝交大奈米中心所提供設備與服務。其中特別感謝陳聯珠、鄭淑娟與劉悅恩小姐在量測與材料分析技術上所提供的服務與討論，以及行政人員何惟梅小姐在行政事務上的協助。另外也要感謝國科會在研究計畫經費上的補助。

最後我要感謝我父母—姚錫勳先生與姚黃麗卿女士，因為你們多年來的辛苦教導與栽培才能有今天的我，讓我無生活上的負擔與壓力，能專心地完成學業。也感謝哥哥—姚鈞譯，無時無刻地給予我溫暖的關懷，讓我在灰心與氣餒的時候不被眼前的困難所打倒。相信我對於自己的未來，會繼續保持的好奇心與努力，創造出屬於自己的一片天空。

謹以此論文獻給所有在人生道路上幫助過我的人



姚奕全 壬辰 春  
於 風城 交通大學

# Contents

<b>Abstract (in Chinese)</b> .....	i
<b>Abstract (in English)</b> .....	iii
<b>Acknowledgments</b> .....	vi
<b>Contents</b> .....	viii
<b>Table Lists</b> .....	xii
<b>Figure Captions</b> .....	xiii

## Chapter 1 Introduction

1-1. Nanosturcture and nanotechnology.....	1
1-2. ZnO material characteristics.....	2
1-3. Synthesis of zinc oxide nanostructures.....	4
1-3-1 Vapor-liquid-solid method.....	4
1-3-2 Aqueous solution (Hydrothermal) growth method	6
1-3-3 Electrodeposition growth method.....	7
1-4. Properties, potential applications of ZnO nanorod arrays	8
1-4-1 Field emission properties.....	9
1-4-2 Gas sensor and ultraviolet photodetectors.....	12
1-4-3 Resistive random access memory (RRAM).....	14
1-5. Optical properties of zinc oxide.....	17
1-6. Outline of dissertation	17

## Chapter 2 Nano Tip Fabrication of Zinc Oxide Nanorods and their Enhanced Field Emission Properties

2-1.	Introduction.....	29
2-2.	Experimental method.....	30
2-3.	Results and discussion.....	31
2-3-1	Morphology and crystalline of ZnO seed layer.....	31
2-3-2	Morphology and crystalline of ZnO nanorod structure.....	31
2-3-3	Field emission properties.....	33
2-4.	Conclusions.....	35

### **Chapter 3 Electrical Properties and Reliability of ZnO-based Nanorod Current Emitters**

3-1.	Introduction.....	43
3-2.	Experimental method.....	44
3-3.	Results and discussion.....	45
3-3-1	Morphology, crystal structure, composition and optical properties of ZnO nanorod array.....	45
3-3-2	Field emission properties.....	48
3-4.	Conclusions.....	50

### **Chapter 4 Field Emission Properties and Reliability of ZnO Nanorod, Nanopagoda, and Nanotip Current Emitters**

4-1.	Introduction.....	57
4-2.	Experimental method.....	58
4-3.	Results and discussion.....	59
4-3-1	Morphology, crystal structure, composition and optical properties of ZnO nanorod, nanopagoda and nanotip array.....	59

4-3-2	Field emission properties.....	61
4-4.	Conclusions.....	64

**Chapter 5 Hydrogen Gas Sensors using ZnO-SnO<sub>2</sub> Core-Shell Nanostructure**

5-1.	Introduction.....	71
5-2.	Experimental method.....	72
5-3.	Results and discussion.....	73
5-3-1	Crystal structure, morphology and chemical composition of as-grown ZnO and ZnO-SnO <sub>2</sub> core-shell nanowires.....	73
5-3-2	Gas sensing properties of as-grown ZnO and ZnO-SnO <sub>2</sub> core-shell nanowires.....	75
5-4.	Conclusions.....	77

**Chapter 6 ZnO Nanorods Grown on Polymer Substrates as UV Photodetectors**

6-1.	Introduction.....	85
6-2.	Experimental method.....	86
6-3.	Results and discussion.....	87
6-3-1	Morphology, crystal structure, composition and optical properties of ZnO nanorod array.....	87
6-3-2	UV sensing properties of ZnO nanorods.....	88
6-4.	Conclusions.....	91

**Chapter 7 Fabrication and Resistive Switching Characteristics of High Compact Ga-Doped ZnO Nanorod Thin Film Devices**



7-1.	Introduction.....	101
7-2.	Experimental method.....	102
7-3.	Results and discussion.....	103
	7-3-1 Morphology and crystalline structure.....	103
	7-3-2 Resistive switching properties.....	105
7-4.	Conclusions.....	109
	<b>Chapter 8 Summary and Conclusions.....</b>	<b>123</b>
	<b>Chapter 9 Future Works.....</b>	<b>127</b>
	<b>References.....</b>	<b>130</b>
	<b>Vita.....</b>	<b>150</b>
	<b>Publication Lists.....</b>	<b>152</b>



## Table Lists

### Chapter 1

<b>Table 1.1</b>	Properties of zinc oxide (ZnO) material.....	19
<b>Table 1.2</b>	Summary of different methods for aqueous solution growth.....	19
<b>Table 1.3</b>	The comparison with the Flash memory and next-generation NVM candidates.....	20

### Chapter 6

<b>Table 6.1</b>	Comparison of photodetector characteristic for various ZnO nanostructures.....	93
------------------	--	----

### Chapter 7

<b>Table 7.1</b>	Relationship of Ga/Zn molar ratio in solution, pH of the solution and real Ga/Zn atomic ratio in GZO nanorod.....	111
<b>Table 7.2</b>	Comparison of RS characteristic for various ZnO nanostructure devices.....	112

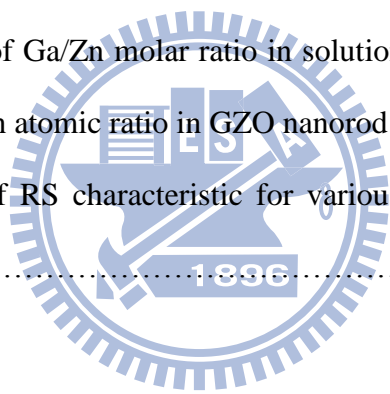


## Figure Captions

### Chapter 1

<b>Figure 1.1</b>	The scale of nanoscale.....	21
<b>Figure 1.2</b>	The dimensionality of confinement and its effects on the density of states.....	21
<b>Figure 1.3</b>	The wurtzite structure model of ZnO.....	22
<b>Figure 1.4</b>	SEM images of various ZnO nanostructures.....	22
<b>Figure 1.5</b>	SEM images of various ZnO nanostructures.....	23
<b>Figure 1.6</b>	Diffusion models for the source atoms to the growth front of the nanowires: (a) classical VLS with diffusion through a liquid seed, (b) a partially molten particle with liquid surface and interface and solid core and (c) a solid growth seed with a liquid particle wire interface and additional surface diffusion area.....	23
<b>Figure 1.7</b>	Aqueous solution growth mechanism of ZnO nanorods.....	24
<b>Figure 1.8</b>	(a) Field emission of electrons from metal or semiconductor surfaces. (b) Band diagram of a semiconductor field-emitter under biasing.....	24
<b>Figure 1.9</b>	Schematic diagram of charge carrier concentration in gas sensor	25
<b>Figure 1.10</b>	(a) Schematic of a ZnO nanoparticle film device structure. (b) Current versus voltage for a ZnO nanoparticle film device in the dark and under 0.83 mW/cm <sup>2</sup> illumination at 370 nm.....	25
<b>Figure 1.11</b>	The typical <i>I-V</i> curve of unipolar resistive switching. LRS and HRS are switched by applying the same voltage polarity but the amplitude of the turn-off voltage is always smaller than that of the turn-on voltage.....	26

<b>Figure 1.12</b>	The typical <i>I-V</i> curves of bipolar resistive switching. The turn-on process occurs on one voltage polarity while the turn-off process is triggered by the opposite voltage polarity.....	26
<b>Figure 1.13</b>	The typical <i>I-V</i> curve of nonpolar resistive switching. The amplitude of the turn-on voltage is always higher than the voltage at which the turn-off process occurs.....	27
<b>Figure 1.14</b>	Optical spectrums.....	28
<b>Figure 1.15</b>	Mechanism of ultraviolet and visible emission.....	28
<b>Chapter 2</b>		
<b>Figure 2.1</b>	The XRD patterns of ZnO seed layer which is annealed at different temperature.....	36
<b>Figure 2.2</b>	The SEM images of annealed ZnO seed layer on Si substrate. (a) Top and (b) cross view.....	36
<b>Figure 2.3</b>	Typical SEM images of (a) as-grown ZnO nanorods and (b) 2h chemical etching nanorods (inset: cross section images).....	37
<b>Figure 2.4</b>	Typical SEM images of (a) the ZnO nanorods after plasma etching and (b) the ZnO nanorods after two-step etching.....	37
<b>Figure 2.5</b>	Schematic illustration of the two-step etching process.....	38
<b>Figure 2.6</b>	Cross section TEM image and EDS spectrum of Si, ZnO seed layer, and as-grown ZnO nanorods.....	39
<b>Figure 2.7</b>	HR-TEM images and FET patterns of Si, ZnO seed layer, and as-grown ZnO nanorods.....	40
<b>Figure 2.8</b>	TEM image of the single ZnO nanorod after plasma etching, the insets show the corresponding SAED pattern and high resolution TEM image.....	41

<b>Figure 2.9</b>	(a) J-E curves (inset is F-N plots) and (b) Stability test of the nanorod emitters.....	42
-------------------	---	----

**Chapter 3**

<b>Figure 3.1</b>	Typical FE-SEM images of ZnO nanorod with various oxygen plasma treatment times (a) 0 s (as-grown), (b) 30 s, (c) 60 s and (g) 120 s. respectively.....	51
-------------------	---	----

<b>Figure 3.2</b>	(a) XRD analysis of ZnO nanorod emitters with the various oxygen plasma etching times. (b) TEM bright field image, corresponding SAED pattern, HR-TEM image and (c) EDS analysis of as-grown ZnO nanorod after 60 s oxygen plasma etching.....	52
-------------------	--	----

<b>Figure 3.3</b>	Room temperature PL spectra of ZnO nanorod emitters with the various oxygen plasma etching times (inset show magnify of green emission areas).....	53
-------------------	--	----

<b>Figure 3.4</b>	(a) J-E curves and (b) F-N plots of ZnO nanorod emitters with various oxygen plasma treatment times.....	54
-------------------	--	----

<b>Figure 3.5</b>	Stability at 25 °C of ZnO nanorodwith oxygen plasma etching for 60 s: (a) Turn-on and threshold fields, (b) Field emission enhanced factor, (c) 1 <sup>st</sup> , 100 <sup>th</sup> , 200 <sup>th</sup> and 400 <sup>th</sup> cycle respective J-E curves and (d) FE-SEM images of tip structured ZnO nanorod emitters for stability tests.....	55
-------------------	---	----

<b>Figure 3.6</b>	Stability at various temperatures of tip structure ZnO nanorod emitters: (a) J-E curves, (b) Turn-on and threshold fields and (c) Field emission enhancement factor.....	56
-------------------	--	----

**Chapter 4**

<b>Figure 4.1</b>	(a) XRD analysis of ZnO nanorod, nanopagoda, and nanotip emitters. Typical FE-SEM images of (b) nanorod, (c) nanopagoda, and (d) nanotip emitters; (insets of (b), (c) and (d) are their top view images) .....	65
<b>Figure 4.2</b>	Schematic descriptions of the formations of ZnO nanopagoda and nanotip emitters.....	66
<b>Figure 4.3</b>	TEM cross section images, corresponding SAED patterns and HR-TEM images of (a) ZnO nanopagoda and (b) ZnO nanotip emitters.....	67
<b>Figure 4.4</b>	Room temperature PL spectra of ZnO nanorod, nanopagoda, and nanotip emitters.....	68
<b>Figure 4.5</b>	(a) J-E curves (inset shows the F-N plots) of ZnO nanorod, nanopagoda, and nanotip emitters. (b) Stability at room temperature of ZnO nanopagoda and nanotip emitters.....	69
<b>Figure 4.6</b>	Stability at various temperatures of ZnO naontip emitters: (a) J-E curves and (b) turn-on and threshold fields.....	70
 <b>Chapter 5</b>		
<b>Figure 5.1</b>	Typical FE-SEM images of (a) as-grown ZnO nanowires, (b) ZnO-SnO <sub>2</sub> -5, (c) ZnO-SnO <sub>2</sub> -10 and (d) ZnO-SnO <sub>2</sub> -20 core-shell nanowires; (insets of (a), (b), (c) and (d): a side images of as-grown and core-shell nanowires.....	79
<b>Figure 5.2</b>	TEM bright field image, EDS analysis and SAED pattern of the (a) as-grown ZnO nanowire and (b) ZnO-SnO <sub>2</sub> -20 core-shell nanowire.....	80
<b>Figure 5.3</b>	HRTEM images of (a) As-grown ZnO nanowires, (b)	

	ZnO-SnO <sub>2</sub> -5, (c) ZnO-SnO <sub>2</sub> -10 and (d) ZnO-SnO <sub>2</sub> -20 core-shell nanowires. ....	81
<b>Figure 5.4</b>	XPS Spectra of as-grown ZnO and ZnO-SnO <sub>2</sub> core-shell nanowires, (a) Zn spectrum, (b) O spectrum and (c) Sn spectrum	82
<b>Figure 5.5</b>	Dynamic response of (a) as-grown ZnO nanowires, (b) ZnO-SnO <sub>2</sub> -5, (c) ZnO-SnO <sub>2</sub> -10 and (d) ZnO-SnO <sub>2</sub> -20 core-shell nanowire sensors at 250 °C .....	83
<b>Figure 5.6</b>	Plots of sensitivity versus hydrogen concentration at 250 °C of the ZnO-SnO <sub>2</sub> core-shell nanowires.....	84
<b>Chapter 6</b>		
<b>Figure 6.1</b>	Schematic structure of ZnO nanorod photodetector.....	94
<b>Figure 6.2</b>	Typical FE-SEM images of (a) ZnO-60, (b) ZnO-30, (b) ZnO-20 and (d) ZnO-10 nanorods, respectively.....	95
<b>Figure 6.3</b>	(a) XRD patterns and (b) PL spectra of the ZnO nanorods with various growth times. Inset is the ratios of UV emission to visible light emission as a function of growth time.....	96
<b>Figure 6.4</b>	(a) TEM bright image and (b) EDS analysis of the ZnO-10 nanorod. Inset is the SAED pattern and HRTEM image of the ZnO-10 nanorod. ....	97
<b>Figure 6.5</b>	(a) Low magnification SEM image of high bent ZnO-10/PET structure (b) convex and (c) concave geometric side views and (d) I-V characteristics measured at different bending morphologies.....	98
<b>Figure 6.6</b>	UV photodetective properties (a) I-V plot of ZnO-10 nanorods in the dark environment and under UV illumination (365 nm)	

with power densities of 25, 35 and 70  $\mu\text{W}/\text{cm}^2$ , respectively. (b) Reversible switching properties of ZnO-10 nanorods. (c) Sensitivity vs time plots under 100 sec illuminations of ZnO nanorods grown with various times at power density of 25  $\mu\text{W}/\text{cm}^2$ . (d) Sensitivity vs growth time curves of the nanorods at 0.5 V bias under 100 sec illuminations. (e) Sensitivity vs time plots of longer (ZnO-60) and shorter (ZnO-10) nanorod photodetectors under longer time illumination..... 99

**Figure 6.7** Stability measurements of ZnO-10/ PET photodetector: (a) different orientation UV illumination (b) retention properties, (c) stability characteristics at UV power density of 25  $\mu\text{W}/\text{cm}^2$  and (d) Multilevel photoresponse performed by various UV power density illuminations..... 100

## Chapter 7

**Figure 7.1** Schematic structure of the Au/GZO nanorod thin films/ ZnO/Au device structure..... 113

**Figure 7.2** Typical FE-SEM cross sectional images of (a) Device 1, (b) Device 2, (c) Device 3 and (d) Device 4; (insets of (a)-(d) are top view of the Devices 1, 2, 3, and 4, respectively)..... 114

**Figure 7.3** (a) XRD analysis and (b) a-axis and c-axis lattice parameters of the GZO nanorod thin films with various Ga/Zn molar ratios in the solutions..... 115

**Figure 7.4** (a) TEM bright field image of Device 4 (the inset is EDS analyzed result of the point indicated) and (b) EDS element line profiles of Device 4..... 116



<b>Figure 7.5</b>	Photoluminescence spectra of the Devices 1, 2, 3, and 4.....	117
<b>Figure 7.6</b>	(a) and (b) Typical bipolar RS I-V curve of Device 4. (c) The yield of the Device 2, 3, and 4, respectively.....	118
<b>Figure 7.7</b>	(a) Pattern size dependence of the resistance value in the ON and OFF states. (b)-(d) Schematic diagrams of bipolar RS mechanism of GZO nanorod film devices through the formation/rupture of conducting filaments formed between GZO nanorod side wall and ZnO seed layer.....	119
<b>Figure 7.8</b>	Endurance cycle plots of $V_{ON}$ and $V_{OFF}$ of Devices (a) 2, (b) 3, and (c) 4.....	120
<b>Figure 7.9</b>	Endurance cycle plots of the ON and OFF resistances of Devices (a) 2, (b) 3, and (c) 4.....	121
<b>Figure 7.10</b>	Dynamic pulse-induced resistive switching of Device 4. Applying a $-8\text{ V } 1\mu\text{s}$ to switch the memory state to ON state and applying a $+6\text{ V } 1\mu\text{s}$ pulse to switch it back to the OFF state.....	122
<b>Chapter 9</b>		
<b>Figure 9.1</b>	The illustration of the new ZnO nanotip field emission device....	128
<b>Figure 9.2</b>	The schematic illustration of the metal oxide/GZO nanorods double layer RRAM device.....	128
<b>Figure 9.3</b>	The schematic illustration of the single ZnO nanowire device.....	129

# Chapter 1

## Introduction

### 1-1. Nanosturcture and nanotechnology

Nanostructures, which are defined with at least on dimension is smaller than one micrometer ( $\mu\text{ m}$ ), normally between 1-100 nanometer (nm), have been given a lot of attention due to their new physical and chemical properties superior to those of their bulk materials. Figure 1.1 gives a size of nanoscale objects and phenomenon a compared with the size of small everyday objects, feeling for the nano-world in natural <sup>[1.1]</sup>. Nanotechnology deals with small structures from sub-nanometer to several hundred nanometers. Generally, the nanotechnology is a technology of fabrication and applications of nanomaterials. Nanoscience not only includes fundamental understanding of physical and chemical properties of nanomaterials but also discussion the fundamental relationships between properties, phenomena and dimensions in the nanometer scale. It is widely felt that nanoscience will lead to the next industrial revolution.

Figure 1.2 indicates the nano-dimension and the corresponding density of states of nano and bulk material <sup>[1.2]</sup>. Nanomaterials and nanostructures can be defined as zero-dimensional (0D) (nanodots and quantum dots), one-dimensional (1D) (nanowires, nanotubes and nanorods), and two-dimensional (2D) (nanobelts and nanosheets) systems in which at least one dimension is smaller 100 nm.

0D nanomaterials have been extensively studied because of the confinements in all three dimensions. A large number of physical and chemical methods have been developed to fabricate 0D nanomaterials with controlled size and pattern from a rich variety of materials <sup>[1.3-1.4]</sup>. Many progresses has been made not only in size dependent

physical and chemical properties but also in fabricating devices using 0D nanomaterials as key components, such as sensor, nanodot lasers and biological detectors <sup>[1.5-1.7]</sup>.

1D nanomaterials includes nanowires, nanotubes, nanofibers, and nanorods have attracted much attention <sup>[1.8-1.9]</sup>. Nanowires and nanorods are the main issues and have attracted marvelous interest over the past years. The nanowire and nanorod provides ideal structures for studying transport processes of one-dimension confined objects and related fundamental phenomena, and they also developing new generation nanodevices with high performance in the future <sup>[1.10]</sup>. In comparison with 0D and 2D nanomaterials, 1D nanomaterials provide a better model system for investing the dependence of electrical and optoelectronic properties on size reduction and dimensionality. Nanowires and nanorods are a new class of quasi 1D nanomaterials that have been attracting great research interest in the past few years and their superior electrical, mechanical, optical and thermal properties permit them to be used as fundamental building blocks for nanoscale science and technology in fields of electronic devices, such as gas sensor, field emission emitters and photodetector <sup>[1.11-1.13]</sup>.

## **1-2. ZnO material characteristics**

Zinc oxide (ZnO) is a II-VI group semiconductor, has a stable wurtzite structure (P6<sub>3</sub>mc space group) with lattice spacing  $a=0.325$  nm and  $c=0.521$  nm with a  $c/a$  ratio of 1.633 as shown in Figure 1.3 <sup>[1.8]</sup>. It is composed of a number of alternating planes with tetrahedrally-coordinated  $O^{2-}$  and  $Zn^{2+}$  ions, stacked alternately along the  $c$ -axis. Along the  $c$ -axis, the positively charged Zn-(0001) polar surface and negative charged O-(000 $\bar{1}$ ) polar surface are the strongest polarity surfaces. The polar surfaces

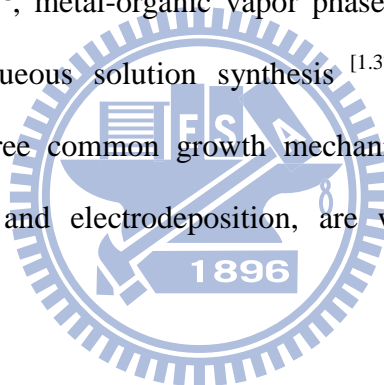
contribute to the variety of ZnO nanostructures by surface reconstruction to maintain a stable structure. ZnO material exhibits high melting temperature (1975°C), high thermal stability and their specific heat is 0.125 cal/gm. ZnO materials with great potential for a variety of practical applications, such as piezoelectric transducers, optical waveguides, surface acoustic wave devices, transparent conductive oxides, chemical sensors, and UV-light emitters<sup>[1.14-1.16]</sup>. ZnO is a wide direct bandgap (~3.37 eV at room temperature) compound semiconductor that is suitable for photonic applications in the UV or blue spectral range. The high exciton-binding energy (60 meV) allows efficient excitonic emission even at room temperature<sup>[1.8]</sup>. In addition, ZnO doped with transition metals shows great promise for spintronic applications. It has also been suggested that ZnO exhibits sensitivity to various gas species, namely ethanol (C<sub>2</sub>H<sub>5</sub>OH), carbon monoxide (CO) and hydrogen (H<sub>2</sub>), which makes it suitable for sensing applications<sup>[1.17]</sup>. Moreover, its piezoelectric (originating from non-centrosymmetric structure) property makes it suitable for electromechanical sensor or actuator applications. The properties of ZnO are listed at Table 1.1<sup>[1.18]</sup>. Last but not least, ZnO is a chemically stable and environmentally friendly materials and considerable interest in studying ZnO in the form of powders, single crystals, films, or nanostructures.

A variety of ZnO nanostructure morphologies, such as nanowires<sup>[1.19-1.21]</sup>, nanorods<sup>[1.22-1.24]</sup>, tetrapods<sup>[1.25-1.26]</sup>, and nanoribbons/belts<sup>[1.27-1.28]</sup>, have been reported. ZnO nanostructures have been fabricated by various methods, such as thermal evaporation<sup>[1.29-1.32]</sup>, metal–organic vapor phase epitaxy (MOVPE)<sup>[1.33-1.34]</sup>, laser ablation<sup>[1.35-1.36]</sup>, hydrothermal (aqueous solution) synthesis<sup>[1.37-1.40]</sup>, and template-based synthesis<sup>[1.41]</sup>. Recently, novel morphologies such as hierarchical nanostructures, bridge-/nail-like nanostructures, tubular nanostructures, nanosheets, nanopropeller arrays, nanohelices and nano-rings have, amongst others, been

demonstrated. Some of the possible ZnO nanostructure morphologies are shown in Figures 1.4 and 1.5<sup>[1.42-1.43]</sup>. The growth and properties of ZnO nanostructures have been extensively studied, but there are still a number of unanswered questions concerning the relationship between fabrication conditions and optical properties.

### **1-3. Synthesis of zinc oxide nanostructures**

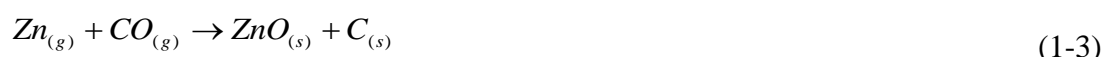
ZnO has probably the richest variety of different nanostructures. Its range includes highly ordered nanowires<sup>[1.19-1.21]</sup>, nanorods<sup>[1.22-1.24]</sup>, nanobelts<sup>[1.44-1.45]</sup>, nanotubes<sup>[1.46-1.47]</sup>, nanohelices<sup>[1.48-1.49]</sup>, and nanorings<sup>[1.50-1.51]</sup> as shown in Figure 1.4 and 1.5. ZnO nanostructures have been fabricated by various methods, such as thermal evaporation<sup>[1.29-1.32]</sup>, metal-organic vapor phase epitaxy (MOVPE)<sup>[1.33-1.34]</sup>, laser ablation<sup>[1.35-1.36]</sup>, aqueous solution synthesis<sup>[1.37-1.40]</sup> and electrodeposition<sup>[1.52-1.53]</sup>. Among them, three common growth mechanisms, vapor growth (VLS), aqueous solution growth and electrodeposition, are well established and detail described as follow.



#### ***1-3-1 Vapor-liquid-solid method***

The VLS growth mechanism was first proposed by Wagner and Ellis in 1964 for Si whisker by hydrogen reduction of  $\text{SiCl}_4$ . The growth mechanism including three main steps: the formation of the small liquid droplet, nucleation and growth of the nanorods, as shown in Figure 1.6<sup>[1.54-1.55]</sup>. In the case of ZnO nanostructures, the thermal evaporation process is realized in a horizontal tube furnace with at least 2 temperature zones. Metal Zn or ZnO powder and graphite are mixed appropriately and load into an alumina boat, and then the boat is placed in the high temperature zone of the furnace under gas flow. As the temperature is increased to the reactive temperature (800-1000 °C), the ZnO reacts with graphite to form Zn and CO vapor

(equation (1-1)-(1-2)), the gaseous would and condense on the catalyst (low temperature zone) such as Au, Sn and Cu particles <sup>[1.56-1.57]</sup>. The nucleation is starting and the single crystalline ZnO nanorods grow by the equation (1-3)-(1-4) <sup>[1.58-1.59]</sup> :



There are several processing parameters such as temperature, pressure, carrier gas (including gas species and its flow rate), substrate and evaporation time period, which can be controlled and need to be selected properly before and/or during the thermal vaporization <sup>[1.60]</sup>. The source temperature selection mainly depends on the volatility of the source material. Usually, it is slightly lower than the melting point of the source material. The pressure is determined according to the evaporation rate or vapor pressure of the source material. The substrate temperature usually drops with the distance of its location from the position of the source material. The local temperature determines the type of product that will be obtained. Based on above conditions, the high aspect ratio and large-scale arrays with vertically aligned nanostructure have been produced by this method <sup>[1.61]</sup>.

In additions, some groups have reported combination the VLS and template to synthesis the highly aligned and uniform density ZnO nanorod arrays <sup>[1.41, 1.62]</sup>. For template materials, anodic aluminum oxide (AAO) is the most popular and highest efficient candidate. The AAO occupied hexagonal ordered porous structure with the porous diameter ranging from 10-200 nm, porous density in the range  $10^{10}$ - $10^{20}$  /cm<sup>2</sup>, and high aspect ratio of the channel, which is difficult to achieve with conventional

lithography technology.

### ***1-3-2 Aqueous solution (Hydrothermal) growth method***

Aqueous solution growth method is a cheapest method to synthesize ZnO nanorods and has been developed to produce functionalized thin films and coating of metal oxide materials on various substrates, such as single crystalline, polycrystalline and plastic substrates. This method does not require any template or epitaxial substrate to control their orientation and it have many advantages over other growth methods such as low cost, environmental friendliness, catalyst-free, large-scale production and low reaction temperature <sup>[1.63-1.65]</sup>.

The synthesis involves the hydrolysis-condensation of hydrated metal ions and complexes and their heteronucleation onto substrates. Experimentally, the aqueous solution growth simply consists of heating an aqueous solution of metal precursors (salts or complexes) at a given ionic pH, in the presence of substrates at mild temperatures (below 100 °C). Therefore, such method does not require expensive and complicated equipment. It is entirely recyclable, safe and environmental-friendly, since only water is used as solvent. In addition, since no organic solvents are present, the purity of the as-prepared thin films is substantially improved. The residual salts are easily washed out by water due to their high solubility <sup>[1.64]</sup>.

Verges et al. report the aqueous solution growth method for the first time in 1990 <sup>[1.66]</sup> and Greene et al. demonstrated a seeded growth process that was used to synthesize ZnO nanowire arrays in water scale production <sup>[1.67]</sup>. Recently, there are extensive reports on fabrication of different nanostructures by aqueous solution growth method, such as nanorods <sup>[1.38]</sup>, nanoflowers <sup>[1.68]</sup>, nanoneedles <sup>[1.69]</sup>, nanotubes <sup>[1.70]</sup>, and nanoplates <sup>[1.71]</sup>. Previous works of aqueous solution growth were focused on controlling the reaction, concentration of solution, different pH value and synthesis

different morphology. The Table 1.2 summarizes some of aqueous solution growth method and the resulting structures<sup>[1.72-1.75]</sup>. Based on the above result, the growth solution usually use the zinc nitrate hexahydrate ( $Zn(NO)_3 \cdot 6H_2O$ ) and the hexamethylenetetramine (HMT,  $C_6H_{12}N_4$ ) in a vessel. The zinc nitrate hexahydrate which is used as source of zinc and HMT is used to control the pH value. The aqueous solution growth method can be shown in Figure 1.7. These can be represented by the following reactions<sup>[1.63, 1.76-1.78]</sup> :



The aqueous solution method is based on the formation of solid phase from a solution, which involves two steps about nucleation and growth. In the nucleation, the clusters of molecules are formed undergo rapid decomposition and particles combine to grow up to a certain thickness of the film by heterogeneous reactions on the substrate surface. When zinc nitrate tetrahydrate and HMT are mixed together, no precipitation accrues initially. With the increase of reaction temperature, the HMT begins to decompose into ammonia and the  $Zn(OH)_2$  occurs. For the solution is heated, ZnO nuclei are formed on the substrate. As soon as the ZnO nuclei are formed, the ZnO nanorods begin to grow. This synthesis of ZnO nanorods without catalysts or templates provides a promising option for the large-scale production of well-dispersed one-dimension nanostructure materials.

### ***1-3-3 Electrodeposition growth method***

Electrodeposition is another method used to achieve ZnO nanostructures<sup>[1.52-1.53]</sup>.



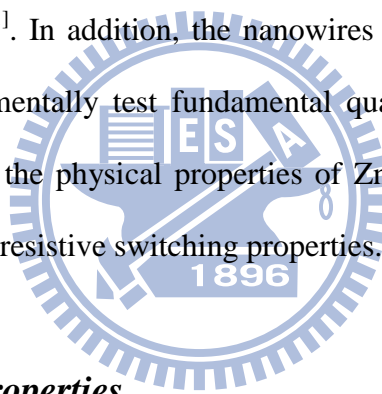
Various groups have used the F-doped SnO<sub>2</sub> (FTO), Sn-doped In<sub>2</sub>O<sub>3</sub> (ITO), and Zn foil substrates to prepare the ZnO nanostructures and by controlling the electrodeposition parameters, such as solution temperature, current density, and deposition time can formation different morphology of ZnO nanostructures<sup>[1.79-1.81]</sup>. Other groups have reported electrodeposition of thin films and indicate that more positive electrodeposition potentials favor high-quality film growth and additional annealing results in significant enhancement and sharpening of the excitonic emission bands<sup>[1.82]</sup>. Wong *et al.* have shown the influence of the substrate surface on the nucleation of nanorods. Electropolishing of Zn foil prior to electrodeposition hinders the nucleation of nanorods. Nonelectropolished films show much narrower and denser growth of ZnO nanorods. The groups conclude that a native surface oxide enhances nucleation<sup>[1.81]</sup>.

In additions, some groups have reported combination the electrodeposition and template to synthesis the uniform density ZnO nanostructures. Liu et al. used electrodeposition and polystyrene (PS) array to synthesis the order-porous ZnO films on Sn-doped In-oxide (ITO) glass substrates and the process. This template is created by self-assembly of an ordered PS array from a suspension of PS spheres and then the ZnO is electrodeposited into the pores of this array. After dissolution of the PS matrix, a stable porous ZnO film is fabricated<sup>[1.83]</sup>. Le et al. synthesis ordered nanowires uses anodic alumina templates. ZnO nanowires are electrodeposited with diameters of 15-90 nm into the pores of the alumina template and oxidized to ZnO in air at 300 °C<sup>[1.84]</sup>.

#### **1-4. Properties, potential applications of ZnO nanorod arrays**

Nanostructures can be defined as systems in which at least one dimension is smaller than 100 nm; that is reducing 1, 2, or 3 dimension (D) of a bulk material to the

nanoscale produces 2D films, 1D nanowires, or 0D nanoclusters, respectively. It well known the dimension of materials continuously shrinks down to nanometer or even smaller scale, some physical properties undergo changes known as the “quantum size effects”<sup>[1.85]</sup>. For example, the band gap of ZnO nanoparticles also demonstrates on size dependence. In the past few years, 1D nanostructures materials, such as nanowires, nanorods, nanotube, nanobelts, and nanotip have drawn much attention in basic scientific research and technology applications<sup>[1.86-1.90]</sup>. In general, the nanorods and nanowires have diameter of 1-200 nm, length of several micrometers with high aspect ratio (length/diameter). Many singular characteristics have been reported including fundamentals of mesoscopic phenomenon and the potential in the buildup of functional electronic<sup>[1.91]</sup>. In addition, the nanowires and nanorods can provide a material system to experimentally test fundamental quantum mechanical concepts. This section will focus on the physical properties of ZnO nanostructures, including field emission, sensing and resistive switching properties.



### ***1-4-1 Field emission properties***

In physics, the characteristic of field emission was first observed by Wood more than one hundred years ago<sup>[1.92]</sup> and theoretically explained by Fowler and Nordheim in 1928<sup>[1.93]</sup>. Generally, the phenomenon of taking electrons from the surface of materials and making them available as free electrons is called as electron emission. The electrons cannot normally escape from the surface of materials at room temperature. The electron field emission depends on a very high electric field at the emission surface. As the electric field at the surface is increased, the potential barrier and the width are reduced. The decrease in barrier width allows the electrons having energy less than electric field at vacuum level to tunnel through (as shown in Figure 1.8). They derived the current-voltage characteristic of field emission process, which

can be written as the follow:

$$J = \frac{e^3 E^2}{8\pi h \varphi} e^{-\frac{8\pi\sqrt{2m}\varphi^{\frac{3}{2}}}{3heE}} \quad (1-9)$$

where J is the current density (A/cm<sup>2</sup>),  $e$  is the electron charge, E is the electric field (V/cm),  $h$  is Plank's constant,  $m$  is the electron mass and  $\varphi$  is the work function (eV) of materials. After that, a modification of the Fowler-Nordheim law to take into account a sharpened emitter-tip shape has been suggested earlier as list in the follow [1.94-1.97].

$$J = \frac{A\beta^2 E^2}{\varphi} \exp\left(\frac{-B\varphi^{\frac{3}{2}}}{\beta E}\right) \quad (1-10)$$

$$\ln\left(\frac{J}{E^2}\right) = \ln\left(\frac{A\beta^2}{\varphi}\right) - \frac{B\varphi^{\frac{3}{2}}}{\beta E} \quad (1-11)$$

$$Slope = -\frac{B\varphi^{\frac{3}{2}}}{\beta} \quad (1-12)$$

$$Intercept = \ln\left(\frac{A\beta^2}{\varphi}\right) \quad (1-13)$$

where  $\beta$  is the field enhancement factor, A ( $1.56 \times 10^{-10} \text{ AV}^{-2} \cdot \text{eV}$ ) and B ( $6.83 \times 10^3 \text{ (eV)}^{-3/2} \text{ V} \cdot \mu\text{m}^{-1}$ ) are constants. In experiment,  $\beta$  could be determined from the slope in plots of  $\ln\left(\frac{J}{E^2}\right)$  vs.  $\frac{1}{E}$  when the work function ( $\varphi$ ) of material is known as shown in equation (1-12).

The tunneling approach to the electron field emission implies the knowledge of the potential energy barrier to the vacuum. This in turn is essentially determined by the strength of the electric field on the emission tip. For a single nanorod the problem can be modeled by a rounded conductive cylinder immersed in a uniform electric field, that is the single nanorod case:

$$E = \frac{V}{\alpha r_0} \quad (1-14)$$

where  $\alpha$  is conveniently chosen as coefficient. For the case of the nanotubes, the value  $\alpha=5$  is most usual. According the Filip model <sup>[1.97]</sup>, when many cylindrical emitters (cathode) are brought together, a neighborhood screening effect appears and the local field on every tip decreases sharply with decreasing distance between the nearest neighbors. In the extreme situation when many emitters (cathode) of equal length are brought into tight contact one actually gets a grounded flat surface facing an anode that is the plane condenser case:

$$E = \frac{V}{d} \quad (1-15)$$

where  $d$  is the cathode-anode gap,  $V$  is the cathode voltage. Clearly, the field on the emission sites of real emitters has to be a compromise between those limiting cases. Therefore, V. Filip et al. propose the following phenomenological formula for the strength of the electric field on the cap of a emitter of radius  $r_0$  belonging to a cathode film whose average gap to the anode is  $d$ :

$$E = s \frac{V}{r_0} + (1-s) \frac{V}{d} \quad (1-16)$$

The screening effect is entirely embedded in the parameter  $s$ ; whose range is between 0 (for very densely arranged uniformly oriented tubes) and 1 (for a single emitter). Obviously the most realistic values of  $s$  for emitters have to be found near 0 since the ratio  $d=r_0$  is usually of the order of 1000 and the equation can simply formation for the extraction field:

$$E = \beta \frac{V}{d} = \beta F_0 \quad (1-17)$$

where  $F_0$  is defined as the apparent field. Nevertheless it should be remembered that in practice the parameter  $\beta$  is not a characteristic of the emitters but of the entire setup, since it depends on the gap distance  $d$ : This fact can be seen from a direct

comparison between equation (1-16) and (1-17):

$$\beta = 1 + s\left(\frac{d}{r_0} - 1\right) \cong 1 + s\frac{d}{r_0} \quad (1-18)$$

From the viewpoint of applications, it should be noted that the major requirements for a good field emitter are low turn-on/threshold fields, high current density, high enhancement factor and good reliability. Therefore, in order to get good field emission properties, the emitters should possess a low work function, small dimension of emitter and uniform emitters distribution. In Chapter 2, the plasma etching methods are proposed to control the emitter tip angle to enhance the operating time of the ZnO nanorod emitters.

Generally, two main problems of reliability for the field emission devices are observed, an abrupt variation of turn-on field and a gradual degradation of emission current for a long operating time. These two phenomena might result from different destruction induced from applied electric field or the field emission current. As a speculation, the electrostatic force and the Joule heat generated by high current might be the major factors that degrade the reliability of the field emission properties.

#### ***1-4-2 Gas sensor and ultraviolet photodetectors***

Oxygen vacancies on metal-oxide surfaces are electrically and chemically active. It is well known that oxygen molecules in an air environment are adsorbed onto the surface of the metal-oxide nanowires to be ionized to  $O_2^-$ ,  $O^-$  and  $O^{2-}$  ions by extracting electron from the conduction band of the oxides<sup>[1.98-1.100]</sup>. The degree of ionization depends on the temperature.  $O_2^-$  is chemisorbed at low temperature (commonly below 100°C) while  $O^-$  and  $O^{2-}$  are chemisorbed at high temperature (commonly above 100°C). These vacancies function as n-type donors and significantly increase the conductivity of oxide. When the adsorption of charge

accepting molecules at the vacancy sites, such as NO<sub>2</sub> and O<sub>2</sub> (oxidation gas), electrons are effectively depleted from the conduction band, leading to a reduced conductivity of the n-type oxide. On the other hand, molecules, such as H<sub>2</sub> (reduction gas), would react with surface adsorbed oxygen and consequently remove it, leading to an increase of conductivity, as shown in Figure 1.9<sup>[1.101]</sup>.

Most metal-oxide gas sensors operate based on this principle. As one of the major materials for solid state gas sensor, bulk and thin films of ZnO have been proposed for NH<sub>3</sub>, alcohol and H<sub>2</sub> sensing under elevated temperature (~400 °C)<sup>[1.102-1.105]</sup>. From the aspect of sensing performance, 1D ZnO nanostructure, such as nanowires and nanorods, is expected to be superior to its thin film counterpart. Since their diameter is small and comparable to the Debye length, chemisorption induced surface states effectively affect the electronic structure of the entire channel, thus confer 1D ZnO nanorods and nanowires have higher sensitivity than thin film.

Ultraviolet (UV) light irradiation of the nanoparticles device of ZnO in air observed to result in a significant increase of the conductivity, as shown in Figure 1.10<sup>[1.106]</sup>. These processes could be observed by introducing ON/OFF switch between light source and the ZnO nanostructure as list in the follow:

Initial state



Switch ON



Switch OFF



Upon illumination, photogenerated holes discharge surface chemisorbed  $O_2^-$  through surface electron-hole recombination, while the photogenerated electrons significantly increase the conductivity. When illumination is switched off,  $O_2^-$  molecules re-adsorb onto nanostructure surface and reduce the conductivity. In general, the properties of the photodetector were demonstrated to be improved through nanostructure. Some critical performance parameters of the photodetector are include responsively, photocurrent, recovery time and reliably.

### ***1-4-3 Resistive random access memory (RRAM)***

Semiconductor memory has played an important role in the modern electronic devices. It is always a major driver for the development of semiconductor industry during the last few decades. According to the storage property, the modern memory devices are mainly classified into two groups. The first group is the volatile memory (VM), which can hold the stored data only when the system power is supplied. The widely-used VM devices are dynamic access memory (DRAM) and static random access memory (SRAM). The other group is nonvolatile memory (NVM), whose the stored data can be held for a long time without any power supply. For ideal NVM devices, it is expected to possess the properties of low operation voltage, low power consumption, high operation speed, high endurance, long retention time, nondestructive readout, simple structure, small size, and low cost <sup>[1,107]</sup>. However, there is no NVM device completely including the above properties up to now. Flash memory has been the mainstream of NVM devices nowadays, and it can be divided into the NOR flash and NAND flash. The NOR flash has high operation speed, which is suitable for the computer coding and mobile phone applications. On the other hand, the NAND flash possesses higher density property and is extensively used for the application of the large data storage.

However, the flash memory suffers some severe issues including high operation voltage, high power consumption, and low operation speed. In addition, as the continuous device scaling down, it will meet the physical scaling limitation in the near future, further leading to poor retention time and coupling interference effect <sup>[1.108]</sup>. Therefore, some modified flash memories, such as charge-trapping (SONOS) flash and band-engineered SONOS flash are proposed to replace the traditional flash memory. Moreover, many researchers are aggressively making their efforts to find the emerging NVM devices with the advantages of DRAM, SRAM, and flash memory. Several high-potential candidates for the next-generation NVM application, including ferroelectric random access memory (FeRAM) <sup>[1.109]</sup>, magnetoresistive random access memory (MRAM) <sup>[1.110]</sup>, phase change random access memory (PCRAM) <sup>[1.111]</sup>, and resistive random access memory (RRAM) have been extensively investigated, respectively. Compared with other NVM, RRAM is based on a large change in electrical resistance between low resistance state (LRS) and high resistance state (HRS) when it is exposed to voltage or current pulses. Both LRS and HRS memory states can be hold for a long time without any power supply and utilized to storage digital data. Table 1.3 illustrates the comparison between DRAM, SRAM, Flash, and the other next-generation NVM candidates <sup>[1.107]</sup>. As can be seen, RRAM possesses the better advantages, including low operation voltage, low operation power, high operation speed, high scalability, good endurance, and small size, than the other memory devices. As a result, it has been aggressively investigated to replace the present flash memory and extensively considered as the most potential candidate for the next-generation NVM application.

An RRAM device consists of one resistor and one corresponding transistor or diode. The resistor, fabricated in the back-end process, is in the structure of metal/insulator/metal (MIM) with the property of resistance changes for data storage.



During the RRAM operation, applying voltage bias on a thin insulator film (100 nm) sandwiched between two metal electrodes, the electrical characteristics of the MIM device are permanently changed. The device is then said to be formed or electroformed, which is called forming process. Before the resistive switching behavior is observed, forming process, similar to soft dielectric breakdown, is needed to active pristine RRAM devices<sup>[1.112-1.113]</sup>. This was reported to generate a critical number of point defects, such as oxygen vacancies and metallic defects, in the thin insulator film by applying external electrical signal. These defects will be align to form high leaky paths (conducting filaments) connecting top electrode and bottom electrode<sup>[1.114]</sup>, leading to the reproducible and repeatable resistive switching phenomenon. Therefore, the forming voltage is not only dependent on the thickness of the resistive thin film but also associated its film quality (i.e., defect concentration).

The basic RRAM operational principles, we need to distinguish the relation between the electrical polarity and the resistive switching phenomenon. The switching operation is called unipolar when the switching procedure is dependent on the amplitude of the applied voltage but independent of the voltage polarity. As shown in Figure 1.11, the unipolar switching is switched from HRS to LRS by sweeping voltage bias to the turn-on voltage (i.e., turn-on process), and the current is limited by the current compliance. The resistive switching back to LRS (i.e., turn-off process) takes place at a current higher than current compliance and the amplitude of turn-off voltage is smaller than that of the turn-on voltage. In contrast, the characteristic is called bipolar when the turn-on process occurs at one voltage polarity and the turn-off process at the reversed voltage polarity (Figure 1.12). As shown in Figure 1.13<sup>[1.115]</sup>, in combination with the unipolar and bipolar switching, the nonpolar switching operation is independent of the polarity of the applied voltage and current biases, which both positive and negative voltages can switch its memory state from LRS to

HRS, and vice versa.

## **1-5. Optical properties of zinc oxide**

ZnO generally reveals n-type conduction with a typical carrier concentration of  $10^{17} \text{ cm}^{-3}$ , which is smaller than the carrier concentration of  $10^{18}$  to  $10^{20} \text{ cm}^{-3}$  in ultraviolet light-emitting and laser diode applications. Compared with other direct wide band gap materials, ZnO exhibits a larger exciton binding energy ( $\sim 60 \text{ meV}$ ) which assures more efficient exciton emission <sup>[1.8]</sup>. In addition, the binding energy of ZnO is larger than its thermal energy ( $\sim 26 \text{ meV}$ ). For these reasons, ZnO has attracted considerable attention for optical applications such as ultraviolet light-emitting devices and optoelectronic devices. The optical spectrum is shown in Figure 1.14 <sup>[1.116]</sup>.

In ZnO, it is noted that the identities of the recombination centers and mechanisms for the luminescence properties are still a matter of controversy. There are two general kinds of emission manners in ZnO. One is the ultraviolet emission (UV emission), and the other is the visible emission. The UV emission is related to the conduction band and valence band of zinc oxide and the visible emission is related to the electron transition from the energy band of impurities and defects (oxygen vacancies) to the valence band. The optical properties of ZnO would be changed by dopant, structure, and annealing <sup>[1.117-1.118]</sup>. The mechanism of the ultraviolet and visible emission is shown in Figure 1.15.

## **1-6. Outline of dissertation**

In the first chapter, the relative backgrounds of this dissertation are introduced briefly including the field emission theory, the sensor theory, and the RRAM devices. Here the motivation and main ideas for the design of our experiment are also described simply.

In the chapter 2-4, the novel methods (plasma etching, chemical etching and two-step aqueous solution growth) are proposed to decrease amount of the oxygen vacancy to enhance the operating time of the ZnO nanotip emitters. The ZnO nanotip emitters have high potential for applications in electron field emission and light emitting devices in the future.

In the chapter 5, the novel spin-coating methods are proposed to prepare SnO<sub>2</sub>-ZnO core-shell nanostructure to enhance the sensitivity of hydrogen. The electrical properties of the core-shell nanowires in 0-200 ppm of hydrogen (H<sub>2</sub>) were measured at temperature of 250 °C. The ZnO-SnO<sub>2</sub> core-shell nanostructures made by two-step chemical growth have high potential for gas sensor application.

In chapter 6, the ultra-fast growth method is proposed to prepare short length and uniform ZnO nanorod array on flexible substrate to use in UV photodetector application. Owing to the good performance including mechanical flexibility, nondestructive properties, high reliability and multilevel photoresponse, the well-aligned ZnO nanorods grown on transparent and flexible PET polymer substrates have high potential for UV photodetector applications.

In chapter 7, the ultra-fast growth method is proposed to prepare dense and uniform Ga-ZnO nanorod array on Au/Ti/SiO<sub>2</sub>/Si substrate to use in RRAM application. This study also investigates the resistive switching behavior and conduction mechanisms of nanorod thin films without any embedding. Results demonstrate that the films exhibit excellent bipolar resistive switching behavior, including low operation voltage and good endurance property.

Finally, all experimental results in the previous chapters and all the suggested works for further researches are summarized in chapter 8 and chapter 9, respectively.

**Table 1.1** Properties of zinc oxide (ZnO) material <sup>[1.18]</sup>.

<b>Property</b>	<b>Value</b>
Lattice parameter $a_0$ (300K)	0.32495 nm
Lattice parameter $c_0$ (300K)	0.52069 nm
Ratio $c_0/a_0$	1.633
Density	5.606 g/cm <sup>3</sup>
Stable phase at 300K	Wurtzite (Hexagonal)
Melting point	1975 °C
Static dielectric constant	8.656
Refractive index	2.008
Energy gap	3.4 eV
Exciton binding energy	60 meV
Electron effective mass	0.24
Electron Hall mobility at 300 K for low n-type conductivity	200 cm <sup>2</sup> /V · s
Hole effective mass	0.59
Hole Hall mobility at 300 K for low p-type conductivity	5-50 cm <sup>2</sup> /V · s

**Table 1.2** Summary of different methods for aqueous solution growth <sup>[1.72-1.75]</sup>

<b>Growth solution</b>	<b>Resulting morphology</b>	<b>Focus of investigation</b>
Zinc nitrate + HMT	Nanorods Nanotubes	Influence of substrate and seed layer.
Zinc nitrate or zinc acetate + HMT	Highly aligned nanorods	Influence of substrate and seed layer.
Zinc nitrate + thiourea + ammonium chloride + ammonia	Nanowires Tower-like nanowires Flower-like nanowires Tube-like nanowires	Influence of growth temperature, reactants and growth time.
Zinc acetate + Sodium hydroxide + Citric acid	Disk-like nanorods Flower-like nanorods Nanorods	Influence of reactants and pH value of growth solution.

**Table 1.3** The comparison with the Flash memory and next-generation NVM candidates <sup>[1,107]</sup>.

Function	DRAM	SRAM	Flash	OUM	MRAM	RRAM
Non-volatility	No	No	Yes	Yes	Yes	Yes
Program power	Low	Low	High	Low	High	Low
Program voltage	Low	Low	High		Medium	Low
Read dynamic margin	100-200 mV	100-200 mV	Delta Current	10-100X	20-40 %	10-1000X
Write-Erase time	50ns-50ns	8ns-8ns	1 $\mu$ s-1-100 ms	12ns-50ns	30ns-30ns	10ns-30ns
Read time	50ns	8ns	50ns	20ns	30ns	20ns
Program power	Medium	High	High	Low	Medium	Low
Multi-bit storage	No	No	Yes	Yes	No	Yes
Scalability limits	Capacitor	6T	T-Ox/HV	Litho	Current	Litho
Endurance	$\infty$	$\infty$	$10^{12}$	$>10^{12}$	$?10^{15}$	$?10^{15}$
Cell size (F <sup>2</sup> )	6-12	50-80	7-11	5-8	?	4

# The Scale of Things-Nanometers

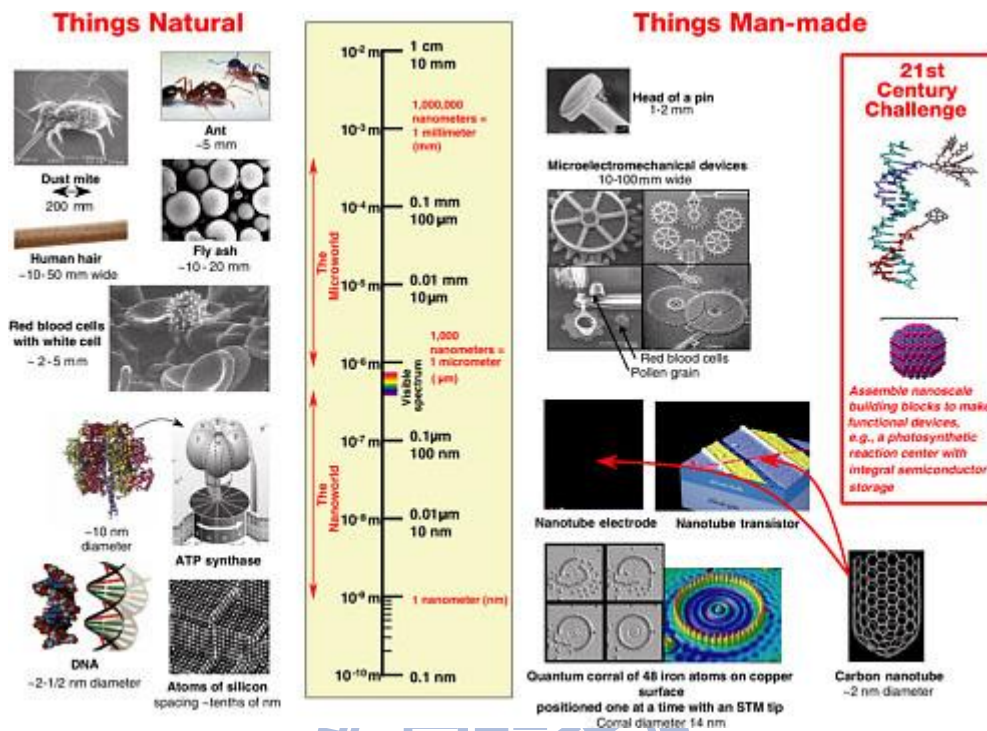


Figure 1.1 The scale of nanoscale [1-1].

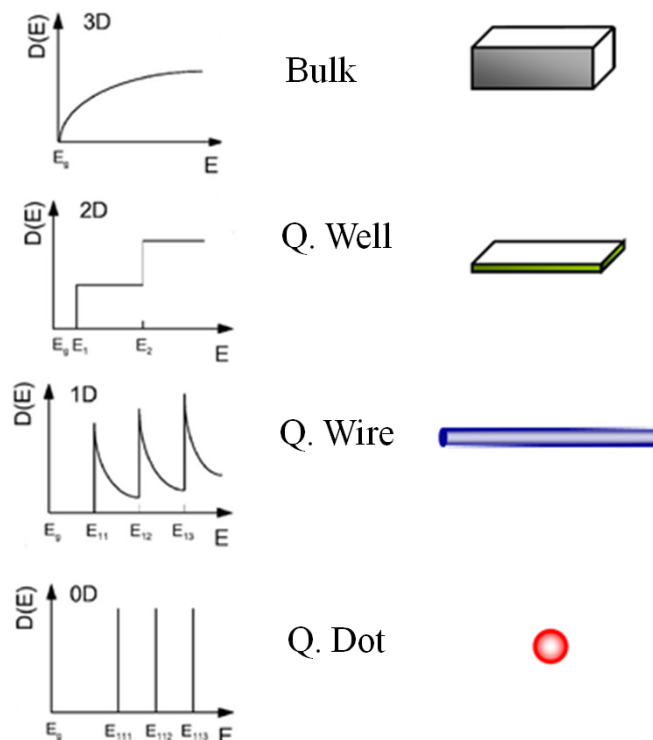
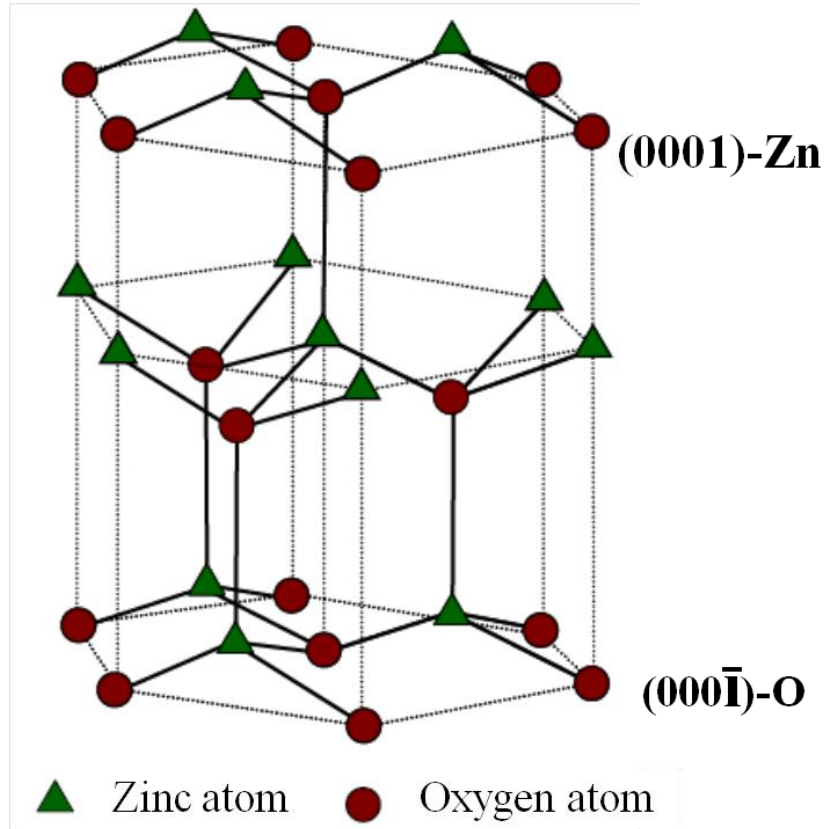
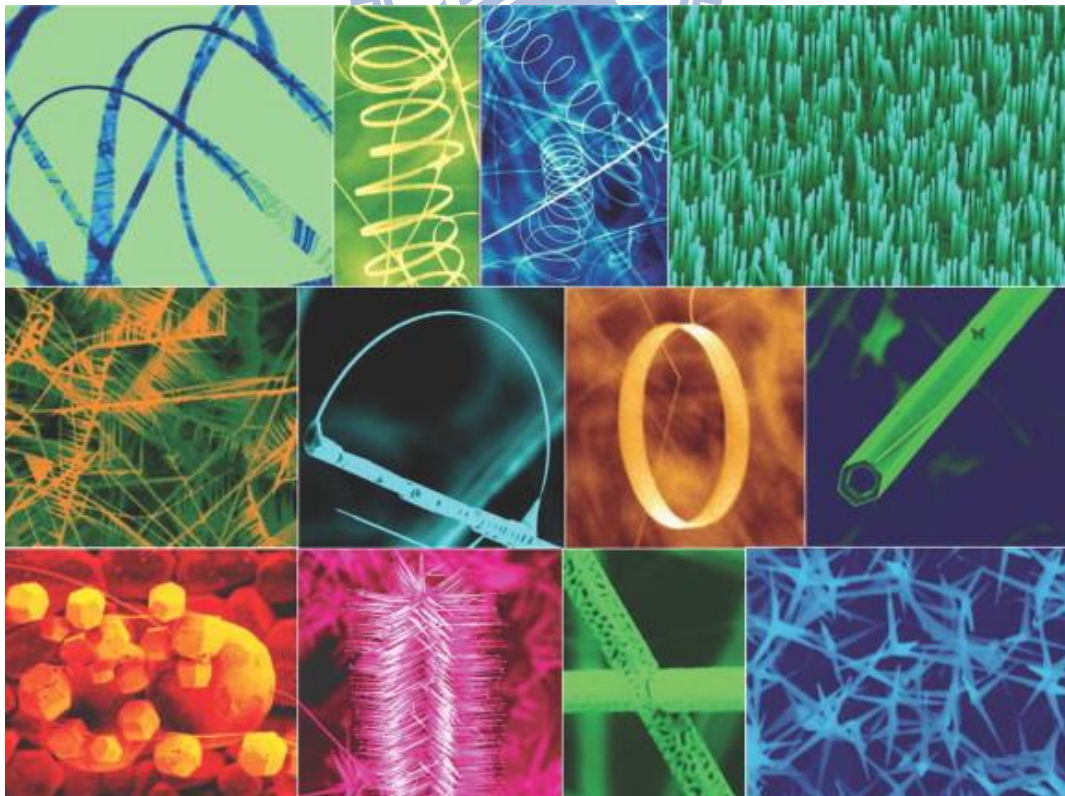


Figure 1.2 The dimensionality of confinement and its effects on the density of states [1.2].





**Figure 1.3** The wurtzite structure model of ZnO.



**Figure 1.4** SEM images of various ZnO nanostructures <sup>[1.42]</sup>.

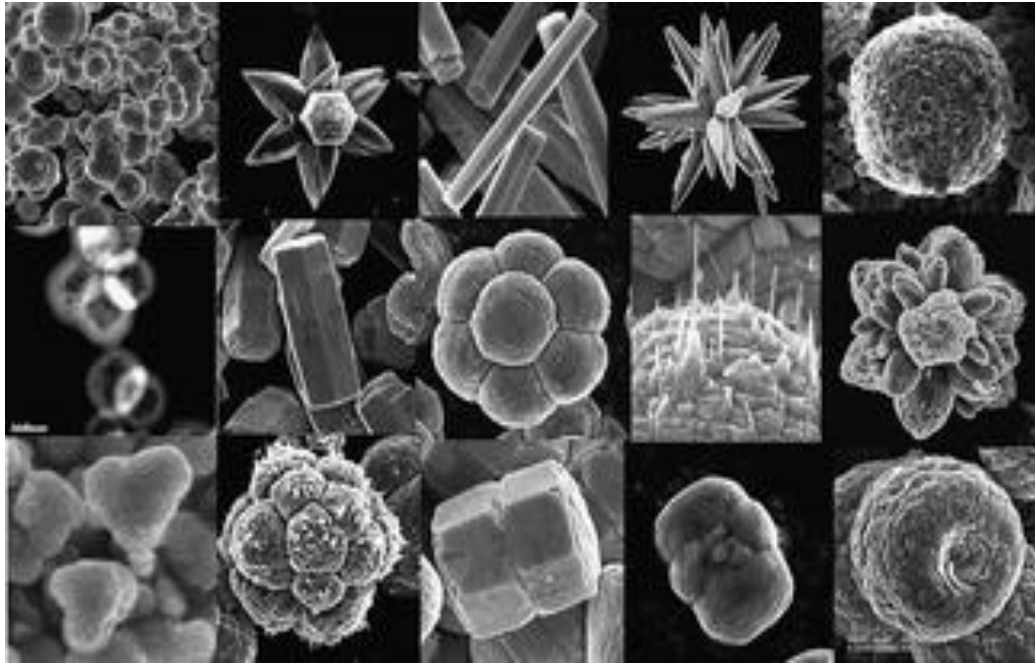


**Figure 1.5** SEM images of various ZnO nanostructures <sup>[1.43]</sup>.

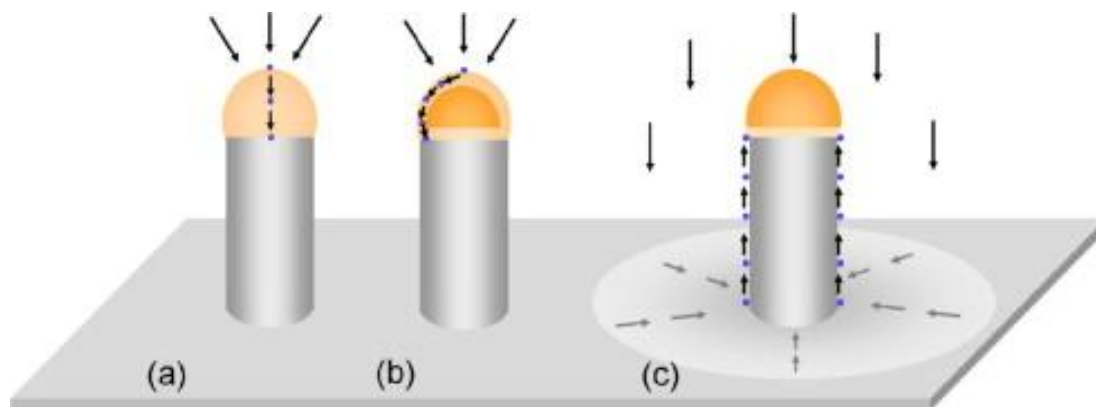


**Figure 1.6** Diffusion models for the source atoms to the growth front of the nanowires: (a) classical VLS with diffusion through a liquid seed, (b) a partially molten particle with liquid surface and interface and solid core and (c) a solid growth seed with a liquid particle wire interface and additional surface diffusion area <sup>[1.55]</sup>.



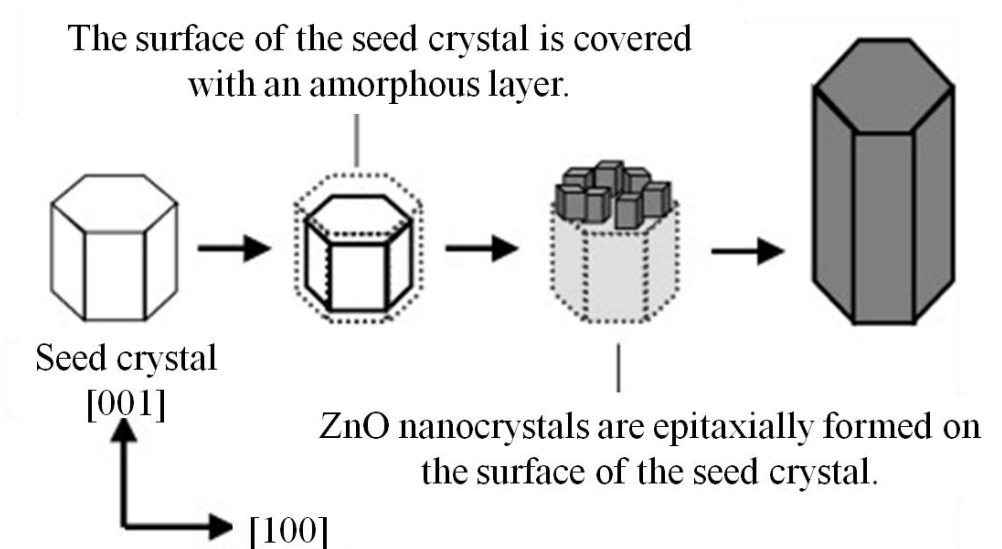


**Figure 1.7** Aqueous solution growth mechanisms of ZnO nanorods <sup>[1.78]</sup>.

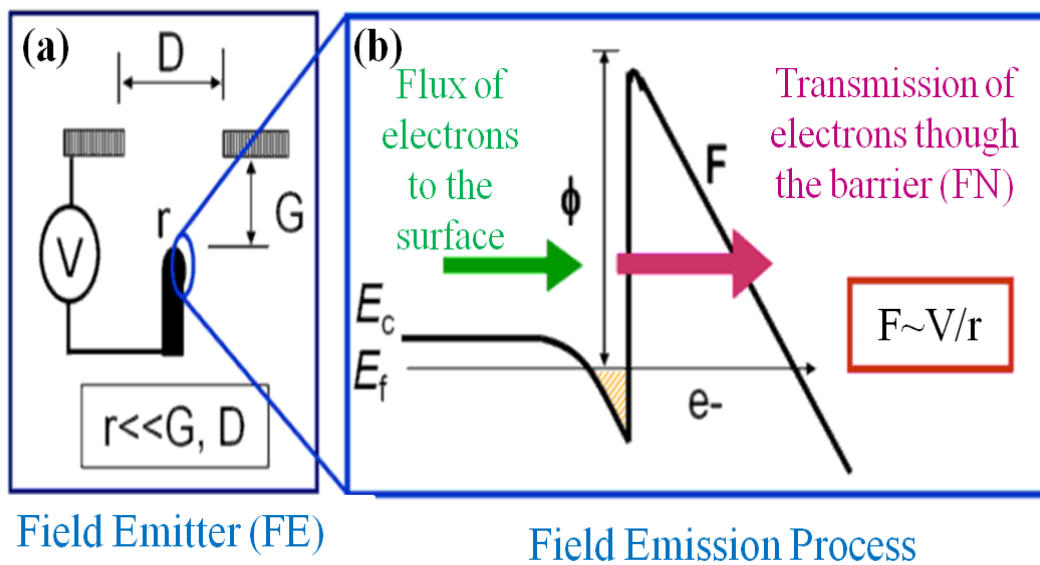


**Figure 1.8** (a) Field emission of electrons from metal or semiconductor surfaces. (b) Band diagram of a semiconductor field-emitter under biasing.

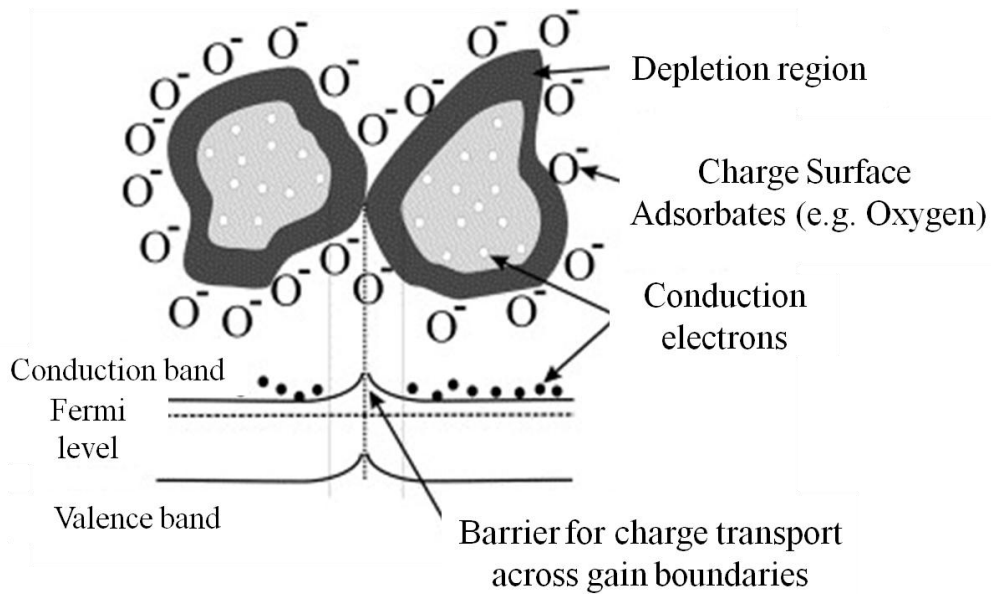


**Figure 1.9** Schematic diagram of charge carrier concentration in gas sensor [1.101].

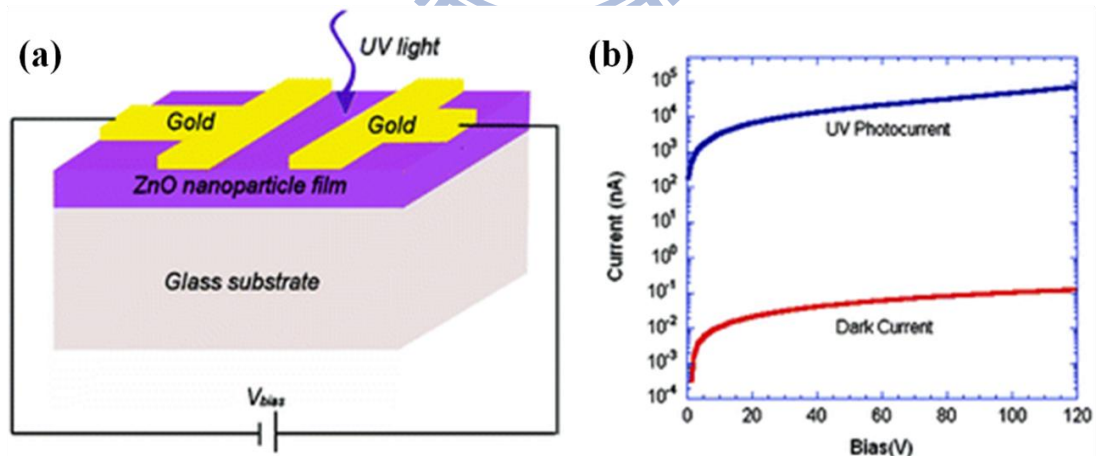
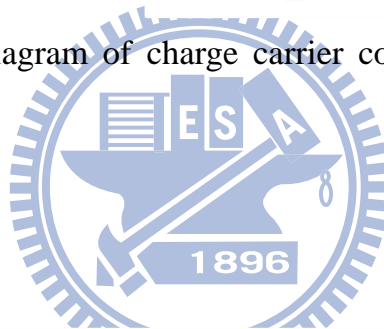


**Figure 1.10** (a) Schematic of a ZnO nanoparticle film device structure. (b) Current versus voltage for a ZnO nanoparticle film device in the dark and under  $0.83 \text{ mW/cm}^2$  illumination at  $370 \text{ nm}$  [1.106].

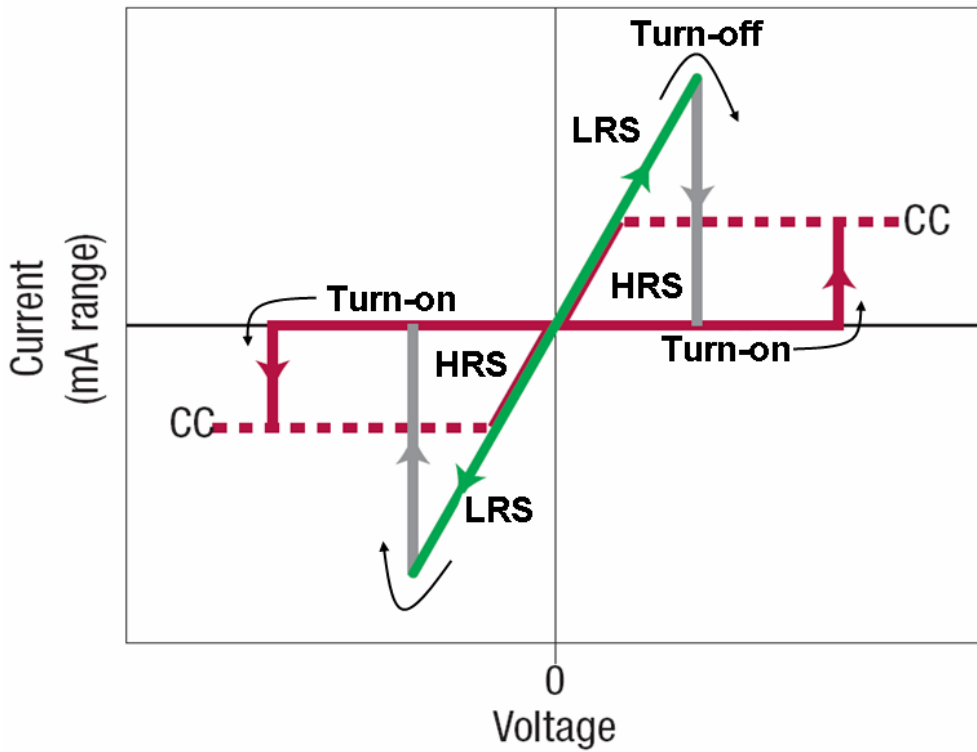


**Figure 1.11** The typical  $I$ - $V$  curve of unipolar resistive switching. LRS and HRS are switched by applying the same voltage polarity but the amplitude of the turn-off voltage is always smaller than that of the turn-on voltage.

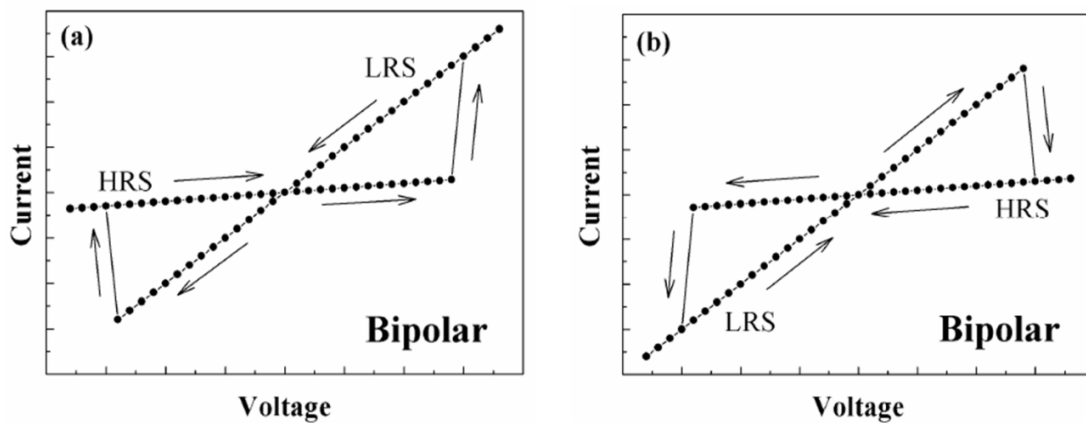


**Figure 1.12** The typical  $I$ - $V$  curves of bipolar resistive switching. The turn-on process occurs on one voltage polarity while the turn-off process is triggered by the opposite voltage polarity.

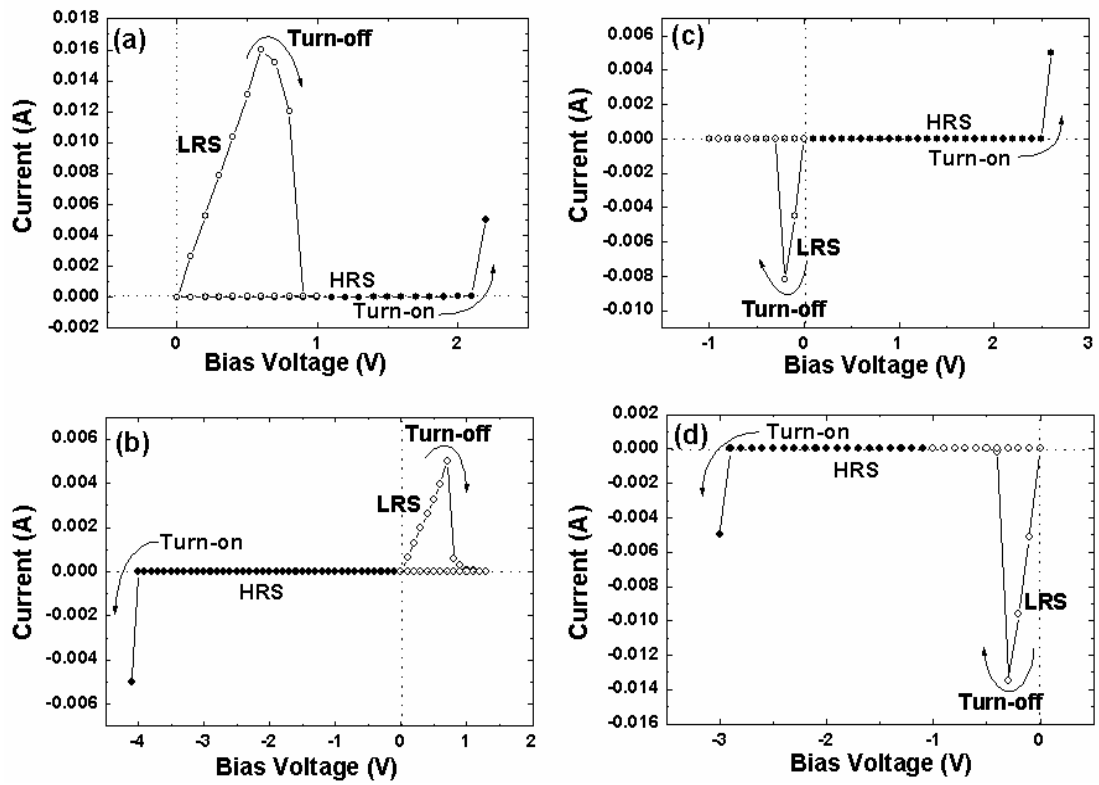


**Figure 1.13** The typical  $I$ - $V$  curve of nonpolar resistive switching. The amplitude of the turn-on voltage is always higher than the voltage at which the turn-off process occurs <sup>[1.115]</sup>.

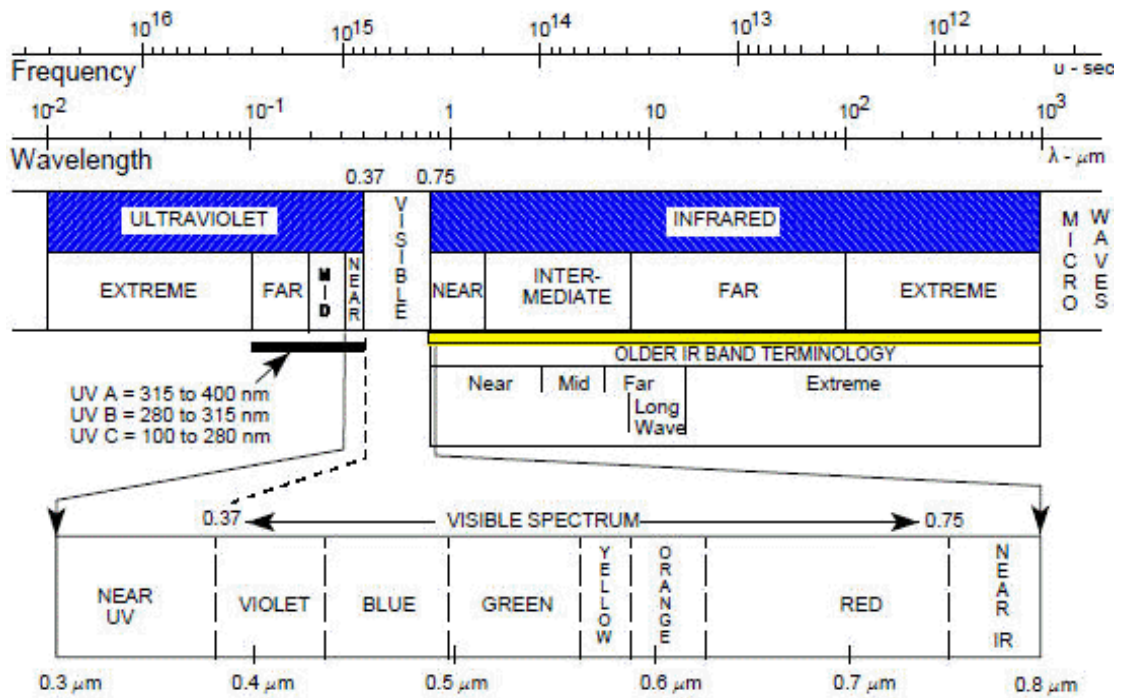


Figure 1.14 Optical spectra [1.116].

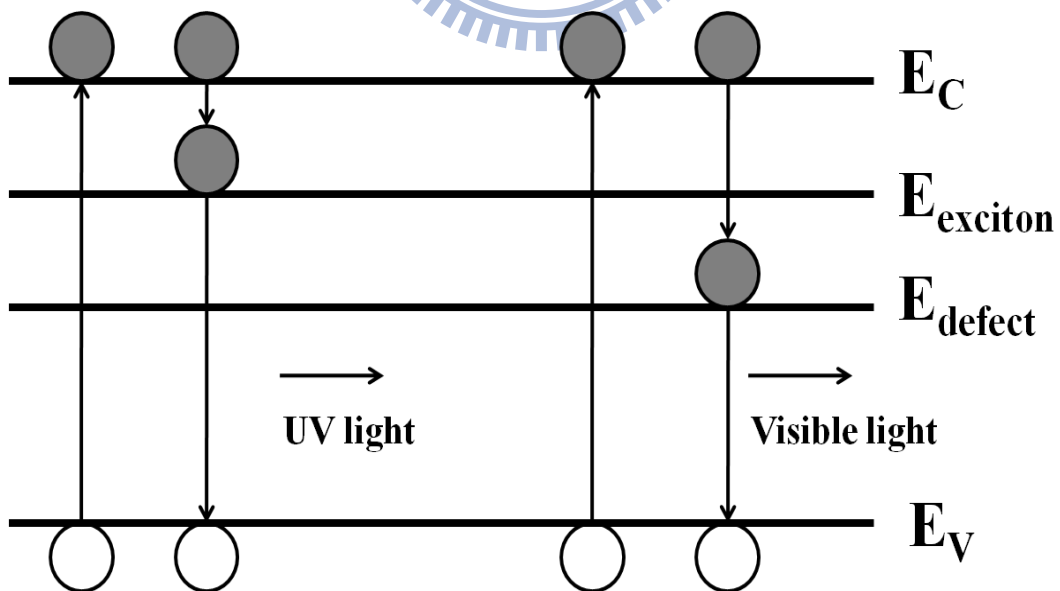


Figure 1.15 Mechanism of ultraviolet and visible emission.

## Chapter 2

### Nano Tip Fabrication of Zinc Oxide Nanorods and their Enhanced Field Emission Properties

#### 2-1. Introduction

One dimensional (1D) ZnO nanomaterials have recently received much attention for their potential applications in field emission displays, solar cells and other nanodevices<sup>[2.1-2.3]</sup>. So far, among several kinds of fabrication techniques including thermal evaporation, vapor-liquid-solid (VLS) growth<sup>[2.4]</sup>, metal-organic chemical vapor deposition (MOCVD)<sup>[2.5]</sup> and aqueous solution method<sup>[2.6]</sup> used for synthesizing 1D ZnO nanomaterials, aqueous solution synthesis has the advantages of low temperature, pressure, simple equipment and ambient being achievable for large area fabrication of different nanostructures. Efficient electron field emission is one of the unique properties of many low dimensional nanomaterials. Especially, ZnO nanorods have been investigated as electron field emitters due to their high temperature stability, large scale application, high aspect ratio and low working function<sup>[2.7-2.11]</sup>. The recent field emission analysis result of the 1D ZnO nanomaterials indicates that electrons are more easily emitted from the nanostructures with sharp tips than the nanostructures with a uniform diameter. Therefore, it is necessary to control the morphologies of the nanorods for improving their field emission properties. In this chapter, we fabricate ZnO nanorods by using aqueous solution method and develop a new technique to form ZnO nanotip structure from the as-grown ZnO nanorods by using the chemical etching and plasma etching combination process. Base on the two-step etching process, we could develop

adjustment of ZnO nanotip angle.

## 2-2. Experimental method

The p-type Si (100) substrate was cleaned by a standard RCA cleaning method and then rinsed in Hydrogen fluoride to remove native oxide from the surface of Si substrate. Subsequently, the epitaxial ZnO buffer layer was deposited by rf-sputtering and followed by in-situ annealing at 750°C for 30 min. After annealing, the thickness of the epitaxial ZnO buffer layer was about 100 nm, which had a highly preferred orientation along (002). Unless specified, the aqueous solution synthesis was carried out at 80°C in a sealed kettle placed in a quartz beaker. The pre-modified substrates were immersed in precursor solution for 2 h. The precursor solutions was prepared by mixing zinc nitrate hexahydrate ( $\text{Zn}(\text{NO}_3)_2 \cdot 6\text{H}_2\text{O}$ ) with methenamine ( $\text{C}_6\text{H}_{12}\text{N}_4$ ) while keeping their mole ratio at 1:1 (0.0375 M). After the aqueous solution synthesis, the nanorods were put in a sealed vessel with various volume ratios dilute acetic acid at 80°C for chemical etching process. The etching time was varied from 1 to 4 h to obtain the nanorods with various top morphologies, which were then bonded on a sputtering target by carbon tape and exposed to Ar plasma with a rf-power of 30 W under a pressure at  $5 \times 10^{-2}$  Torr for 30 sec for the plasma etching. The morphology, size distribution, and crystal structure of the ZnO nanorods with nanotips were characterized using X-ray diffractor (XRD, Bede D1), field-emission scanning electron microscope (FE-SEM, Hitachi S-4700I), transmission electron microscope (TEM, JEOL 2010). The chemical composition was estimated by a energy dispersive X-ray spectrometer (EDS, Oxford ISIS300). The field-emission current-voltage (I-V) curves of both as-grown ZnO nanorods and the nanorods with nanotips were measured at room temperature in the tubo pump vacuum chamber at a pressure of  $2 \times 10^{-6}$  Torr. We used micrometer to adjust the distance between a anode and tip of

ZnO nanorods was 250  $\mu\text{m}$ . The micrometer with the an accuracy of  $\pm 0.1 \mu\text{m}$ . The dependence of the field emission current on the anode-cathode voltage could be recorded automatically with Keithley 237 picoammeter measurement system. The lifetime test was also carried out for the nanorod emitters. The nanorods emitters could be subjected to the field emission test at least 1000 times under the sweeping electric field from 0.4 to 4.4V/ $\mu\text{m}$  without obvious changes in the results and the step time between first and second cycling is defined as 5s.

## **2-3. Results and discussion**

### ***2-3-1 Morphology and crystalline of ZnO seed layer***

Figure 2.1 shows the XRD patterns of seed layers which are annealed at different temperature under Ar/O<sub>2</sub> flow ratio of 3. It indicates that the (002) orientation of seed layer is improved by annealing. And the (002) peak increases with increase of annealing temperature. Figure 2.2 is the SEM images of annealed ZnO seed layer, (a) shows the top view and (b) is corresponding cross view. It can be found that there are many obvious grains in the seed layer. The thickness of seed layer is about 100nm. In order to grow nanorod array along C-axis, we choose to deposit seed layer under Ar/O<sub>2</sub> flow ratio of 3 and anneal it at 750°C in this thesis.

### ***2-3-2 Morphology and crystalline of ZnO nanorod structure***

The morphologies of as-grown ZnO nanorod were observed using FE-SEM and their typical SEM images are shown in Figure 2.3. The well aligned as-grown nanorods have perfect orientation perpendicular to the substrate and relatively high cover density (Figure 2.3 (a)). After chemical etching for 1h, only little area near the edge of the nanorods disappears. The etching direction occur from edge to center with



an increased etching time up to 2 h and its image is shown in Figure 2.3 (b). All these phenomena can be explained by isotropic etching. The six  $\{1\bar{1}00\}$  families of planes of the ZnO nanorods possess same surface energy, therefore, the six isotropic planes have the same etching rate during etching process. We can consequently control the top area of ZnO nanorods through using different solution conditions: e. g. etching time, solution concentration and etching temperature. The following plasma etching process is employed to form sharper ZnO nanotips with the different tip angles.

The SEM image of the as-grown ZnO nanorods after plasma etching treatment with a rf-power of 30 W under a pressure at  $5 \times 10^{-2}$  Torr for 30 sec is shown in Figure 2.4 (a), indicating that the ZnO acute nanotips are formed after such a plasma treatment and the tip angle is approximately  $110^\circ$  (inset in Figure. 2.4 (a)). For obtaining smaller tip angle, the combination of chemical and plasma etching process is employed. Figure 2.4 (b) shows the SEM image of the nanotips obtained by chemical etched for 2h and then plasma treatment with the same condition as the above-mentioned, indicating that the tip angle is approximately  $85^\circ$  can be obtained. (inset in Figure 2.4 (a)). Our experiment result depicts that such a two-step etching method, chemical etching for controlling the top area of as-grown ZnO nanorods and plasma etching for obtaining acute tips, we can easily fabricate the nanorods with various tip angles for field-emission application. The schematic description of the two-step etching process is shown in Figure 2.5.

The crystallinity and morphology of the as-grown and the ZnO nanorods after two step etching process are investigated by TEM equipped with selected area electron diffraction (SEAD). Figure 2.6 shows the TEM and EDS spectra of the as-grown ZnO nanorods, indicating that the ZnO seed layer and the as-grown ZnO nanorods are composed of only Zn and O. No evidence of other impurities is found

from the spectrum. With further quantitative analysis of EDS, it reveals that the atomic ratio of Zn/O is 57:43 and 51:49 of seed layer and nanorod, which is close to stoichiometric ratio. To investigate the crystal orientation relationship, the high resolution TEM and Fourier transform patterns (FET) were obtained as shown in Figure 2.7. The high resolution TEM (HRTEM) images show the seed layer and nanorod have lattice planes with interplaner spaces of 5.22 and 5.21 Å, respectively and at the interface reveals no significant defect. The Fourier transform patterns from the seed layer, interface, and nanorod reveal the same growth direction, indicating the orientation relationships between seed layer and nanorods are follows: seed layer [0001]||nanorod [0001]. Figure 2.8 shows the TEM and HRTEM images of the nanorods after above two-step etching process, indicating that the nanorods have a small tip angle of the 85°, which is consistent the result of SEM observation. It also shows that the preferred growth of the ZnO nanorods is in the [001] direction. The clear lattice fringes indicate that the interplanar spacing of the (002) c axis of ZnO is 5.2Å (inset in Figure. 4), which is consistent with that of the International center for Diffraction Data (ICDD-2000) database No.80-0075 of ZnO.

### ***2-3-3 Field emission properties***

The typical field emission properties of the nanorods after various etching treatments are shown in Figure 2.9. The emission current -voltage characteristics were analyzed by using the Fowler-Nordheim (F-N) equation or the field emission measurement<sup>[2.12-2.15]</sup>

$$J = A \left( \frac{\beta^2 E^2}{\phi} \right) \exp \left( - \frac{B \phi^{1.5}}{\beta E} \right) \quad (2-1)$$

$$\ln \left( \frac{J}{E^2} \right) = \ln \left( \frac{A \beta^2}{\phi} \right) - \frac{B \phi^{1.5}}{\beta E} \quad (2-2)$$

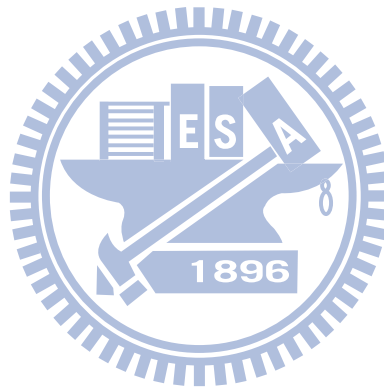
where J is the current density, E is the applied field,  $A=1.56 \times 10^{-10}$  (AeV/V<sup>2</sup>),

$B=6.83 \times 10^9$  (V/eV<sup>1.5</sup>m),  $\beta$  is a field enhancement factor and  $\psi$  is the work function of the emitter which is about 5.37 eV for ZnO. The  $\beta$  approximately equals  $s \times d/r$ , where  $s$  is dependent on screen effect,  $d$  is the distance from anode to cathode, and  $r$  is the radius of the emitter<sup>[2,12]</sup>. The log I-V plots for the nanorod field emitters are shown in the inset of Figure 2.9 (a), indicating that the turn on electric fields of the as-grown, plasma etching and two-step etching emitters are 6.01, 3.03 and 1.70 V/ $\mu$ m, respectively, at a current density of 1  $\mu$ A/cm<sup>2</sup>. When the work function of the nanorods is known, the field enhancement factor ( $\beta$ ) can be calculated from the slope of the F-N plot (inset in Figure 2.9 (a)). The  $\beta$  values are about 946, 1972 and 3513 for as-grown, plasma etching and two-step etching ZnO nanorod emitters, respectively. The average  $\beta$  of the ZnO nanorod emitters is related to the geometry, tip size and number density of the nanorods grown on substrate. The smaller tip angle of the nanorods after two-step etching process would lead to larger  $\beta$  value and lower turn-on field in comparison with that of the nanorods after only plasma etching, which is obviously confirmed by our experimental results shown above. Figure 2.9 (b) shows the stability of the turn-on field for as-grown, plasma etching and two-step etching nanorod emitters. It can be seen from the Figure 2.9 (b) that the turn-on fields of the nanorods after two-etching processes reach more stable values in comparison with the as-grown nanorods. From the as-grown nanorods, the variation of turn-on fields is more than 1 V/ $\mu$ m. We believe that the variation state of turn-on fields is due to the as-grown nanorods were destruction by electrons, which produce the many particles on the nanorods. In constant of two-step etching nanorod emitters, the variation of turn-on fields is less than 0.5 V/ $\mu$ m during 5000 sec. Based on lifetime measurement, we suggested that the plasma etching and two-step etching nanorod emitters were bombarded by high energy argon ions will reached to a stable state. Therefore, the turn-on fields of the nanorods after etching processes reach more stable

values in comparison with as-grown nanorods.

## 2-4. Conclusions

In summary, we successfully fabricated sharp tip structured ZnO nanorods by employing etching process. Through plasma etching, the  $110^\circ$  tip angle nanorods was obtained. We were able to easily control tip angle of the nanorods by using two-step etching process, a combination of chemical etching process and plasma etching process. After such plasma etching and two-step etching processes, the field emission properties of ZnO vertically aligned nanorod emitters were significantly enhanced and the stability of their turn-on fields was improved.



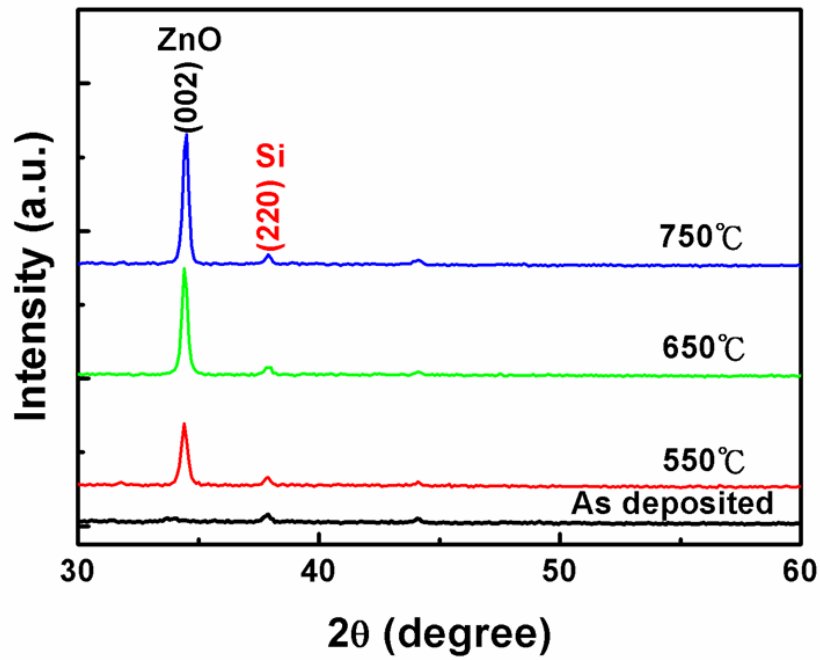


**Figure 2.1** The XRD patterns of ZnO seed layer which is annealed at different temperature.

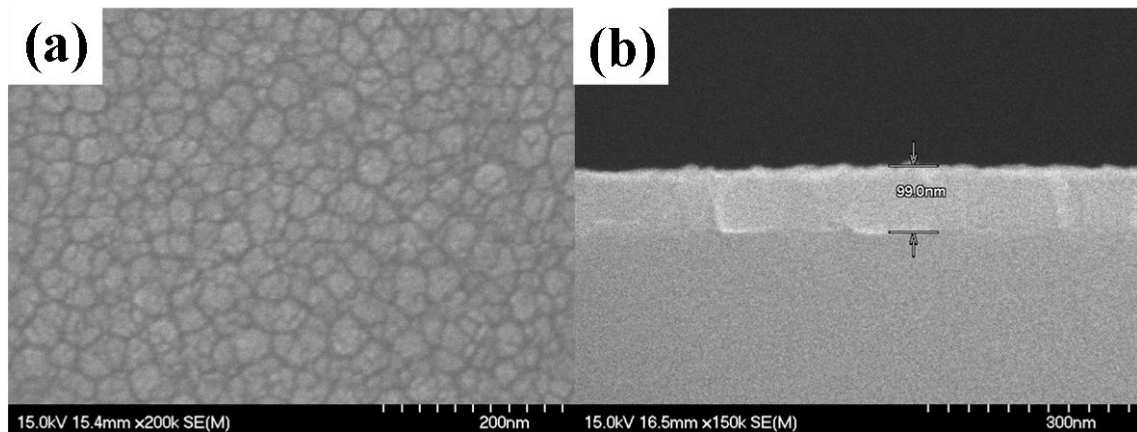


**Figure 2.2** The SEM images of annealed ZnO seed layer on Si substrate. (a) Top and (b) cross view.

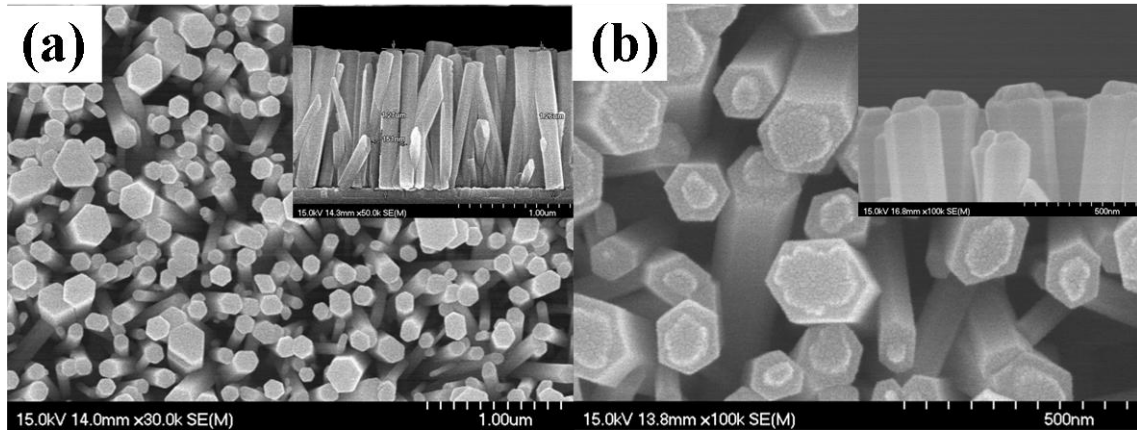


**Figure 2.3** Typical SEM images of (a) as-grown ZnO nanorods and (b) 2h chemical etching nanorods (inset: cross section images).

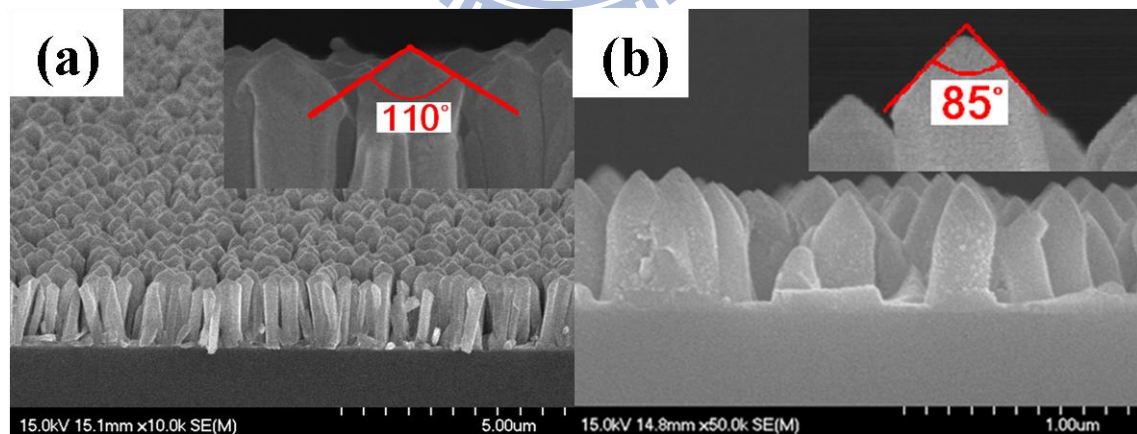


**Figure 2.4** Typical SEM images of (a) the ZnO nanorods after plasma etching and (b) the ZnO nanorods after two-step etching.

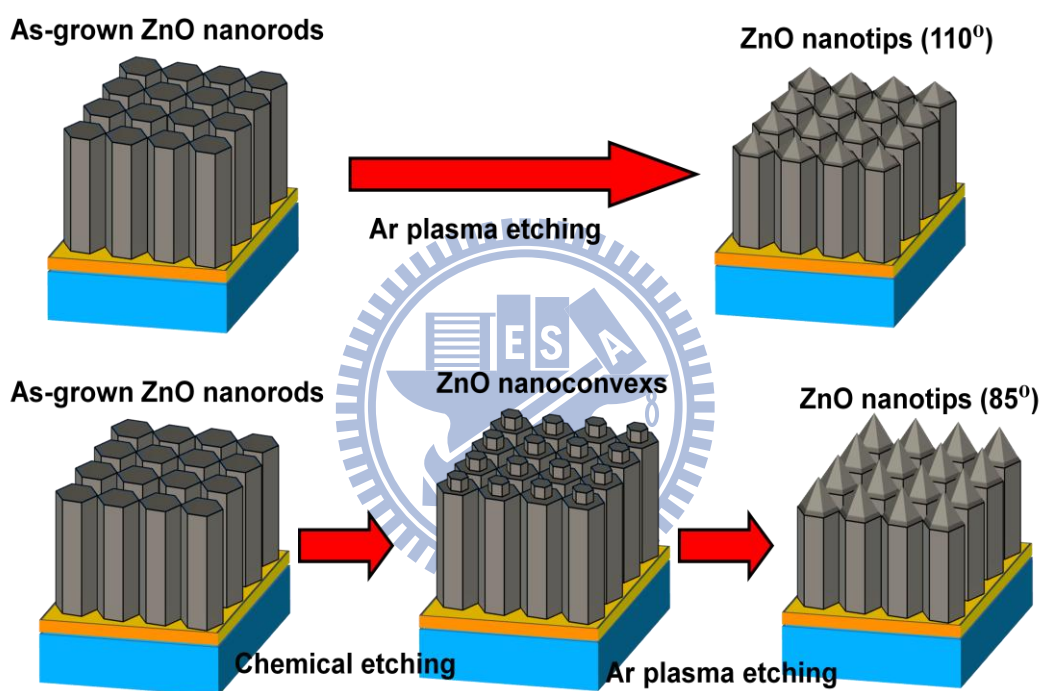


**Figure 2.5** Schematic illustration of the two-step etching process.



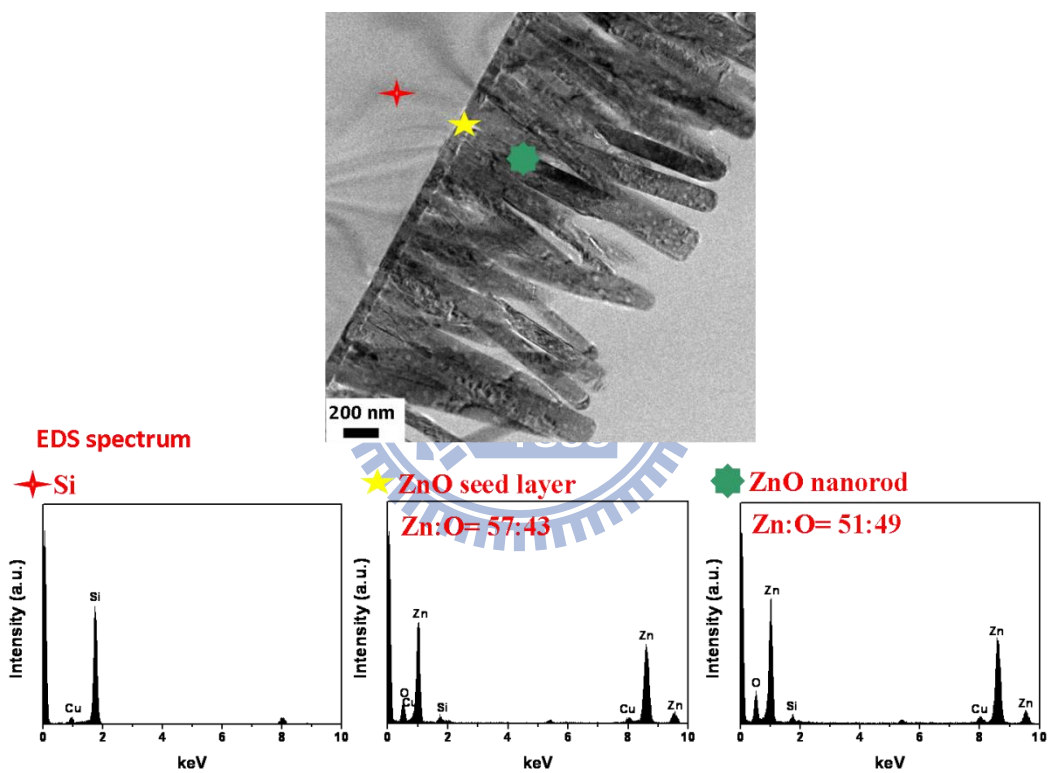


**Figure 2.6** Cross section TEM image and EDS spectrum of Si, ZnO seed layer, and as-grown ZnO nanorods.



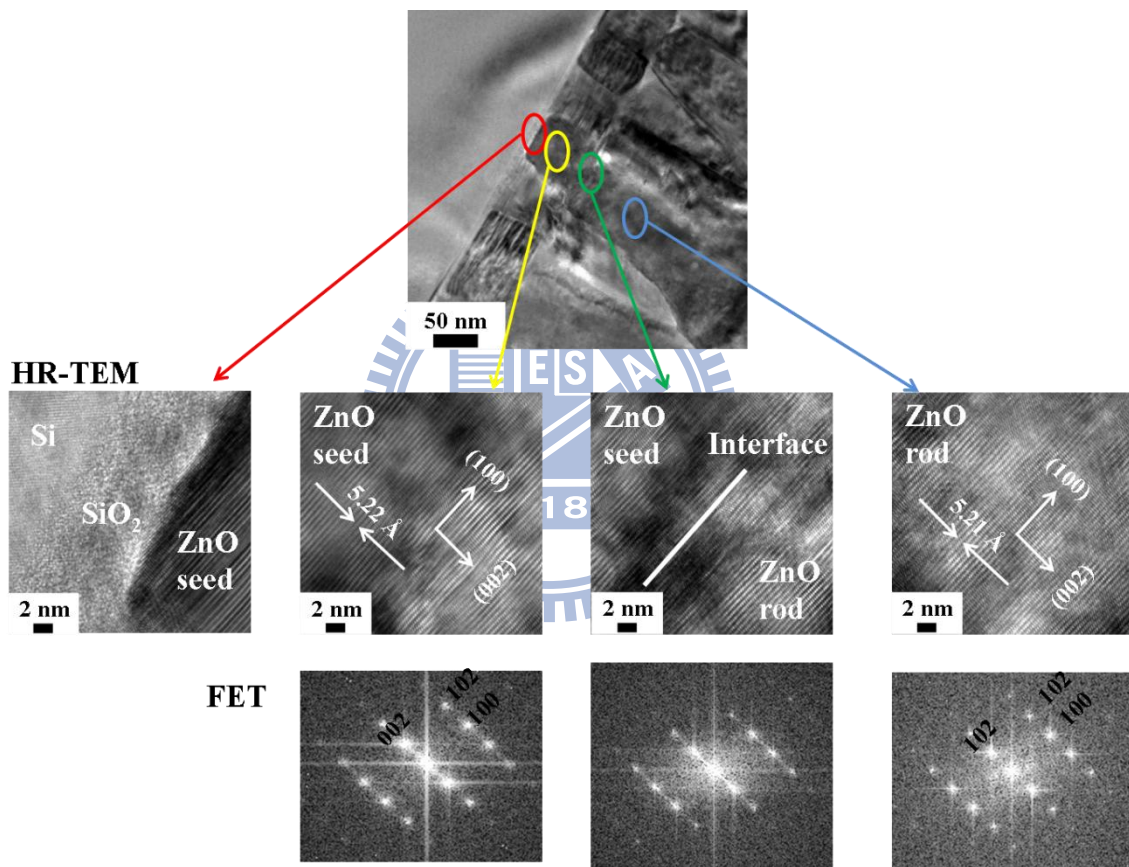


**Figure 2.7** HR-TEM images and FET patterns of Si, ZnO seed layer, and as-grown ZnO nanorods.

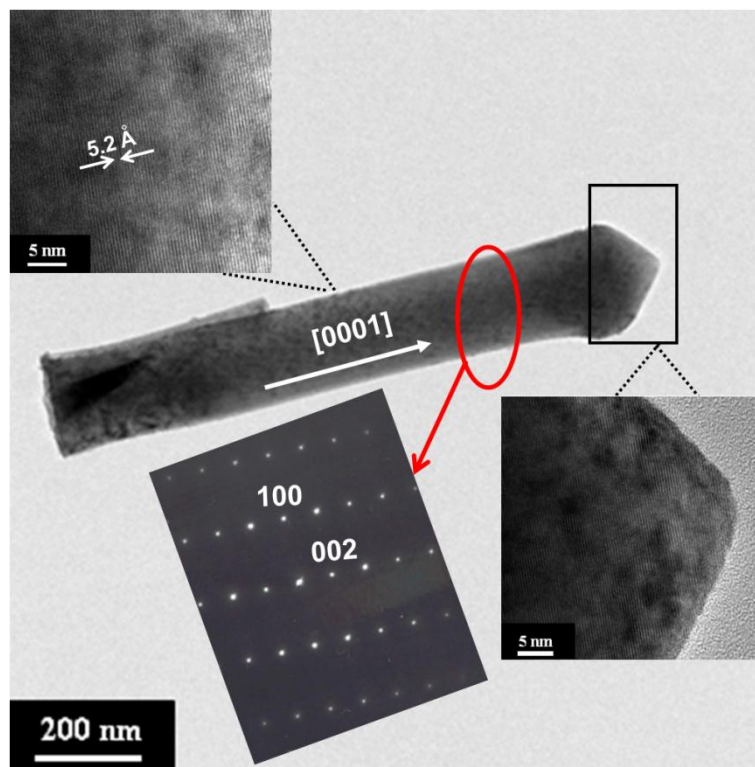


**Figure 2.8** TEM image of the single ZnO nanorod after plasma etching, the insets show the corresponding SAED pattern and high resolution TEM image.

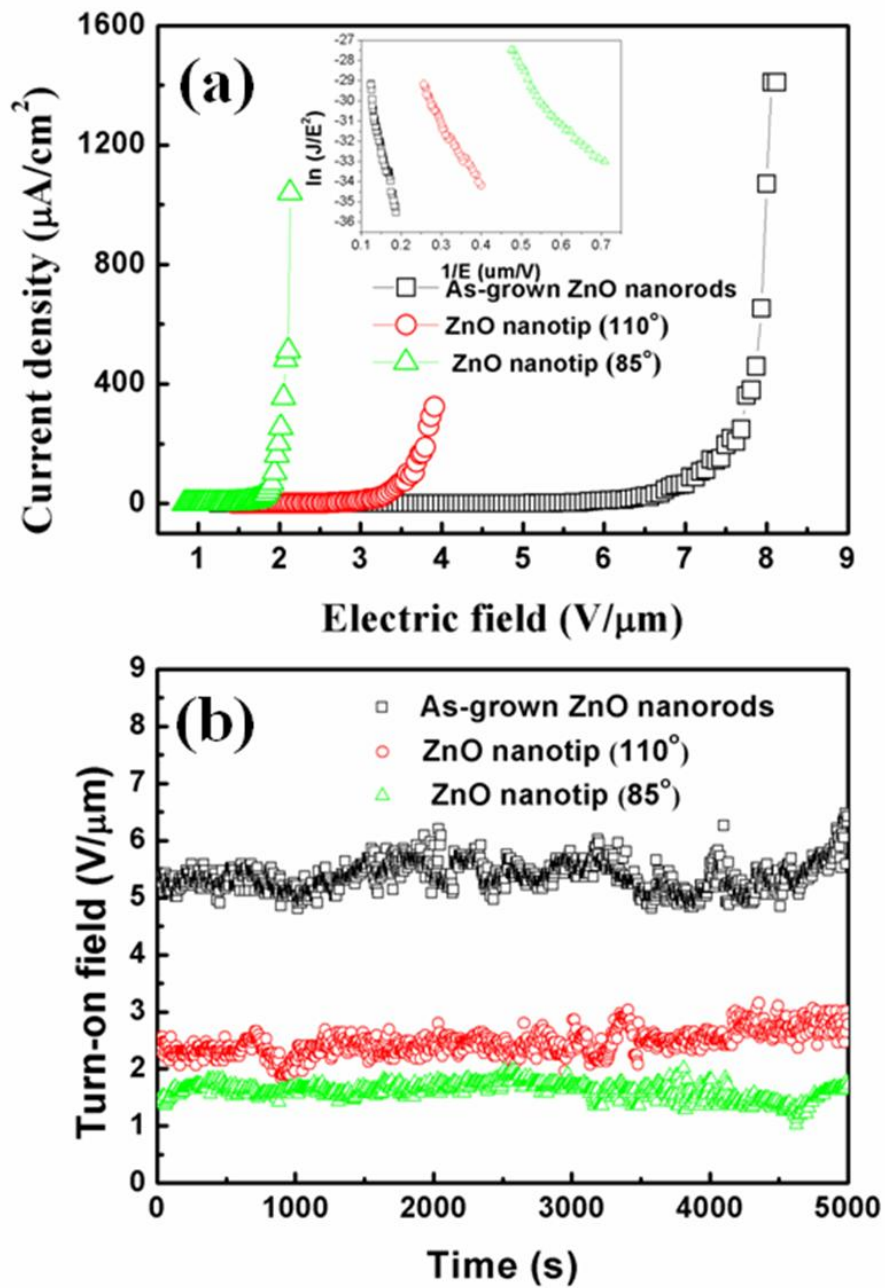


**Figure 2.9** (a) J-E curves (inset is F-N plots) and (b) Stability test of the nanorod emitters.

# Chapter 3

## Electrical Properties and Reliability of ZnO-based Nanorod Current Emitters

### 3-1. Introduction

One-dimensional (1D) semiconductor nanostructures attract renewed interest because of their excellent optoelectronic properties and promising applications<sup>[3.1-3.2]</sup>. Among the various applications, field emission displays had attracted a lot of interest for their high aspect ratio, proper number densities, and high emission stability<sup>[3.3]</sup>. Several groups have been reported on field emission from nanorods / nanowires such as carbon nanotubes (CNTs)<sup>[3.4]</sup>, diamond cones<sup>[3.5]</sup>, Ni<sub>31</sub>Si<sub>12</sub> nanowires<sup>[3.6]</sup> and ZnO nanorods<sup>[3.7-3.8]</sup> etc. Among 1D nanostructure, the ZnO nanorods are considered to be one of the most promising cold cathode materials due to their large exciton binding energy, strong radiation-oxidation resistance, and high thermal stability<sup>[3.9-3.10]</sup>. Generally, the field emission property depends on the material work function, tip morphology and number density of nanorod emitters. But, still it's a challenge to develop the nanorod emitters having good properties and high reliability. Therefore, improvement of the field emission performances is an important issue for their application in field emission displays.

It is well known that control the morphologies of the nanorods to improve their field emission properties because the vertically aligned ZnO nanorods have relatively large diameter and hexagonal structure at top end. Plasma treatment is an easy and fast process to control morphology of the nanorods. We recently reported the preparation of ZnO nanotip structures from the as-grown ZnO nanorods by using the

combination of chemical etching and Ar plasma treatment<sup>[3.11]</sup>. However, there is no literature that has ever been reported on the effect of oxygen plasma treatment on field emission properties of ZnO nanorods. In this chapter, we synthesized the ZnO nanorods by using solution method and employed oxygen plasma etching method to form nanotip on the as-grown nanorods. Effects of etching time on morphology of nanostructures, electrical and optical characteristics of ZnO nanorods are also investigated.

### 3-2. Experimental method

P-type Si (100) substrate was cleaned by a standard Radio Corporation of America (RCA) method. A thin film of zinc acetate was spin coated on the substrate for 10 times with a solution containing 5 mM zinc dehydrate ( $C_4H_6O_4Zn \cdot 2H_2O$ , 98 % purity) in ethanol. After deposition, the film was annealed at 350 °C for 30 min to produce ZnO buffer layer. Then, the aqueous solution synthesis of ZnO nanorod array was carried out at 90 °C in a sealed kettle placed in a quartz beaker. The ZnO coated substrates were immersed in a precursor solution for 3 hour. The solution containing of the 0.05 M zinc nitrate hexahydrate ( $Zn(NO_3)_2 \cdot 6H_2O$ , 99.9% purity) and the 0.05 M methenamine ( $C_6H_{12}N_4$ , 99.9% purity). After the reaction, the substrates were removed from the solution, rinsed with deionized water, and dried in the air. For making the nanorods with tip morphologies, nanorods were bound on a sputtering target by carbon tape and exposed to oxygen plasma for 0, 30, 60 and 120 s, respectively. For the plasma treatment, process pressure and rf-power were maintained at  $5 \times 10^{-2}$  Torr and 30 W, respectively.

The morphology, size distribution and crystal structure of all the nanorods were investigated by a field-emission scanning electron microscope (FE-SEM, Hitachi S-4700I), a transmission electron microscope (TEM, JEOL 2100F), and a X-ray

diffractor (XRD, Bede D1). The chemical composition was estimated by a energy dispersive X-ray spectrometer (EDS, Oxford ISIS300). The field-emission current-voltage (I-V) curves of all nanorod emitters were measured at a pressure of  $2 \times 10^{-6}$  Torr kept by a turbo molecular pump. A copper tip was employed to act as an anode with a tip area of  $7.09 \times 10^{-3} \text{ cm}^2$  and p-type Si covered with ZnO emitters as a cathode with an area of  $1 \text{ cm}^2$ . We used micrometer (accuracy of  $\pm 1 \text{ }\mu\text{m}$ ) to adjust the distance between a copper anode and nanorod emitters. The distances of the as-grown and other nanorod emitters with the anode are 100 and 150  $\mu\text{m}$ , respectively. The field emission properties are affected by the anode area and anode-cathode distance based on Filips model <sup>[3,19]</sup>. The turn-on and threshold fields are defined at current densities of  $1 \text{ }\mu\text{A}/\text{cm}^2$  and  $1 \text{ mA}/\text{cm}^2$ , respectively. The dependence of the field emission current on the anode-cathode voltage was recorded using programmable Keithley 237 picoammeter measurement system. The stability measurements were also carried out for the ZnO nanorod emitters at temperature of 25, 50 and 100  $^\circ\text{C}$ , respectively. The photoluminescence (PL) spectra were obtained using a He-Cd laser (325nm) as excitation source at room temperature.

### **3-3. Results and discussion**

#### ***3-3-1 Morphology, crystal structure, composition and optical properties of ZnO nanorod array***

Figures 3.1(a)-(d) show the FE-SEM morphologies of the as-grown and oxygen plasma treated (etching times of 30, 60 and 120 s, respectively) ZnO nanorod emitters. As show in Figure 3.1 (a), the as-grown ZnO nanorods arrays present typical hexagonal shape structure with an average diameter of 230 nm, an average length of 1.4  $\mu\text{m}$  and relatively high cover density. The morphology of ZnO nanorod emitters

reveals dramatic change due to the oxygen plasma treatment. While oxygen plasma treatment for 30 s, we find that the top of the nanorods becomes tower-shaped morphology. By increasing the treatment time to 60 s, the tip structure of the ZnO nanorod emitters is formed. The formation of acute nanotips morphology is due to the oxygen ion bombardment at the edge of the nanorods leading to isotropic etching<sup>[3.11]</sup>. Figure 3.1 (d) shows the morphology of the nanorods plasma treated for 120 s, indicating a destruction due to over etched and a decrease of aspect (c/a) ratio of the nanorods, which will degrade the performance of the emitters<sup>[3.12]</sup>.

Figure 3.2 (a) indicates that X-ray diffraction patterns of the as-grown and oxygen plasma etched ZnO nanorod array exhibit single phase with hexagonal wurtzite structure, (002) preferred orientation and the lattice constant of ZnO nanorods are  $a=b\sim 3.256 \text{ \AA}$ ,  $c\sim 5.204 \text{ \AA}$  (space group P63mc; JCPDS card NO. 36-1451). No characteristic diffraction peaks from impurities were detected. From Figure 3.2 (a), it shows that the intensity of the (002) diffraction peak increases with an increase of the oxygen plasma bombardment time up to 120 s. It indicates that the oxygen ions bombardment not only helps to form tip structure but also oxidizes the oxygen vacancies at the ZnO nanorods. The crystalline characteristics, morphology and composition of the ZnO nanorod with 60 sec oxygen plasma treatment studied using plane view TEM observations. The bright field image, selected area diffraction (SAD) pattern and high resolution images of the nanorod are shown in Figure 3.2 (b). Figure 3.2 (b) shows that the nanorod has a small tip, which is consistent with the result of SEM observation and the tip angle approximately  $100^\circ$  can be obtained. The SAED pattern (insets in Figure 3.2 (b)) shows the preferred [0001] growth of the ZnO nanorods. The high resolution images shown in insets of figure 3(e) reveal the tip and side of nanorods have lattice planes with interplaner spaces of  $2.54 \text{ \AA}$  and  $2.58 \text{ \AA}$ , respectively, indicating the ZnO nanorods are wurtzite structure with [0001] direction.



It is also observed that the tip area is smooth surface and no crack, indicating that the oxygen plasma treatment is a fast and powerful nanoscale surface modification method. The EDS spectrum shown in Figure 3.2 (c) indicates that the constituent elements of the nanorod are only composed of Zn and O having atomic ratio of Zn/O is 48.7:51.3, which is close to stoichiometric ratio. No evidence of other impurities was found in the EDS spectrum. The Cu and C signals originated from the TEM grid.

Photoluminescence (PL) spectrum is a useful technology for characterizing the optical properties of nanostructures. The room-temperature PL spectra of the as-grown and oxygen plasma etched ZnO nanorod emitters are shown in Figure 3.3. The strong UV emissions for those nanorods occur at about 378 nm, which comes from the recombination of exciton. The broad emission band located at about 550 nm, which is the green emission of the visible spectrum. These peaks occur from the oxygen vacancies of the nanorods<sup>[3.13-3.14]</sup>. It is known that oxygen vacancies are the common defect in n-type ZnO, which are relative to visible emission. From the Figures 3.3, indicate the intensity of visible emission decreases, due to the decrease in oxygen vacancy concentration by oxygen plasma treatment. Inset of Figure 3.3 shows green emission peak intensity decreases, indicating clearly the decreased oxygen vacancy concentration and consequently, the enhanced intensity of UV emission during oxygen plasma treatment occurred. Previously, the reduced oxygen vacancy concentration of ZnO nanorods by annealing at various temperatures in an oxygen atmosphere was reported<sup>[3.15]</sup>. Thus, the reduced green emission is expected to occur by annealing at oxygen atmosphere. In contrast with our case, we were used a simple oxygen plasma treatment, which employed oxygen ion implantation into ZnO nanorods and make reparation the oxygen vacancy of ZnO nanorods and exhibit much better UV emission than the as-grown nanorods.



### 3-3-2 Field emission properties

Figures 3.4 (a) show the J-E curves of the as-grown ZnO and oxygen plasma etched ZnO nanorod emitters. The field emission current–voltage characteristics are analyzed by using the Fowler-Nordheim (F-N) equation<sup>[3.16-3.17]</sup>:

$$J = A \left( \frac{\beta^2 E^2}{\varphi} \right) \exp \left( - \frac{B \varphi^{1.5}}{\beta E} \right) \quad (3-1)$$

Where J is the current density, E the applied electric field,  $A=1.56 \times 10^{-10}$  (AeV/V<sup>2</sup>),  $B=6.83 \times 10^9$  (V/eV<sup>1.5</sup>m),  $\beta$  a field enhancement factor and  $\varphi$  the work function of the emitter. When the work functions of the ZnO is known, the field enhancement factor can be calculated from the slope of the F-N plots (Figure 3.4 (b)). The field emission properties of the nanorods with various Ga/Zn molar ratios in the solutions and different oxygen plasma treatment times are listed in Tables 3.1. Regarding the oxygen plasma treatment, the ZnO nanorod with 60 s treatment shows the best field emission properties. The turn-on field, threshold field, and field enhancement factor are found to be 2.42 V/ $\mu$ m, 3.61 V/ $\mu$ m, and 2268 respectively. Based on Filips model, the  $\beta$  is approximately equal to  $1 + s \frac{d}{r}$ , where s is dependent on screen effect, d the distance between anode and cathode and r the radius of the emitters. In our experiment, the different etched time emitters are considered with the same nanorods number density of 18.5 / $\mu$ m<sup>2</sup> from FE-SEM images and the same distance between tips and anode plate. Clearly, the nanorods with sharp tips have high  $\beta$  values. In our case, the optimum oxygen plasma etched time for the nanorods is 60 s. These nanorod emitters show lower turn-on field, uniform morphology distribution and high crystallinity. On the other hand, the ZnO nanorods with 120 s oxygen plasma treatment show decrease in aspect ratio (c/a) and destruction of nanorods from FE-SEM observation, which would degenerate the field emission properties.

Figures 3.5 (a) and (b) depict the stability characteristics of 10<sup>4</sup> s at 25 °C for the

tip structured ZnO nanorod emitters and show the variations of turn-on field, threshold field and field enhancement factor are  $2.34 \pm 0.21$  V/ $\mu\text{m}$ ,  $3.87 \pm 0.18$  V/ $\mu\text{m}$  and  $2252.8 \pm 107.5$ , respectively. Figure 3.5 (c) depicts the J-E curves for 1<sup>st</sup>, 100<sup>th</sup>, 200<sup>th</sup> and 400<sup>th</sup> operation cycles of these tip structured ZnO nanorod emitters. The stable and reproducible field emission properties can be observed up to 400 cycling tests. After the stability tests, the morphology of nanorod emitters were observed using FE-SEM and it still exhibit the nanotips on the nanorod emitters (shown in Figure 3.5 (d)), imply the tip structured ZnO nanorod emitters provide the enough lifetime and operation cycles for field emission device applications.

Figure 3.6 (a) depicts the J-E curves at temperatures of 25 °C, 50 °C and 100 °C for tip structured ZnO nanorod emitters. It is indicated that the nanorod emitters can be successively and stably operated between the 25 and 100 °C. During the cycling test for 1000 s, the turn-on fields are  $2.33 \pm 0.25$  V/ $\mu\text{m}$ ,  $2.41 \pm 0.33$  V/ $\mu\text{m}$  and  $2.34 \pm 0.16$  V/ $\mu\text{m}$ ; the threshold fields are  $3.86 \pm 0.27$  V/ $\mu\text{m}$ ,  $3.60 \pm 0.47$  V/ $\mu\text{m}$  and  $3.77 \pm 0.18$  V/ $\mu\text{m}$ ; the field enhancement factor are  $2239.0 \pm 115.9$ ,  $2289.5 \pm 141.1$  and  $2216.6 \pm 188.4$  at the 25 °C, 50 °C and 100 °C, respectively, which can be calculated according to the J-E curves and they are shown in Figures 8(b)-(c). According to crystal defect theory, the probability ( $\rho$ ) of oxygen ions to overcome the potential barrier and create vacancies can be expressed as <sup>[3,18]</sup>

$$\rho \approx \nu \exp\left(-\frac{E}{k_B T}\right) \quad (3-2)$$

where  $\nu$  is a characteristic atomic vibrational frequency, E is the potential barrier height and T the temperature. Thus, with an increase of temperature, the probability of defect formation is increased. However, in the present case, the nanorod emitters still exhibit the stable and reversible field emission properties at temperatures 25-100 °C. Thus, oxygen plasma etching process has the advantage of obtaining more

stable field emission characteristic up to 100 °C. This phenomenon may be attributed to decreasing the concentration of oxygen vacancies of the nanorods and obtaining a better crystallinity after the treatment.

### **3-4. Conclusions**

In summary, we successfully enhance the performance of ZnO employing oxygen plasma treatment. The synthesized process is simple, low cost and enable to large scale production. The (002) orientation and tip-structured morphology of the nanorod emitters were proved by XRD pattern, FE-SEM and TEM observations. The PL spectrum reveals that the green emission peak that occurred form oxygen vacancies after oxygen plasma treatment is lowered and obviously this phenomenon is due to reduced the concentration of oxygen vacancies of the nanorod emitters. The tip structured nanorod emitters can be formed after oxygen plasma treatment. Thus, through oxygen plasma treatment, the tip structured ZnO nanorod emitters have enhanced performance including lower turn-on and threshold fields, higher field enhancement factor, good stability characteristics over  $10^4$  s at room temperature. In addition, the tip structured ZnO nanorod emitters can successfully and stably operate up to 100 °C without notable degradation of emission properties. Therefore, these tip structured ZnO nanorod emitters could be used in electron field emission and light emitting applications in the future.

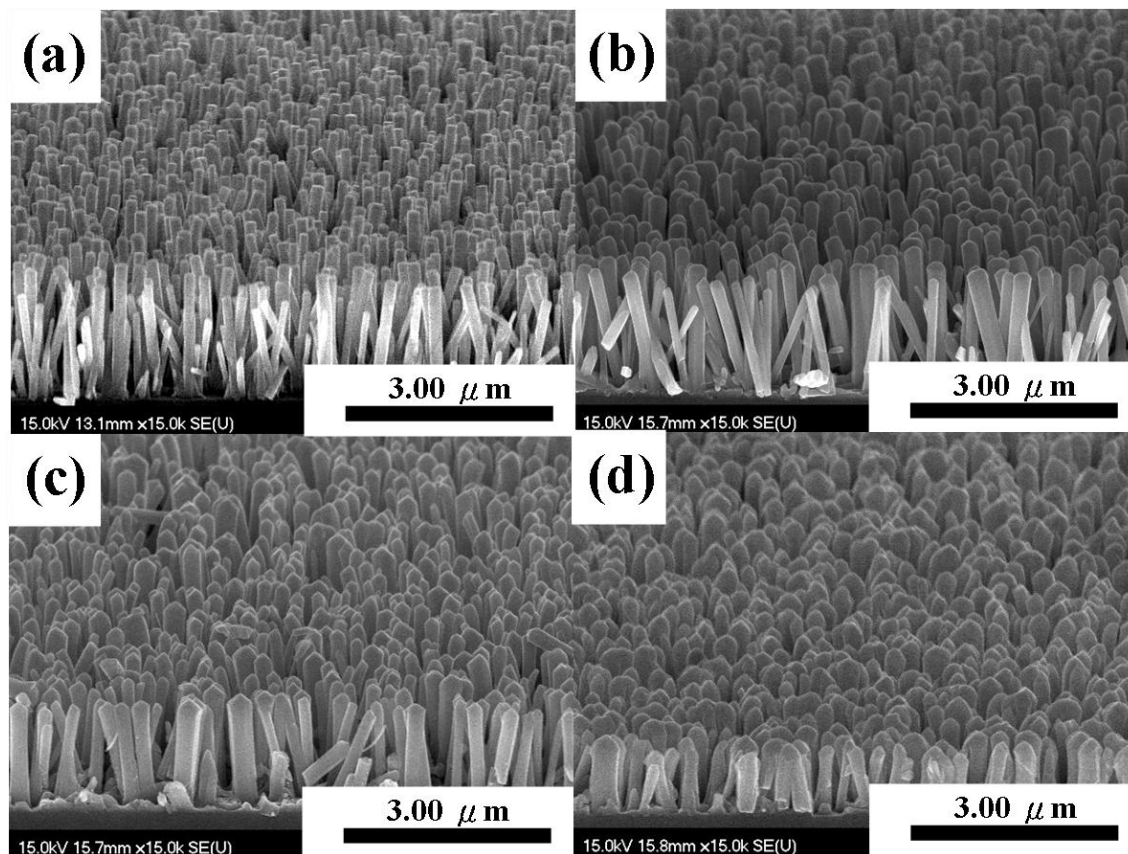


**Figure 3.1** Typical FE-SEM images of ZnO nanorod with various oxygen plasma treatment times (a) 0 s (as-grown), (b) 30 s, (c) 60 s and (g) 120 s. respectively.

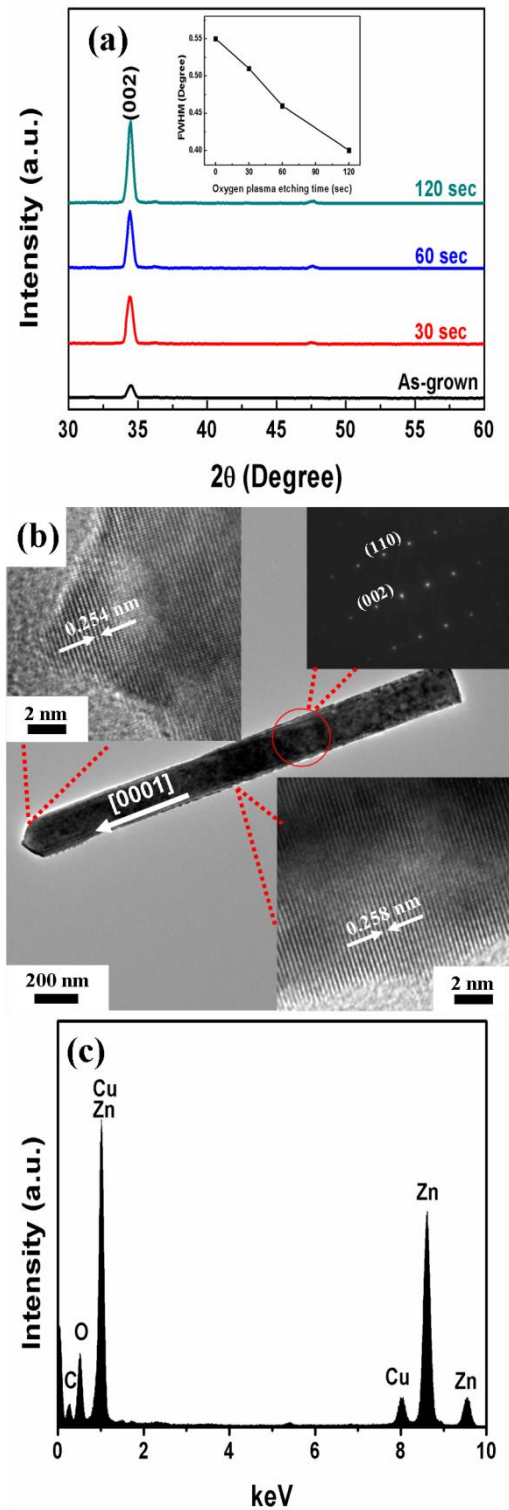


**Figure 3.2** (a) XRD analysis of ZnO nanorod emitters with the various oxygen plasma etching times. (b) TEM bright field image, corresponding SAED pattern, HR-TEM image and (c) EDS analysis of as-grown ZnO nanorod after 60 s oxygen plasma etching.

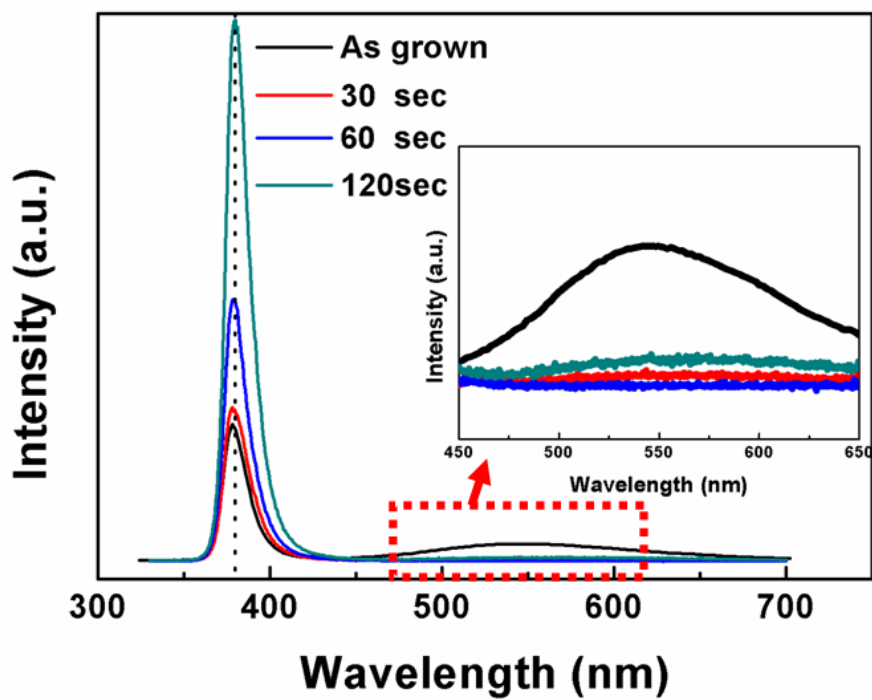


**Figure 3.3** Room temperature PL spectra of ZnO nanorod emitters with the various oxygen plasma etching times (inset show magnify of green emission areas).

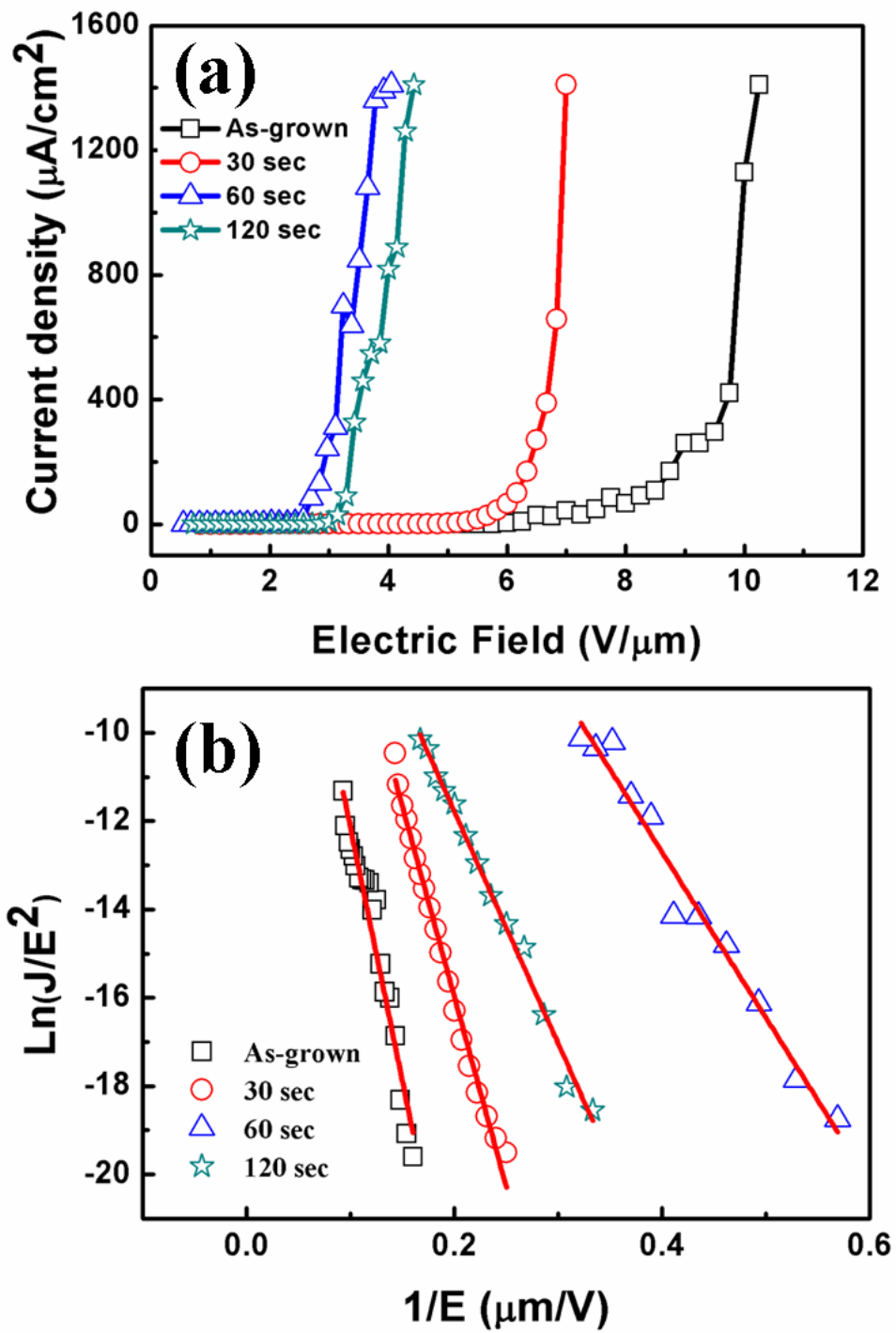


**Figure 3.4** (a) J-E curves and (b) F-N plots of ZnO nanorod emitters with various oxygen plasma treatment times.

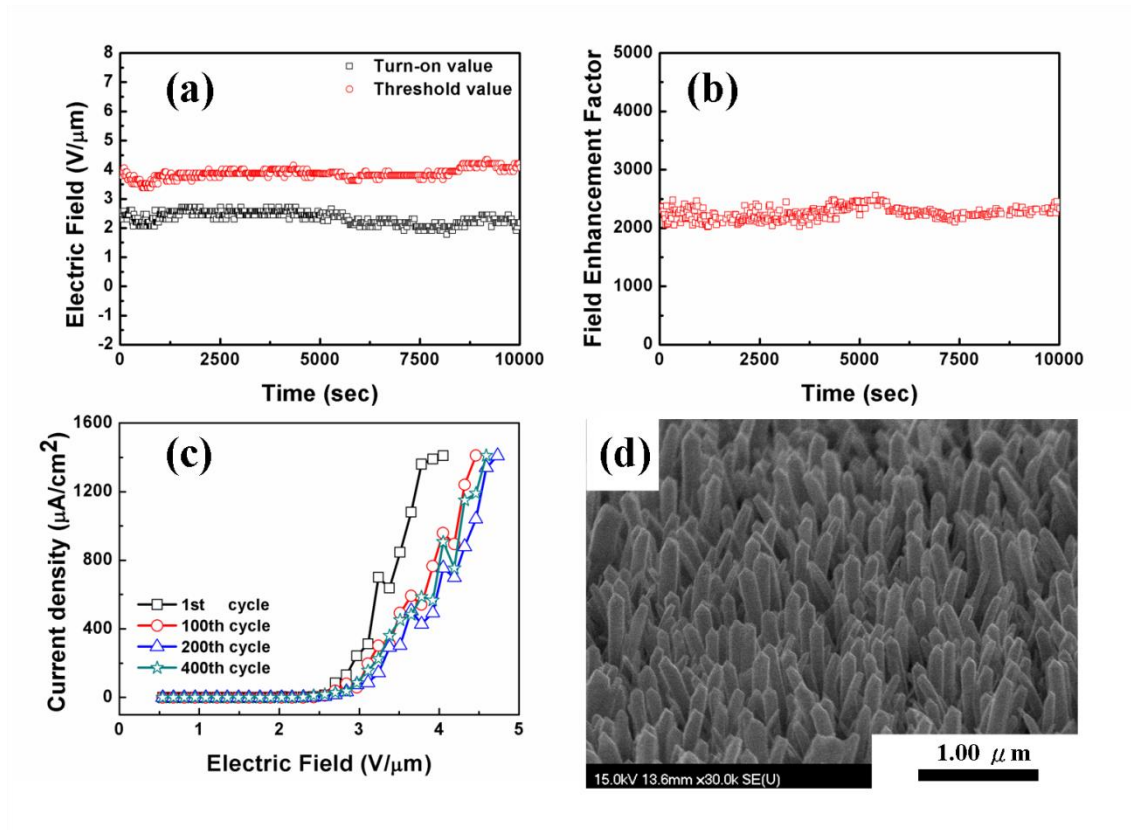


**Figure 3.5** Stability at 25 °C of ZnO nanorod with oxygen plasma etching for 60 s: (a) Turn-on and threshold fields, (b) Field emission enhanced factor, (c) 1<sup>st</sup>, 100<sup>th</sup>, 200<sup>th</sup> and 400<sup>th</sup> cycle respective J-E curves and (d) FE-SEM images of tip structured ZnO nanorod emitters for stability tests.



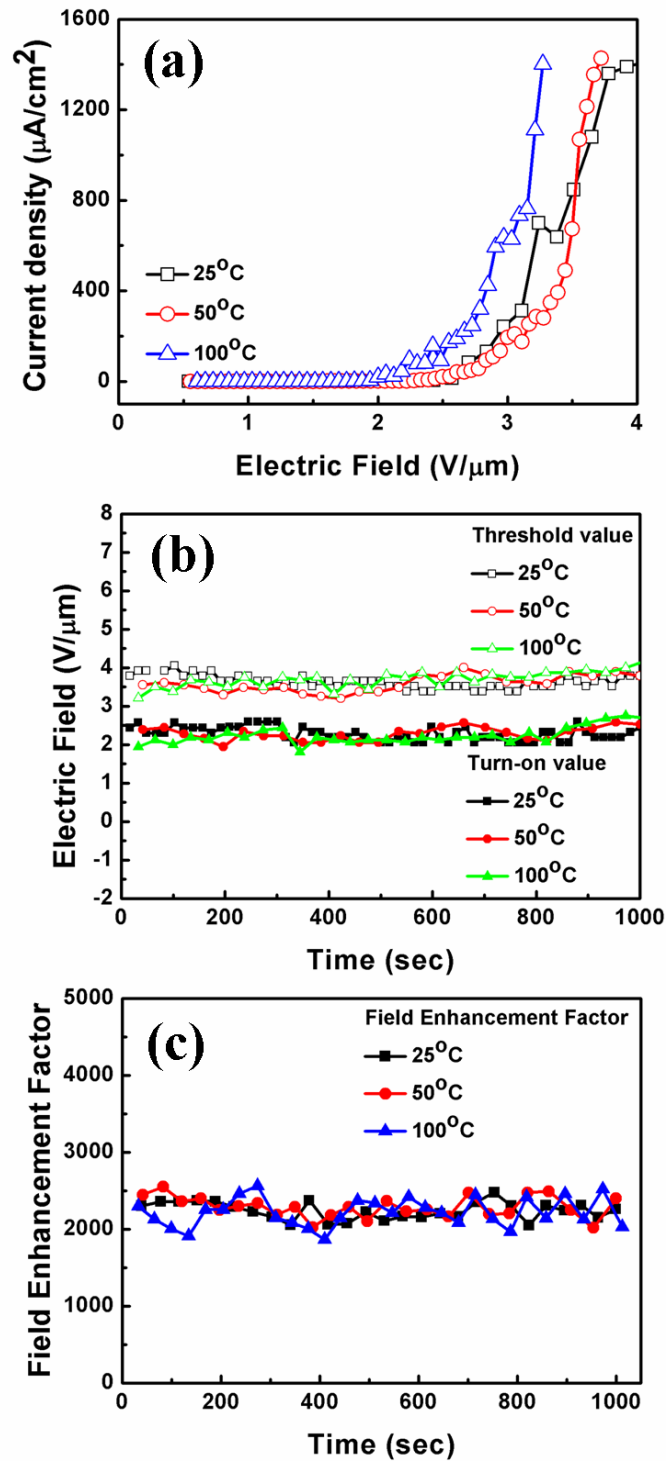


**Figure 3.6** Stability at various temperatures of tip structure ZnO nanorod emitters: (a) J-E curves, (b) Turn-on and threshold fields and (c) Field emission enhancement factor.

# Chapter 4

## Field Emission Properties and Reliability of ZnO Nanorod, Nanopagoda, and Nanotip Current Emitters

### 4-1. Introduction

Zinc oxide (ZnO) nanostructures have demonstrated promising applications in nanodevices such as field emission displays, sensors and other nanodevices <sup>[4.1-4.4]</sup>. Among the various applications, field emission displays have attracted a lot of interest for their high aspect ratio, proper number densities and high emission stability <sup>[4.5]</sup>. Recently, much effort has been made on fabricating special nanorod array type, as it is believed that ZnO nanorods with such geometrical configurations would be more helpful to the emission of electrons than that with the flat ones <sup>[4.6-4.7]</sup>. Thus, it is necessary to control the morphologies of the nanorods to improve their field emission properties. In addition, many surface treatments, such as ion beam sputtering <sup>[4.8]</sup>, hydrogen (H<sub>2</sub>) plasma treatment <sup>[4.9]</sup> and air plasma treatment <sup>[4.10]</sup> have been employed to enhance the field emission properties of ZnO nanostructures. In our previous report, we prepared ZnO nanotip with various tip angles from the as-grown ZnO nanorods by using the combination of chemical etching and plasma treatment <sup>[4.11]</sup>. However, for providing the nanorods with various tip angles, it requires to carefully control the chemical etching conditions such as solution concentration, temperature and etching time to form the convex morphology. Recently, the ZnO nanopagoda arrays have been grown on the silicon substrate by adding L-ascorbic acid or sodium citrate in reaction solution <sup>[4.12-4.13]</sup>. Compared with the chemical etching, the growth direction and the degree of lamination of the ZnO nanostructure was easily

controlled by simply adjusting concentration of L-ascorbic acid or sodium citrate. Such solution synthesis method has high potential for industrial-scale fabrication. In this paper, we synthesized the ZnO nanopagoda emitters by using solution method and employed oxygen plasma etching method to form small tip angle emitters. Electrical, optical and reliability characteristics of those ZnO nanostructures are also investigated.

## 4-2. Experimental method

P-type Si (100) substrate was cleaned by a standard Radio Corporation of America (RCA) method. Subsequently, the epitaxial ZnO buffer layer was deposited by rf-sputtering and followed by in-situ annealing at 750 °C for 30 min. Unless specified, the aqueous synthesis was carried out at 90 °C in a sealed kettle placed in a quartz beaker. The pre-modified substrates were immersed and downward growth in precursor solution for 1 h to form the basic nanorod arrays. The precursor solution was prepared by mixing 0.05 M zinc nitrate hexahydrate ( $\text{Zn}(\text{NO}_3)_2 \cdot 6\text{H}_2\text{O}$ , 99.9% purity) and 0.05 M methenamine ( $\text{C}_6\text{H}_{12}\text{N}_4$ , 99.9% purity). For making the nanorods with pagoda morphologies, the substrate with the basic nanorod arrays was placed downward near the surface of chemical solution and heated to about 90 °C for 3 h. This solution contains 0.02 M zinc nitrate hexahydrate ( $\text{Zn}(\text{NO}_3)_2 \cdot 6\text{H}_2\text{O}$ , 99.9% purity), 0.02 M methenamine ( $\text{C}_6\text{H}_{12}\text{N}_4$ , 99.9% purity) and  $2.75 \times 10^{-4}$  M L-ascorbic acid ( $\text{C}_8\text{H}_8\text{O}_6$ , 99% purity). After the reaction, the substrate was bonded on a sputtering Al target by carbon tape and exposed to oxygen plasma for 30 s to form the ZnO nanotip structure. For the plasma treatment, process pressure and rf-power were maintained at  $5 \times 10^{-2}$  Torr and 30 W, respectively.

The morphology, size distribution and crystal structure of the ZnO nanorod, nanopagoda and nanotip emitters were investigated by a field-emission scanning

electron microscope (FE-SEM, Hitachi S-4700I), a transmission electron microscope (TEM, JEOL 2100F) and a X-ray diffractor (XRD, Bede D1), respectively. The field-emission current-voltage (I-V) curves of the ZnO emitters were measured in the turbo pump vacuum chamber at a pressure of  $2 \times 10^{-6}$  Torr. A copper tip was employed to act as an anode with the tip area of  $7.09 \times 10^{-3}$  cm<sup>2</sup>. We used micrometer (accuracy of  $\pm 1$   $\mu$ m) to adjust the distance between a copper anode and the emitters. The distances between the ZnO emitters and the anode are 100, 250 and 250  $\mu$ m, respectively. The field emission properties are affected by the anode area and anode-cathode distance based on Filips model<sup>[4,14]</sup>. The turn-on and threshold fields are defined at current densities of 1  $\mu$ A/cm<sup>2</sup> and 1 mA/cm<sup>2</sup>, respectively. The dependence of the field emission current on the anode-cathode voltage was recorded using programmable Keithley 237 picoammeter measurement system. The stability measurements were also carried out for the ZnO nanotip emitters at temperatures of 25, 50 and 100 °C, respectively. The photoluminescence (PL) spectra were obtained using a He-Cd laser (325nm) as excitation source at room temperature.

### **4-3. Results and discussion**

#### ***4-3-1. Morphology, crystal structure, composition and optical properties of ZnO nanorod, nanopagoda and nanotip array***

Figure 4.1 (a) shows the XRD spectra of the ZnO nanorod, nanopagoda and nanotip emitters, respectively. Diffraction peaks in the XRD patterns for all the ZnO nanostructures can be indexed as wurtzite hexagonal structure (JCPDS-ICDD-2003 No.89-1937,  $a=0.3253$ nm and  $c=0.5209$ nm) and they exhibit the (002) highly preferred orientation. No characteristic diffraction peaks from impurities were detected. The morphologies of the ZnO nanostructures were observed using FE-SEM

and their typical images are shown in Figures 4.1 (b)-(d). The ZnO nanorod arrays are vertically well-aligned with diameters in the range of 120-220 nm (inset of Figure 1 (b)), 940-1030 nm in length and relatively high number density (85 emitters/ $\mu\text{m}^2$ ). The top of nanorods grown in the second aqueous solution growth (addition of  $2.75 \times 10^{-4}$  M L-ascorbic acid in the reaction solution) becomes tower-shaped morphology (nanopagoda) as shown in Figure 4.1 (c). The tip width and base diameter of the laminated nanopagodas are about 30-50 and 500-650 nm (inset of Figure 4.1 (c)), respectively. Figure 4.1 (d) indicates that the ZnO nanotip emitters can be easily sharpened and exhibit a tip angle approximately  $20^\circ$  by oxygen plasma treatment for 30 s. The edge area of the emitters is smooth surface (Figure 4.1 (d)), indicating that the oxygen plasma treatment is a fast and powerful nanoscale surface modification method.

In the previous works, L-ascorbic acid acted as reduction reagent in the synthesis solution for metal nanostructures [4.12-4.13]. The growth direction and the degree of lamination of the ZnO nanostructure can be controlled by changing the concentration of L-ascorbic acid. The schematic descriptions of ZnO nanopagoda and nanotip formations are shown in Figure 4.2. One-dimensional ZnO nanorods are easily grown along c-axis of the wurtzite crystal, which has a hexagonal structure with six nonpolar  $\{10\bar{1}0\}$  prismatics capped by polar zinc (positive)  $[0001]$  and oxygen (negative)  $[000\bar{1}]$  basal surfaces (Figure 4.2 (a)) [4.13, 4.15]. Each plane of the pentagon in a structure of L-ascorbic acid has two hydroxyls (O-H) and carbon-oxygen double bond (C=O) (Figure 4.2 (b)). This bottom plane structure has four lone paired electrons on the four oxygen atoms. These lone paired electrons are easily bonded on the polar zinc surface by electrostatic force and inhibit the  $[0001]$  direction crystal growth to form the pagoda morphology (Figure 4.2 (c)). Finally, we perform the oxygen plasma etching

on this nanopagoda structure to form the nanotip emitters as shown in Figure 4.2 (d).

The crystalline properties and morphologies of the nanopagoda and nanotip were studied using TEM observations. The cross section images, selected area electron diffraction (SAED) patterns of the nanopagoda and nanotip are shown in Figures 4.3 (a) and (b), respectively. Significant differences between the cross section images of the nanopagoda and nanotip, confirm the successful change in the edge morphology of nanopagoda by oxygen plasma etching. Figure 4.3 (b) reveals that the nanotip has a small tip angle of  $20^\circ$ , which is consistent with the result of SEM observation (Figure 4.1 (d)). The clear lattice images indicate that the interplanar spacing of the (002) plane of ZnO nanopagoda and nanotip is 0.53 nm (insets in Figures 4.3 (a) and (b)), which is consistent with that of the International center for Diffraction Data (JCPDF-ICDD-2003) database No.89-1397 of ZnO. The SAED patterns (insets in Figures 4.3 (a) and (b)) identify the ZnO nanopagoda and nanotip growth along the [0001] direction, which agree with the result from XRD (Figure 4.1 (a)).

Figure 4.4 shows the room-temperature PL spectra of the ZnO nanorod, nanopagoda and nanotip emitters. The strong UV emissions for those emitters occur at about 378 nm, which comes from the recombination of exciton. The broad emission band located at about 550 nm is the green emission of the visible spectrum. The green emission spectra shown in the inset of Figure 4.4 occur from oxygen vacancies existed in the emitters<sup>[4.16]</sup>. The nanotip emitter has the lowest green emission intensity and the highest UV emission peak intensity among them, indicating clearly the decreased oxygen vacancy concentration occurred after oxygen plasma treatment.

#### ***4-3-2 Field emission properties***

Figure 4.5 (a) show the J-E curves of emitters. The ZnO nanorod, nanopagoda

and nanotip emitters have turn-on electric fields of 6.01, 1.46 and 1.07 V/ $\mu\text{m}$  at a current density of 1  $\mu\text{A}/\text{cm}^2$  and threshold electric fields of 10.00, 2.32 and 1.63 V/ $\mu\text{m}$  at a current density of 1  $\text{mA}/\text{cm}^2$ , respectively. The field emission current–voltage characteristics are analyzed by using the Fowler-Nordheim (F-N) equation<sup>[4.14, 4.17]</sup>:

$$J = A \left( \frac{\beta^2 E^2}{\phi} \right) \exp \left( - \frac{B \phi^{1.5}}{\beta E} \right) \quad (4-1)$$

$$\ln \left( \frac{J}{E^2} \right) = \ln \left( \frac{A \beta^2}{\phi} \right) - \frac{B \phi^{1.5}}{\beta E} \quad (4-2)$$

Where J is the current density, E the applied electric field,  $A=1.56 \times 10^{-10}$  ( $\text{AeV}/\text{V}^2$ ),  $B=6.83 \times 10^9$  ( $\text{V}/\text{eV}^{1.5}\text{m}$ ),  $\beta$  the field enhancement factor and  $\phi$  the work function of the emitters. When the work function of the ZnO is 5.37 eV, the  $\beta$  values can be calculated from the slopes of the F-N plots (inset in Figure 4.5 (a)), which are 1057, 3681 and 4735 for nanorod, nanopagoda and nanotip, respectively. Based on Filips model, the  $\beta$  is approximately equal to  $1 + s \frac{d}{r}$ , where s is dependent on screening effect, d the distance between anode and cathode and r the radius of the emitters. The smaller tip angle and uniform morphology distribution would lead to larger  $\beta$  value. In our experiment, the nanopagoda and nanotip emitters exhibit the smaller tip angle and lower emitter number density (10 emitters/ $\mu\text{m}^2$ ) than the nanorod emitters (85 emitters/ $\mu\text{m}^2$ ). The better field emission performance of the nanopagoda and nanotip emitters is due to the minimized screening effect between the neighboring emitters (that is, low number density). The effective electric field at the top of the emitters can be reduced if the neighboring emitters are too close to each other. Nilsson et al. reported that 0.25 emitters / $\mu\text{m}^2$  is the optimal number density for the 1 $\mu\text{m}$  height CNT arrays<sup>[4.18]</sup>. According to their simulation results, to minimize the screening effect, the optimal distance between two adjacent emitters should be two times of the height of the emitters. In our experiment, the ratios of emitter's distance to emitter's length are approximately  $0.05 \pm 0.01$ ,  $0.63 \pm 0.04$  and  $0.65 \pm 0.03$

times of the height of the nanorod, nanopagoda and nanotip emitters, respectively. Through L-ascorbic acid added in the chemical solution, the nanopagoda and nanotip emitters can decrease their screening effect and reveal lower turn-on fields and higher field enhancement factors. When the nanotip emitters have the same number density ( $10 \text{ emitters}/\mu\text{m}^2$ ) and similar screening effect with the nanopagoda emitters, the smaller tip angle ( $20^\circ$ ) of the nanotip emitters would lead to have larger  $\beta$  value and lower turn-on field in comparison with nanopagoda emitters. Figures 4.5 (b) and (c) depict the stability characteristics of  $2 \times 10^4 \text{ s}$  at  $25^\circ\text{C}$  for the ZnO nanopagoda and nanotip emitters. It also shows the variations of turn-on fields:  $1.63 \pm 0.17$  and  $1.05 \pm 0.06 \text{ V}/\mu\text{m}$ ; threshold fields:  $2.15 \pm 0.27$  and  $1.64 \pm 0.07 \text{ V}/\mu\text{m}$ ; current densities at the threshold fields:  $993.84 \pm 98.52$  and  $989.33 \pm 53.45 \mu\text{A}/\text{cm}^2$  for the nanopagoda and nanotip emitters, respectively. The turn-on, threshold fields and current densities of the nanotip emitters reach more stable values in comparison with those of the nanopagoda emitters. Because the nanopagoda and nanotip emitters have the same number density ( $10 \text{ emitters}/\mu\text{m}^2$ ) and consequently, similar screening effect, we believe that the larger variations in the turn-on, threshold field and current density are due to the hexagon edge area from the ZnO nanopagoda emitters (Figures 4.1 (c) and (d)), which would produce many emission points on the emitters leading to larger variations in those properties. Figures 4.5 (b) and (c) reveal the nanotip emitters with smooth surface exhibit small variation of turn-on and threshold fields, less than  $0.07 \text{ V}/\mu\text{m}$  and stable current density during  $2 \times 10^4 \text{ s}$  measurement. Figure 4.6 (a) depicts the J-E curves at temperatures of  $25$ ,  $50$  and  $100^\circ\text{C}$  for the nanotip emitters. It is indicated that the nanotip emitters can be successively and stably operated between  $25$  and  $100^\circ\text{C}$ . During the cycling test for  $5000 \text{ s}$ , the turn-on fields:  $1.10 \pm 0.03$ ,  $0.93 \pm 0.05$  and  $0.95 \pm 0.04 \text{ V}/\mu\text{m}$ ; the threshold fields:  $1.67 \pm 0.05$ ,  $1.64 \pm 0.06$  and  $1.63 \pm 0.05 \text{ V}/\mu\text{m}$  at the  $25$ ,  $50$  and  $100^\circ\text{C}$ , respectively (Figure 4.6 (b)), calculated



from their J-E curves. Figure 4.6 (c) shows the current density (threshold field) as a function of time at temperatures indicated. The current densities are  $989.74 \pm 48.22$ ,  $988.13 \pm 50.73$  and  $993.56 \pm 58.48$   $\mu\text{A}/\text{cm}^2$  at 25, 50 and 100 °C, respectively. No obvious degradation of current densities is observed at those measured temperatures. Thus, our ZnO nanotip emitters obviously exhibit the stable and reproducible field emission properties at temperatures 25-100 °C. This behavior is proposed to be attributed to reduced oxygen vacancy concentration, small tip angle of 20°, smooth edge surface of the emitter and a better crystallinity obtained for ZnO nanotip emitters after the oxygen plasma etching process.

#### 4-4. Conclusions

The ZnO nanotip emitters were successfully fabricated by employing the combination of chemical solution growth and oxygen plasma treatment. The synthesized process is simple, fast, low cost and enable to large scale production. The nanotip emitters exhibit the (002) highly preferred orientation and small tip angle morphology proved by XRD, FE-SEM and TEM observations, respectively. The nanotip emitters have turn-on field of 1.07 V/ $\mu\text{m}$ , threshold electric field of 1.63 V/ $\mu\text{m}$ , field enhancement factor of 4735 and also exhibit stable and reproducible field emission properties at 25-100 °C. Such good performance is attributed to reduced oxygen vacancy concentration, better crystallinity, small tip angle of 20° and smooth edge surface of the emitters after the oxygen plasma etching process. The ZnO nanotip emitters have high potential for applications in electron field emission and light emitting devices in the future.

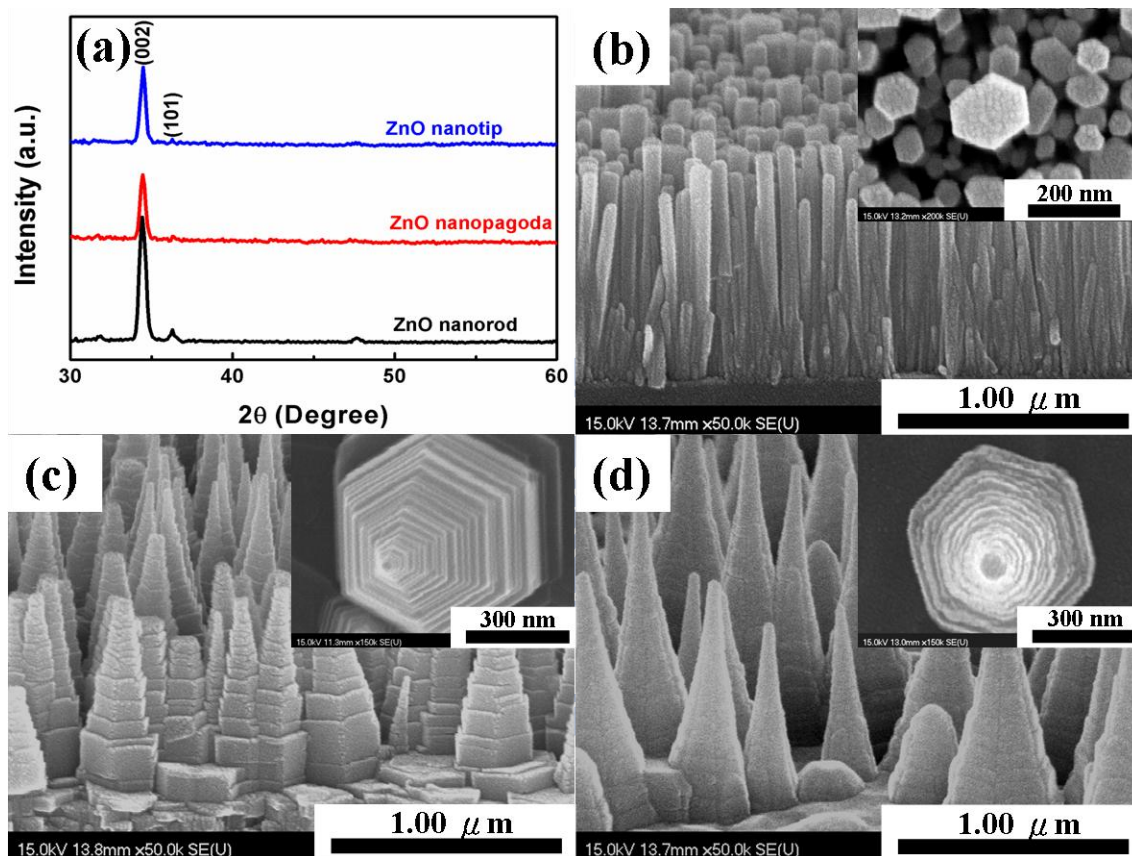


**Figure 4.1** (a) XRD analysis of ZnO nanorod, nanopagoda, and nanotip emitters. Typical FE-SEM images of (b) nanorod, (c) nanopagoda, and (d) nanotip emitters; (insets of (b), (c) and (d) are their top view images).

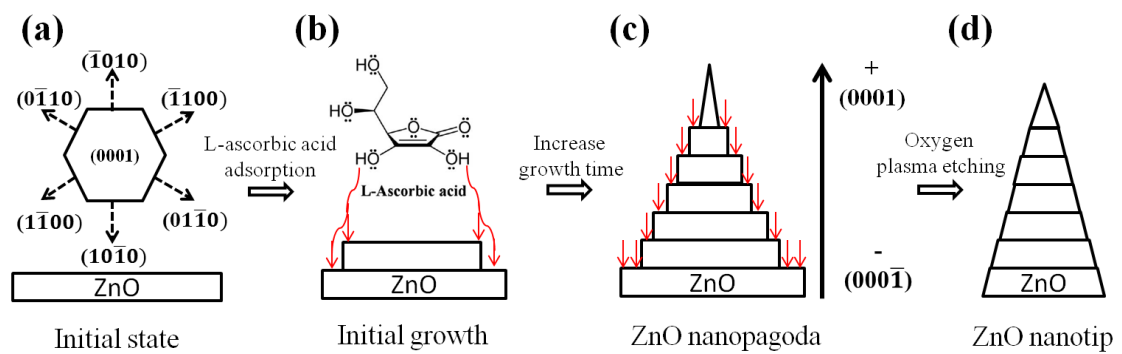


**Figure 4.2** Schematic descriptions of the formations of ZnO nanopagoda and nanotip emitters.

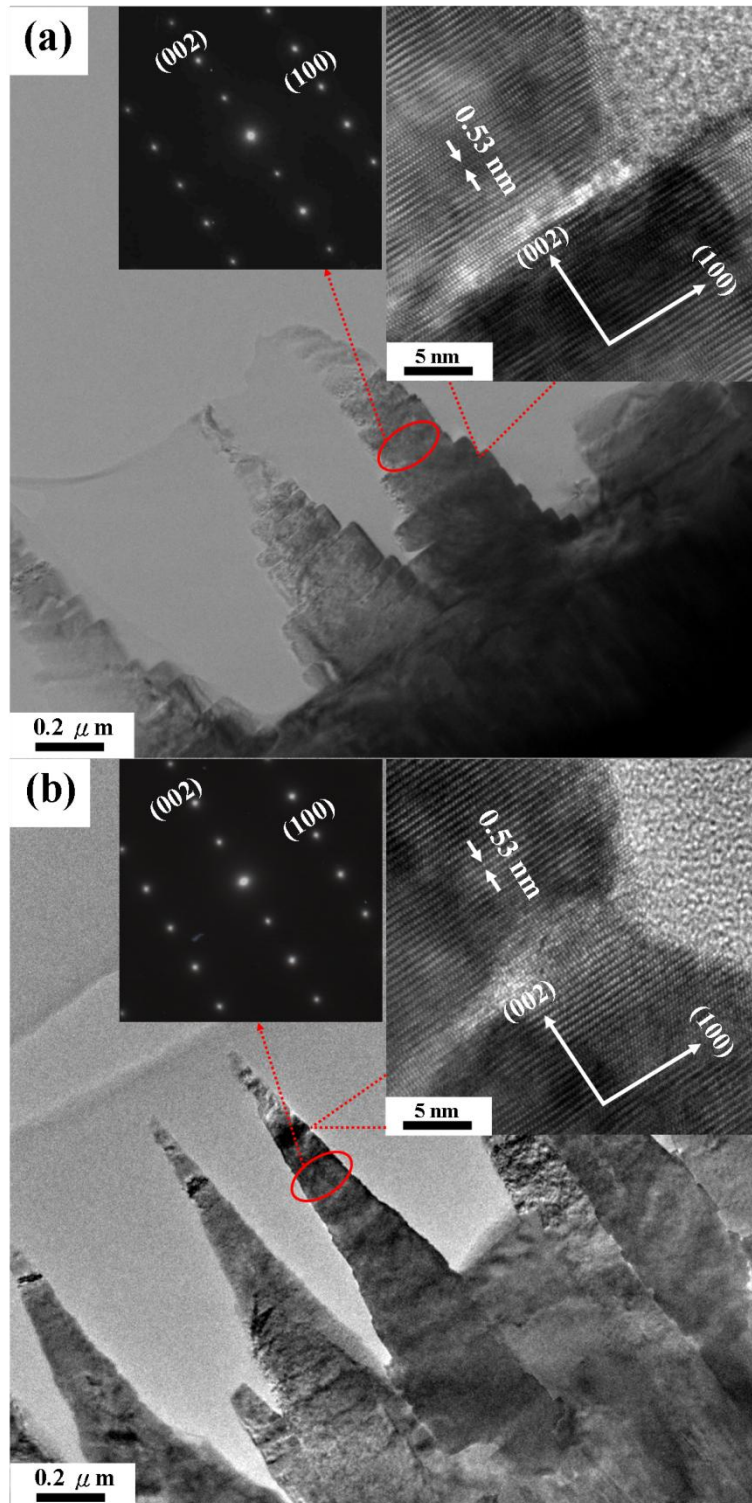


**Figure 4.3** TEM cross section images, corresponding SAED patterns and HR-TEM images of (a) ZnO nanopagoda and (b) ZnO nanotip emitters.

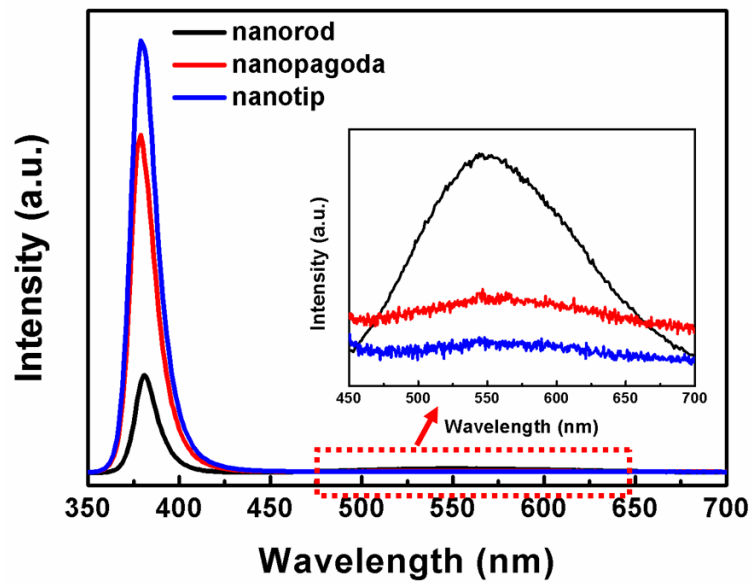


**Figure 4.4** Room temperature PL spectra of ZnO nanorod, nanopagoda, and nanotip emitters.

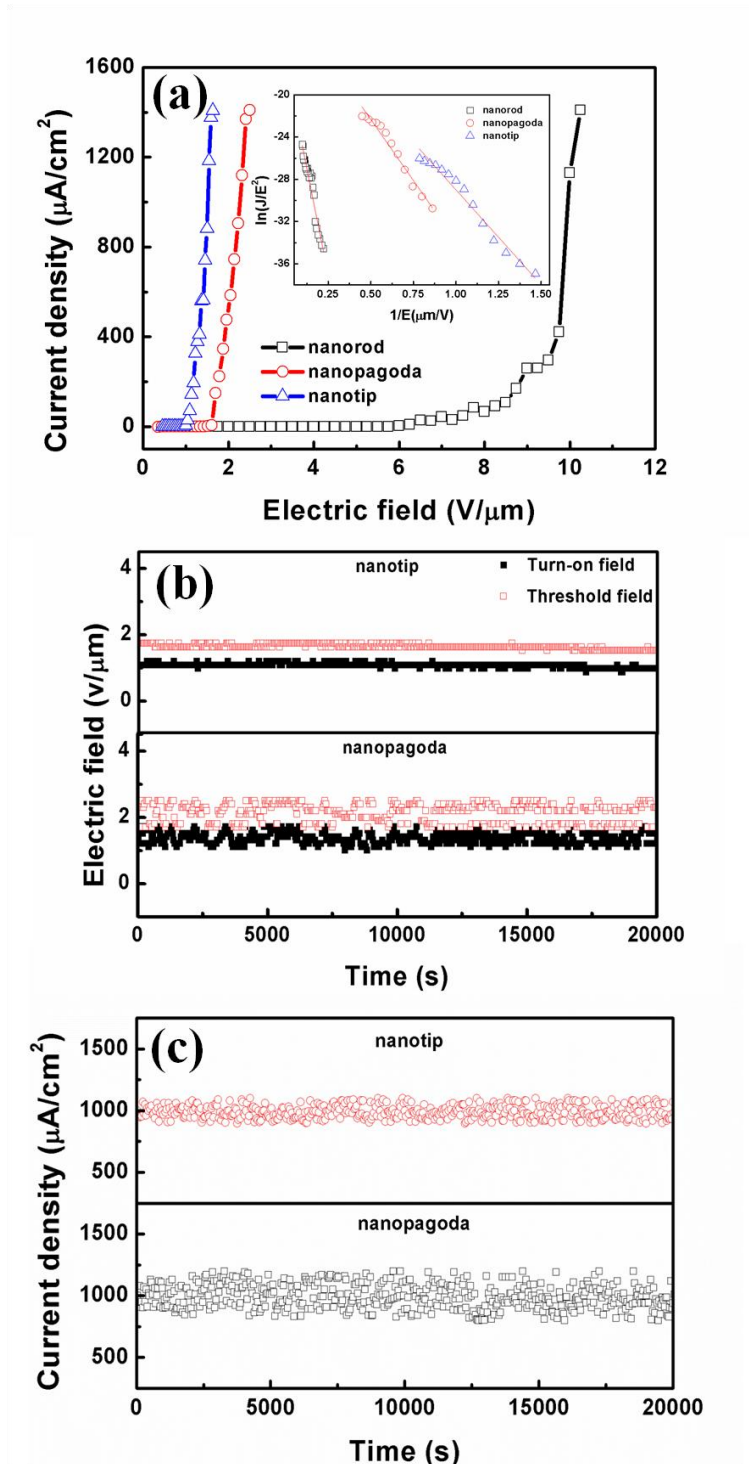


**Figure 4.5** (a) J-E curves (inset shows the F-N plots) of ZnO nanorod, nanopagoda, and nanotip emitters. (b) Stability at room temperature of ZnO nanopagoda and nanotip emitters.

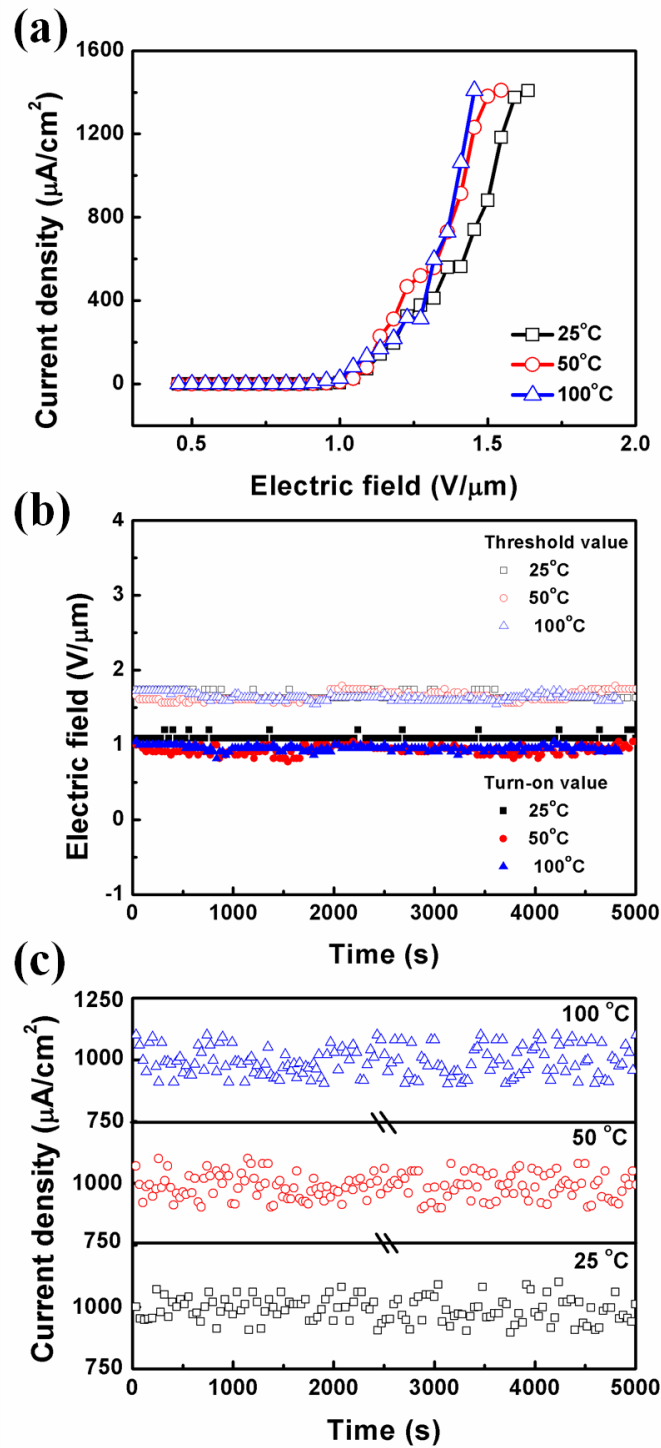


**Figure 4.6** Stability at various temperatures of ZnO nanotip emitters: (a) J-E curves and (b) turn-on and threshold fields.



# Chapter 5

## Hydrogen Gas Sensors using ZnO-SnO<sub>2</sub> Core-Shell Nanostructure

### 5-1. Introduction

Recently, metal oxide semiconductors sensor has been attracted considerable attention because of their potential application in environment, medicine and chemical process controlling. The most advantages of metal oxide semiconductors are low cost, no environment pollution and compatibility with the silicon-based technology. Up to now, numerous metal oxide semiconductors, including SnO<sub>2</sub> [5.1-5.2], TiO<sub>2</sub> [5.3], CeO<sub>2</sub> [5.4], Ba<sub>0.5</sub>Sr<sub>0.5</sub>TiO<sub>3</sub> [5.5], and ZnO [5.6-5.8] have been used for gas sensor. Among them, ZnO and SnO<sub>2</sub> are chemically stable n-type semiconductors and with wide direct band gaps at room temperature of 3.37 and 3.60 eV [5.9-5.11], respectively, and their electrical transport is highly dependent on the adsorption/desorption gas molecules. In recent years, various forms of ZnO and SnO<sub>2</sub>-based gas sensors including thick film, thin film, heterojunction, nanoparticle and nanowire [5.12-5.16] have all been fabricated and demonstrated that ZnO and SnO<sub>2</sub> are very sensitive to reducing gases.

In addition to metal oxide gas sensors, several nanocomposite gas sensors were also reported in the literature. Chang *et al* reported that a ZnO-Au nanoparticle composite sensor was made by using UV light to absorb Au particles onto the ZnO nanowire and its device sensitivity at 350°C was enhanced from 4.2 to 46.5% at 50 ppm CO [5.6]. Mesoporous ZnO-SnO<sub>2</sub> (m-Z-S) nanofibers fabricated via simple electrospinning were reported to exhibit high sensitivity and good reproducibility in the range of 3-500 ppm ethanol [5.9]. In addition, the Fe<sub>2</sub>O<sub>3</sub>-ZnO nanocomposite sensor



showed fairly excellent sensitivity and selectivity to  $\text{NH}_3$  at room temperature. Its response time and recovery time of the sensor were less than 20 sec<sup>[5,17]</sup>. Obviously, the sensing properties were demonstrated to be improved through nanocomposite form based on above previous results. However, the sensing properties of core-shell nanostructures have received scarce attention.

In this chapter, the vertically well-aligned ZnO nanowires were grown on ZnO/Si substrate using an aqueous solution method and then the uniform  $\text{SnO}_2$  shell layer on the surface of ZnO core nanowire nanostructure was formed by spin coating method. The structure, morphology and physical properties of the ZnO- $\text{SnO}_2$  core-shell nanowires and their hydrogen gas sensing properties were investigated.

## 5-2. Experimental method

The p-type Si (100) substrate was cleaned by a standard RCA cleaning method and then rinsed in Buffered Oxide Etch (BOE) solution for 30 sec to remove native oxide from the surface of Si substrate. Subsequently, the epitaxial ZnO buffer layer was deposited by rf-sputtering and followed by in-situ annealing at 750 °C for 30 min. After annealing, the thickness of the epitaxial ZnO buffer layer was about 100 nm. Unless specified, the ZnO nanowire aqueous solution synthesis was carried out at 90 °C in a sealed kettle placed in a quartz beaker. The pre-modified substrate was immersed in the first precursor solution for 3 h, which was prepared by mixing 0.025 M zinc chloride ( $\text{ZnCl}_2$ ) with ammonia water ( $\text{NH}_4\text{OH}$ ). After the aqueous solution synthesis, the ZnO nanowires were grown on the pre-modified substrate. In the second step, the as-grown nanowires were spin-coated with 0.001M  $\text{SnCl}_4$  solution and then heat treated at 325°C above the decomposition temperature of  $\text{SnCl}_4$  for 4 h in air ambient to form  $\text{SnO}_2$  layer. The as-grown ZnO nanowires were repeatedly spin-coated for 5 times (ZnO- $\text{SnO}_2$ -5), 10 times (ZnO- $\text{SnO}_2$ -10) and 20 times

(ZnO-SnO<sub>2</sub>-20), respectively, to obtaining various thickness SnO<sub>2</sub> shell layers. The thickness of the SnO<sub>2</sub> layers was determined using TEM analysis.

. The morphology, size distribution and crystal structure of the as-grown ZnO and the ZnO-SnO<sub>2</sub> core-shell nanowires were analyzed using field-emission scanning electron microscope (FE-SEM, Hitachi S-4700I) and transmission electron microscope (TEM, JEOL 2100F). The chemical composition was estimated by energy dispersive X-ray spectrometer (EDS, Oxford ISIS300) and X-ray photoelectron spectroscopy (XPS, Microlab 350).

For electrical measurement, silver paste was applied on top surfaces of the sample and fired at 650 °C for 30 min as the electrode. The composition, morphology and crystal structure of the samples before and after making electrode for nature were found to be similar. The resistance varied with H<sub>2</sub> concentration of the as-grown ZnO and the ZnO-SnO<sub>2</sub> core-shell nanowires was measured at 250 °C through two probe method by using a computer-controlled gas sensing test system. The H<sub>2</sub> gas was controlled over 25, 50, 100 and 200 ppm using mass flow controller (MFC, Brooks 5850E).

### **5-3. Results and discussion**

#### ***5-3-1 Crystal structure, morphology and chemical composition of as-grown ZnO and ZnO-SnO<sub>2</sub> core-shell nanowires***

Figure 5.1 (a) reveals the typical FE-SEM image of the ZnO nanowires synthesized by solution method. The nanowires vertically well-aligned grown on the ZnO film/Si substrate have an average diameter of 130±11.7 nm and length of 3.8±0.65µm. The FE-SEM images display the ZnO-SnO<sub>2</sub> core-shell nanostructures prepared with repeatedly spin-coated 5 times, 10 times and 20 times (Figure 5.1

(b)-(d)). They reveal that the SnO<sub>2</sub> shell layer uniformly covers the surface of the ZnO core nanowires and the shell thickness on a nanometer scale is varied with the spin-coated time.

The crystalline characteristics and morphology of the as-grown ZnO nanowires and ZnO-SnO<sub>2</sub> core-shell nanowires after annealed at 650 °C, 30 min were studied using TEM analysis. The bright field images, EDS analysis and selected area diffraction (SAD) pattern of the as-grown ZnO nanowires are shown in Figure 5.2 (a). From the bright field images (Figure 5.2 (a)) the nanowires are needle-like with a diameter of 30 nm at the tip and 100 nm in the middle. They are only composed of Zn and O and no evidence of other impurities is found in the EDS spectrum. The Cu signals originate from the TEM grid. Figure 5.2 (b) clearly reveals that the SnO<sub>2</sub> shell layer is uniformly grown on the surface of the ZnO core nanowires. A clear Sn peak is observed in the EDS spectrum of ZnO-SnO<sub>2</sub>-20 nanowires (inset of Figure 5.2 (b)). The SAED pattern of ZnO-SnO<sub>2</sub>-20 nanowires indicates that not only has single crystal from ZnO nanowire, but also has amorphous structure attributed to SnO<sub>2</sub> shell layer (inset of Figure 5.2 (b)). Therefore, the SnO<sub>2</sub> layer has successfully been synthesized onto the surface of the ZnO nanowires. Figure 5.3 (a)-(d) show the high resolution images of ZnO-SnO<sub>2</sub>-5, ZnO-SnO<sub>2</sub>-10 and ZnO-SnO<sub>2</sub>-20 nanowires. They indicate that the thickness of synthesized SnO<sub>2</sub> shell layers increase from 2.5 to 9.0 nm as the spin-coated time increased from 5 to 20 times. They also depict that the SnO<sub>2</sub> shell layer is amorphous structure in nature, which is consistent with the result from SAD pattern.

The XPS spectra (Figure 5.4 (a) and (b)) show that there are feature peaks corresponding to elements of Zn and O. Three strong peaks located at 531.5, 1022.2 and 1045.2 eV are, respectively, due to the O (1s) and Zn (2P<sub>3/2</sub> and 2p<sub>1/2</sub>) binding energies for as-grown nanowires. In the Figure 5.4 (c), the two peaks located at 495.3

and 486.3 eV can be assigned to Sn 3d<sub>3/2</sub> and Sn 3d<sub>5/2</sub>, whose gap between two peaks is 9 eV, that is consistent with the reference value of SnO<sub>2</sub><sup>[5,18]</sup>. Compared as-grown nanowires with ZnO-SnO<sub>2</sub>-20 core-shell nanowires, it is observed that the peak shifted from 531.5 eV to 530.3 eV of O 1s peaks is attributed to oxygen in SnO<sub>2</sub>. Therefore, XPS result analysis reveals that a SnO<sub>2</sub> shell layer is indeed coated on the surface of the ZnO nanowire.

### ***5-3-2 Gas sensing properties of as-grown ZnO and ZnO-SnO<sub>2</sub> core-shell nanowires***

The most widely accepted model for gas sensing behaviors in previous reported work is based on the modulation of the depletion layer by oxygen absorption. It is well known that oxygen molecules in an air environment are adsorbed onto the surface of the oxide semiconductor nanowires to be ionized to O<sub>2</sub><sup>-</sup>, O<sup>-</sup> and O<sup>2-</sup> ions by extracting electron from the conduction band of the oxides. The degree of ionization depends on the temperature<sup>[5,19-5,21]</sup>. O<sub>2</sub><sup>-</sup> is chemisorbed at low temperature (commonly below 100°C) while O<sup>-</sup> and O<sup>2-</sup> are chemisorbed at high temperature (commonly above 100°C). As a result, depletion layer is formed on the surface of the oxide nanowires, leading to a decrease of the carrier concentration in an air environment. When the sensors are exposed to a reducing gas, such as CO, NH<sub>3</sub> and H<sub>2</sub>, they release the trapped electrons back to the conduction band when the reducing gas reacts with the adsorbed oxygen molecules, thus increasing of the carrier concentration of the nanowires. Therefore, the resistance of nanowires would decrease as reaction with reducing gas. The reaction between reducing gas and nanowires can be described by:



where R is the reducing gas such as H<sub>2</sub> and CO.

The above as-grown and ZnO-SnO<sub>2</sub> core-shell nanowires were fabricated as gas sensors. Their gas sensing characteristics in various concentrations of H<sub>2</sub> were investigated and compared. Figure 5.5 (a)-(d) show the dynamic H<sub>2</sub> sensing properties of the as-grown ZnO nanowires and ZnO-SnO<sub>2</sub>-5, ZnO-SnO<sub>2</sub>-10 and ZnO-SnO<sub>2</sub>-20 core-shell nanowires, respectively, at 250 °C in various concentrations of H<sub>2</sub> gas indicated. It is found that the resistance increases in air and subsequently decreases at various H<sub>2</sub> concentrations for these four type nanowires. The reproducible and stable sensing characteristics can be obtained. The sensitivity of nanowires gas sensor is defined as

$$\text{Sensitivity} = \frac{(R_a - R_b)}{R_a} \quad (5-2)$$

Where R<sub>a</sub> is the resistance of the sensor in air, R<sub>b</sub> is the resistance of the sensor in the presence of H<sub>2</sub> gas. The sensitivity of the sensor as a function of injecting H<sub>2</sub> concentration is shown in Figure 5.6, indicating that the sensitivity of those four type nanowire sensors is increased with increasing both H<sub>2</sub> concentration and SnO<sub>2</sub> thickness. At the low H<sub>2</sub> concentration, the lower sensor response would be attributed to that it does not have enough amounts of H<sub>2</sub> molecules to react with the surface-adsorbed oxygen species. On the other hand, the increase in H<sub>2</sub> concentration leads to enhance the trapped electrons released and increase the sensitivity of the nanowires. Similar phenomenon has also been observed from ethanol sensors based on single crystalline SnO<sub>2</sub> nanorods <sup>[5.22]</sup>. Among the above mentioned four type nanowire sensors, the ZnO-SnO<sub>2</sub>-20 core-shell nanowire sensor shows the best sensitivities. They are 80, 83, 86 and 89% when concentrations of the injected H<sub>2</sub> gas are 25, 50, 100 and 200 ppm, respectively. Usually, the change in resistance, consequently, the sensitivity of sensor is attributed to the adsorption and desorption

oxygen ions forming a depletion region at the nanowires surface. Since our nanowires covered with average thickness of amorphous SnO<sub>2</sub> layer (ultrafine particle film) less than 9 nm, which is comparable to the space charge length, a large gas concentration dependence on resistance and significant enhancement of the sensitivity would be expected to be occurred<sup>[5,23]</sup>. In our case, as-grown ZnO nanowires exhibit an average diameter of 150 nm and length of 3.8 μm (large surface-to-volume ratio) and the thickness of SnO<sub>2</sub> shell layer between 2.5 to 9.0 nm changed with spin-coated times. It would cause the following two different extremes occur: when the device is exposed to the reducing gas, the depletion of carriers occurred at SnO<sub>2</sub> layer of the core-shell nanowires in air would produce a pinch-off channel (high resistance) and then the removal of adsorbed oxygen from the SnO<sub>2</sub> shell layer in H<sub>2</sub> reducing gas leads to produce a highly conductive channel (low resistance). Among our various core-shell nanowires, the ZnO-SnO<sub>2</sub>-20 exhibiting a thicker SnO<sub>2</sub> shell layer, 9.0 nm, produces a larger pinch-off channel than other core-shell nanowires and reveals a high resistance (R<sub>a</sub>) in air. In contrast, the core-shell nanowires with SnO<sub>2</sub> shell layer for thickness comparable to space charge length in H<sub>2</sub> gas exhibit quite close R<sub>b</sub> values (as shown in Figure 5.5 (b)-(d)). Therefore, the improved sensitivity is found for the core-shell nanowire sensors with thicker SnO<sub>2</sub> layer.

#### 5-4. Conclusions

In summary, we successfully fabricated ZnO-SnO<sub>2</sub> core-shell nanowires by two-step chemical growth. The ZnO-SnO<sub>2</sub> core-shell nanowires had a single crystal ZnO cores and amorphous SnO<sub>2</sub> shell layer. Through spin coating, the SnO<sub>2</sub> shell layer uniformly coated onto the ZnO nanowires and the various SnO<sub>2</sub> shell layer thickness were obtained by adjusting spin coating times. The H<sub>2</sub> gas sensors were fabricated by these core shell nanowires using silver layer as the electrode. High

sensitivity (80 %) at both low H<sub>2</sub> concentration (25 ppm) and low working temperature (250 °C) was obtained. The core shell nanowire sensor with good sensitivity has high potential in gas sensor application.



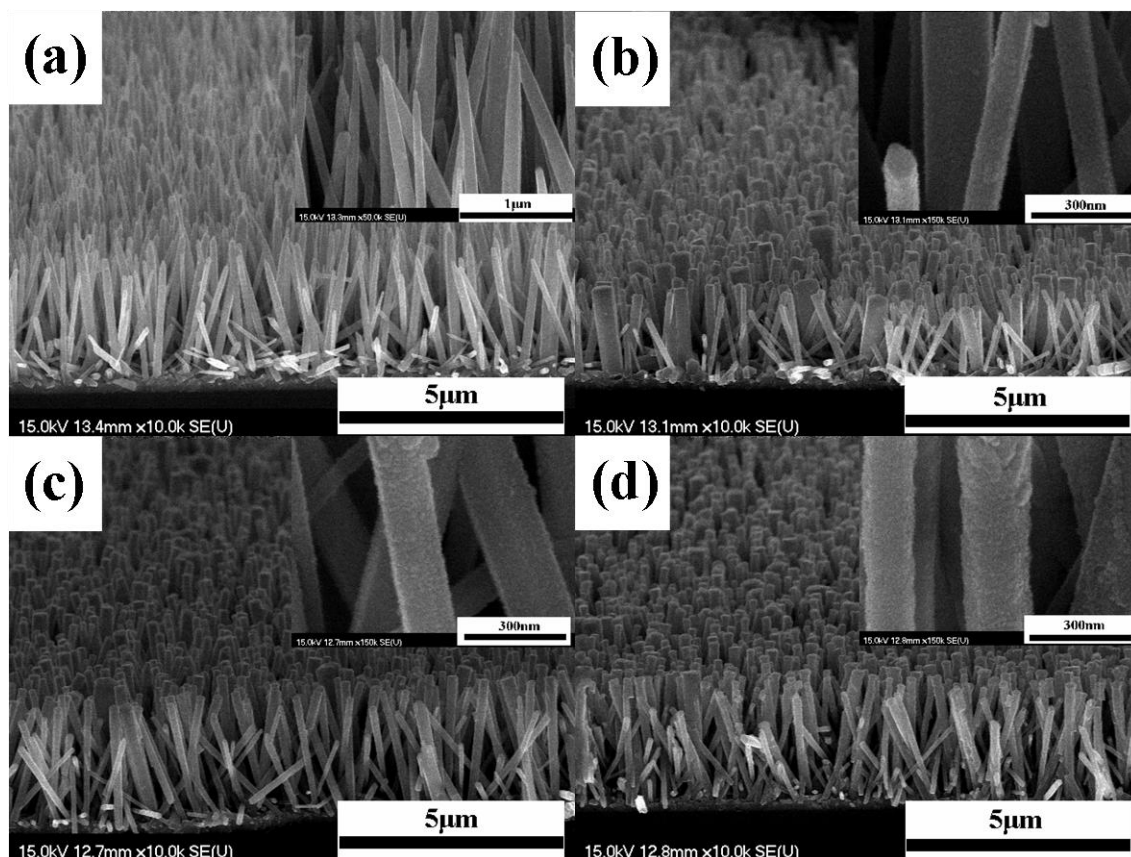


**Figure 5.1** Typical FE-SEM images of (a) as-grown ZnO nanowires, (b) ZnO-SnO<sub>2</sub>-5, (c) ZnO-SnO<sub>2</sub>-10 and (d) ZnO-SnO<sub>2</sub>-20 core-shell nanowires; (insets of (a), (b), (c) and (d): a side images of as-grown and core-shell nanowires.



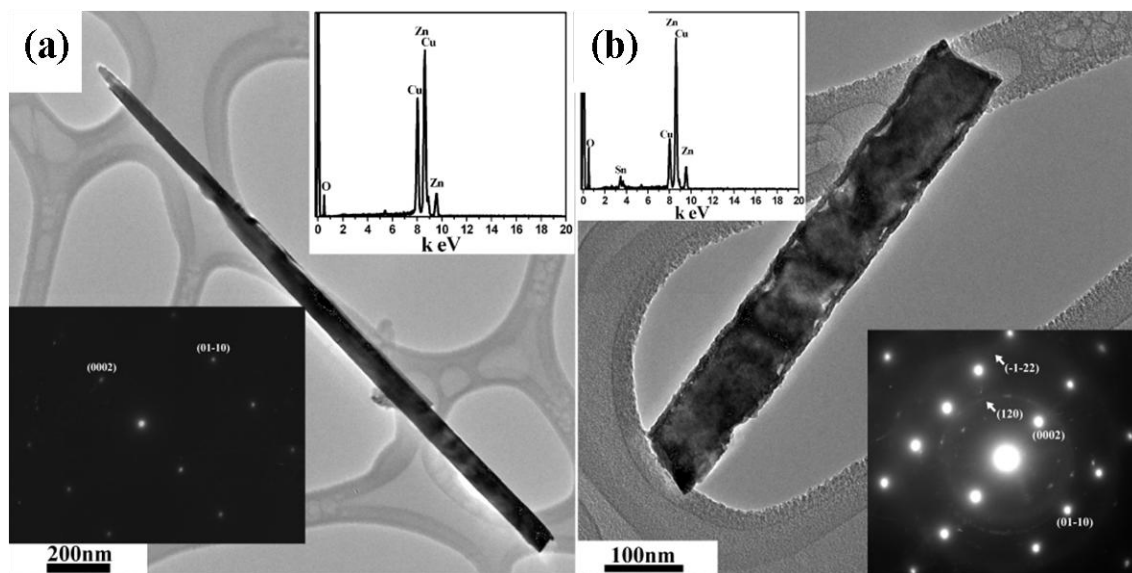


**Figure 5.2** TEM bright field image, EDS analysis and SAED pattern of the (a) as-grown ZnO nanowire and (b) ZnO-SnO<sub>2</sub>-20 core-shell nanowire.

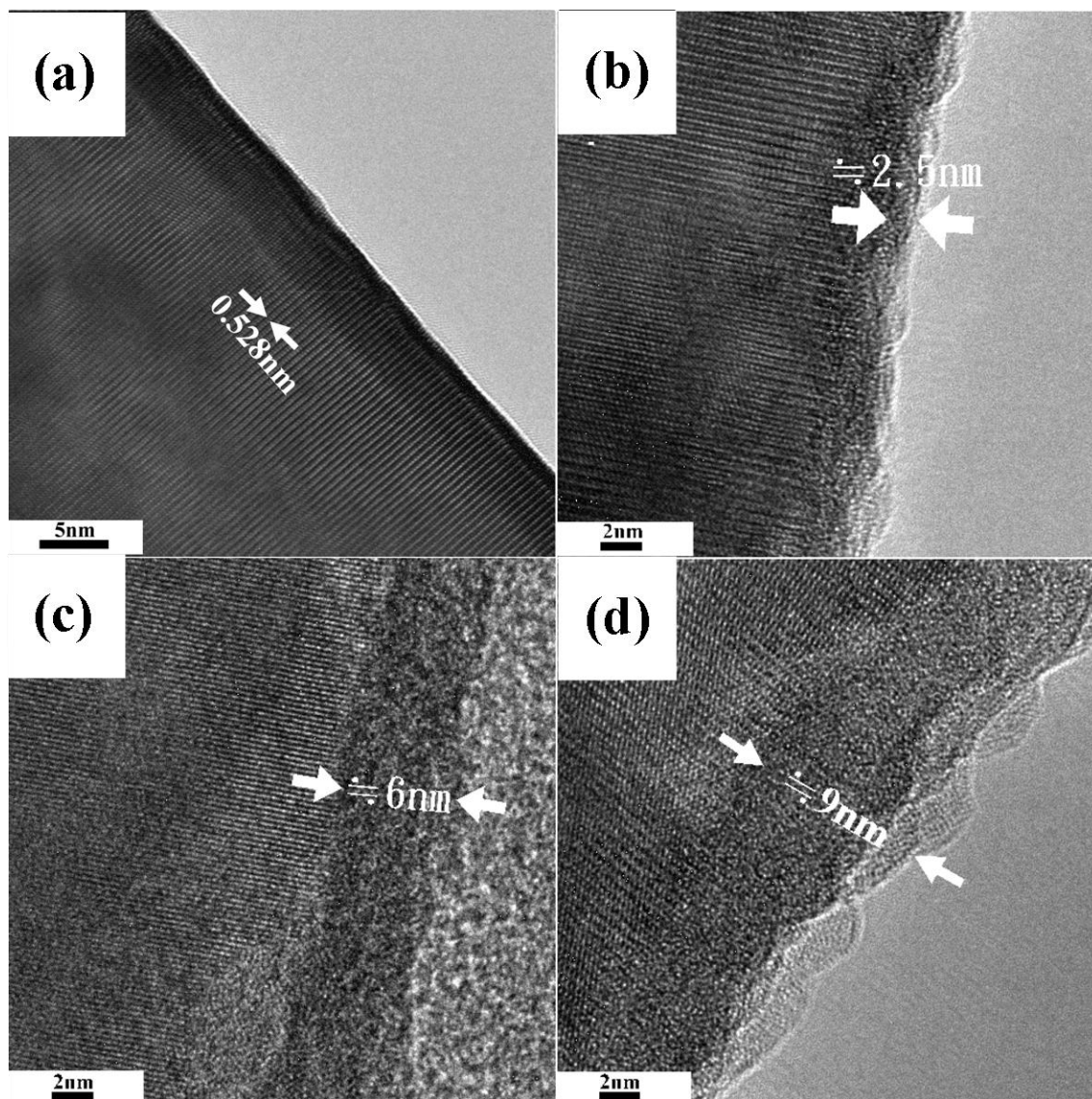


**Figure 5.3** HRTEM images of (a) As-grown ZnO nanowires, (b) ZnO-SnO<sub>2</sub>-5, (c) ZnO-SnO<sub>2</sub>-10 and (d) ZnO-SnO<sub>2</sub>-20 core-shell nanowires.

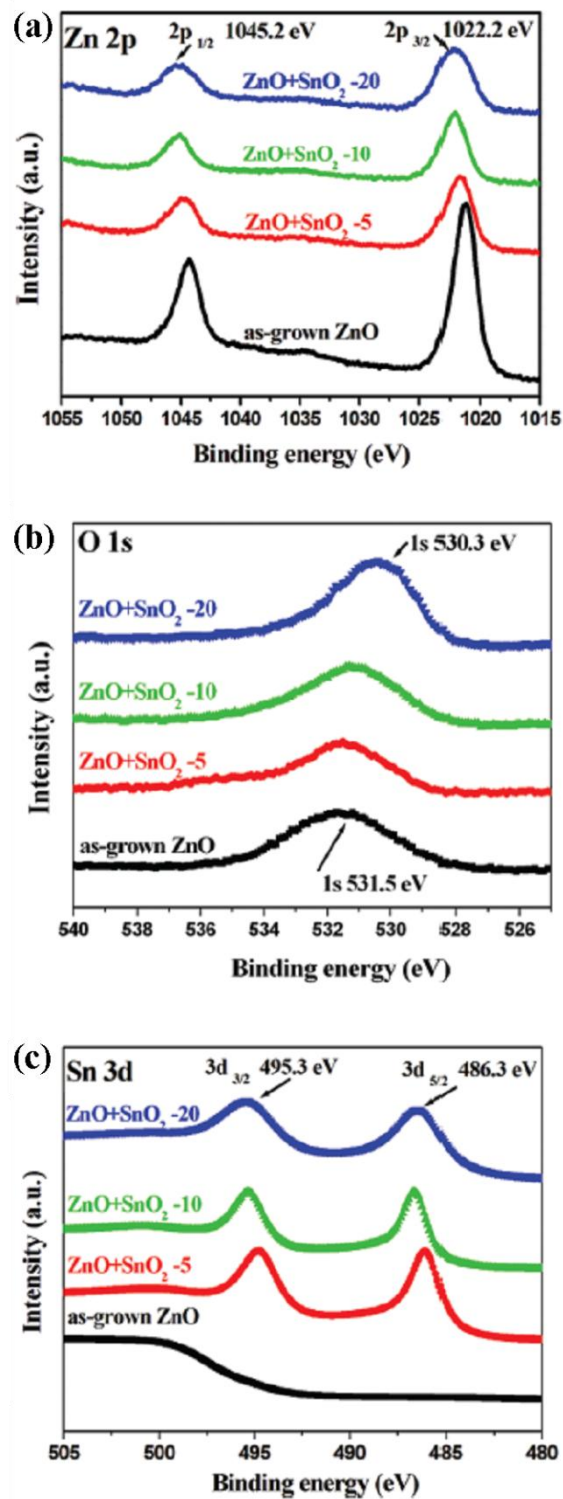


**Figure 5.4** XPS Spectra of as-grown ZnO and ZnO-SnO<sub>2</sub> core-shell nanowires, (a) Zn spectrum, (b) O spectrum and (c) Sn spectrum.

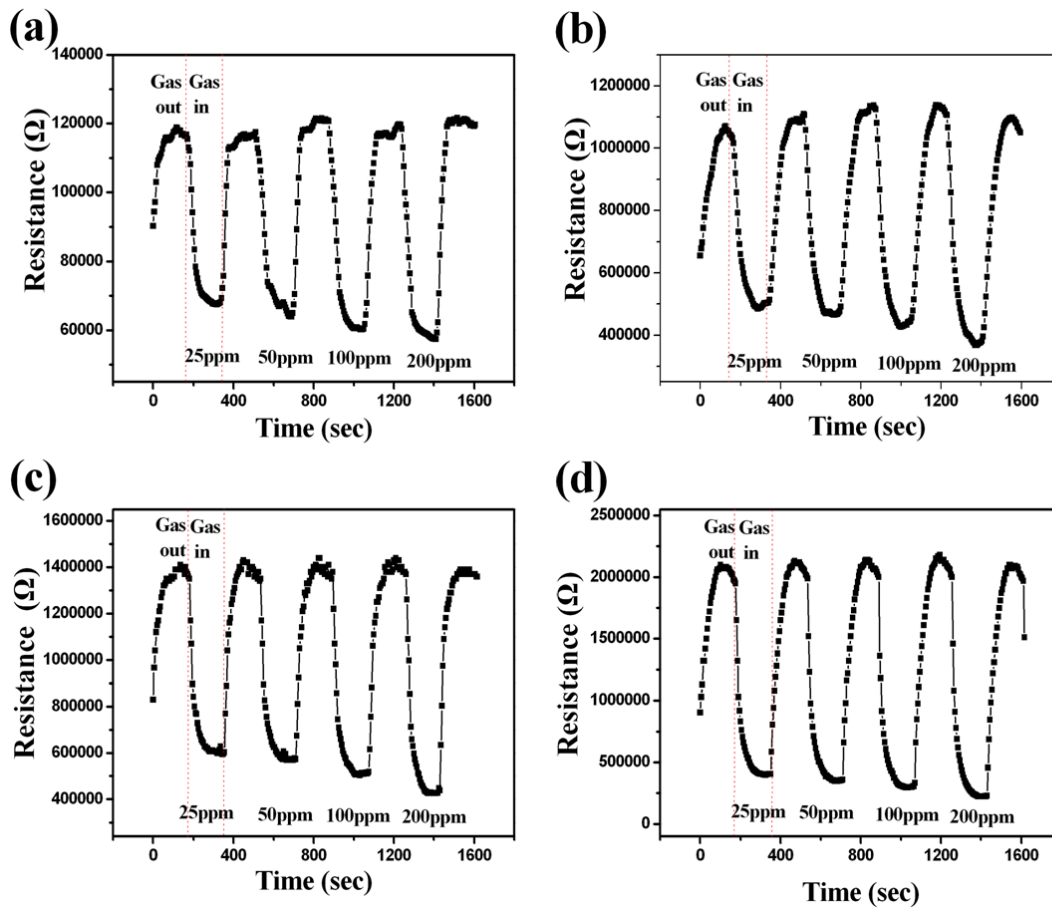


**Figure 5.5** Dynamic responses of (a) as-grown ZnO nanowires, (b) ZnO-SnO<sub>2</sub>-5, (c) ZnO-SnO<sub>2</sub>-10 and (d) ZnO-SnO<sub>2</sub>-20 core-shell nanowire sensors at 250 °C.

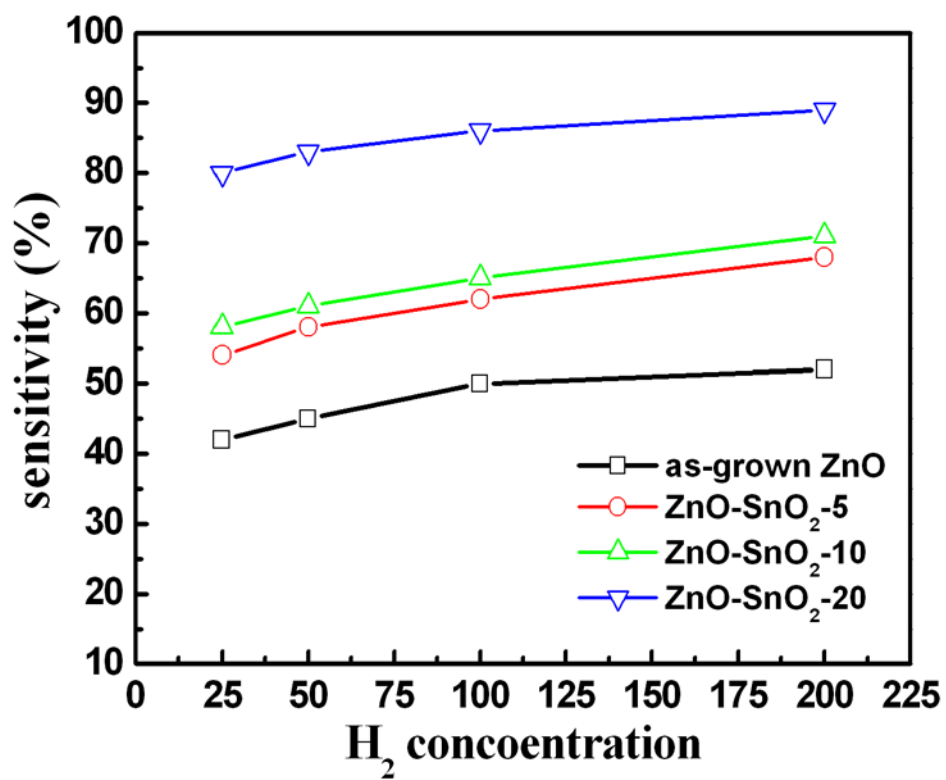


**Figure 5.6** Plots of sensitivity versus hydrogen concentration at 250 °C of the ZnO-SnO<sub>2</sub> core-shell nanowires.

# Chapter 6

## ZnO Nanorods Grown on Polymer Substrates as UV Photodetectors

### 6-1. Introduction

One-dimensional (1D) zinc oxide (ZnO) nanomaterials have recently received much attention for their potential applications in field emitter <sup>[6.1-6.2]</sup>, light emitting diode <sup>[6.3]</sup>, chemical sensor <sup>[6.4]</sup> and photodetector <sup>[6.5-6.8]</sup>. Among various applications, ultraviolet (UV) photodetector is an important device that has a wide range of chemical and environmental detecting applications. Compared with the bulk or thin film photodetectors, the 1D nanostructures are able to provide higher sensitivity and faster response devices because they have larger aspect ratio of length to diameter and much higher surface area to volume ratio compared with their film and bulk materials counter parts <sup>[6.9]</sup>. The photodetector with high sensitive properties was prepared by aligned ZnO nanorods on paper substrates using low temperature chemical solution <sup>[6.10]</sup>. The colloidal ZnO nanoparticles formed on glass substrates by spin-coating and were observed to have fast recovery time <sup>[6.11]</sup>. In addition, a simple wet chemical method combined with photolithography technique was used to prepare ZnO nanorods at selective areas, which exhibited a larger photoresponse than the thin film photosensors <sup>[6.12]</sup>. Obviously, the performances of the photodetectors were demonstrated to be improved through nanorod or nanoparticle form based on above mentioned previous results. Compared with Si, glass and paper substrates, the polyethylene terephthalate (PET) polymer substrates have the advantages of high transparency, good flexibility, and low cost <sup>[6.13]</sup>. Large area PET substrate is

commercially available, which is a good substrate for the fabrication of flexible photodetectors. However, the photoresponse properties of the nanorods grown on PET have received scarce attention. In this work, the vertically well-aligned ZnO nanorods are grown on ZnO buffer film/PET substrates using an aqueous solution method. The structure and morphology of ZnO nanorods and their UV photodetective properties are investigated.

## 6-2. Experimental method

The schematic description of the ZnO nanorod photodetector is shown in Figure 6.1. The fabrication of ZnO UV photodetectors is described as below. Before the ZnO nanorods are grown, a 10 nm-thick ZnO buffer layer is spin-coated onto PET substrate to reduce the mismatch between ZnO nanorods and polymer substrate. The two silver electrodes fabricated by E-gun evaporation with an area of 5 mm (W) × 15 mm (L) and thickness of about 48 nm are separated about 5 mm from each other. The silver electrodes have smooth surface based on the images of scanning electron microscope (not show here). Unless specified, the aqueous solution synthesis of ZnO nanorods is carried out at 90 °C in a sealed kettle placed in a quartz beaker. The ZnO coated substrates are immersed in a precursor solution for 60, 30, 20 and 10 min (ZnO-x, x=growth time), respectively, which is prepared by mixing 0.25 M zinc chloride (ZnCl<sub>2</sub>) with 7 ml ammonium hydroxide solution (NH<sub>4</sub>OH). After the reaction, the substrates are removed from the solution, rinsed with deionized water, and dried in the air. Surface morphologies and size distribution of the ZnO nanorods used in the photodetector fabrication are analyzed by field-emission scanning electron microscope (FE-SEM, Hitachi S-4700I). X-ray diffraction (XRD, Bede D1), photoluminescence (PL) and transmission electron microscope (TEM, JEOL 2100F) observations are then utilized to characterize the crystallographic and optical

properties of those ZnO nanorods. Both the current-voltage ( $I$ - $V$ ) characteristic and current-time ( $I$ - $t$ ) photoresponse are measured at room temperature in air under UV illumination at  $\lambda=365$  nm with power densities of 25, 35 and 70  $\mu\text{W}/\text{cm}^2$ , respectively.

### 6-3. Results and discussion

#### *6-3-1 Morphology, crystal structure, composition and optical properties of ZnO nanorod array*

Figures 6.2 (a)-(d) reveal the typical FE-SEM images of the ZnO nanorods synthesized for 60 and 10 min by the aqueous solution method. It can be observed the ZnO nanorods vertically well aligned grown on the ZnO film/PET substrate. The average length of ZnO nanorods decreases from  $1520 \pm 155.3$  to  $425 \pm 25.3$  nm and their average diameter decreases from  $120 \pm 22.3$  to  $30 \pm 5.5$  nm as the growth time decreased from 60 to 10 min. The ZnO nanorods with various growth times are uniformly grown on the ZnO film/PET substrate (Figures 6.2 (a)-(d)), indicating that the vertical nanorods with uniform length and diameter can be easily synthesized with the growth time of 10 min.

Figure 6.3 (a) indicates XRD patterns of ZnO nanorods with various growth times, exhibiting the single phase with wurtzite structure for all the nanorods. In addition, the intensity of (002) peak is much higher than those of other peaks, suggesting that the ZnO nanorods preferentially grow in the [001] direction. The intensity of (002) peak increases with an increase of the growth time, indicating that the crystallinity is improved by increasing growth time. Figure 6.3 (b) reveals the room temperature PL spectra of ZnO nanorods with a strong luminescence peak centered at around 377 nm, which represents the near-band-edge emission, while a weak broad band centered around at 550 nm is mainly attributed to oxygen vacancies



excited in the ZnO crystals <sup>[6.14-6.16]</sup>. In addition, it also clearly indicates the blue shift of the UV peak position (from 377 to 374 nm) with reduced growth time. A similar behavior was also observed in ZnO nanorods, which was explained that the decrease in the size of ZnO nanorods can induce the blueshift of the UV peak <sup>[6.17]</sup>. The inset of the Figure 6.3 (b) shows the  $I_{UV}/I_{VIS}$  ratio as a function of growth time, where  $I_{UV}$  is the intensity of UV emission peak and  $I_{VIS}$  the intensity of visible emission peak. The  $I_{UV}/I_{VIS}$  ratio slightly increase with an increase of growth time, which has the same trend with the crystallinity improved by the increasing growth time (Figure 6.3 (a)). The bright field image of the ZnO-10 nanorods is shown in Figure 6.4 (a), revealing that the nanorod exhibits the diameter of the nanorod tip is slightly smaller than that of the bottom. The HRTEM image (inset at upper right corner of Figure 6.4 (a)) indicates the nanorod is highly crystalline with a lattice spacing of 5.204 Å, which corresponds to the (002) plane in the ZnO crystal lattice. The selected area diffraction (SAED) pattern (inset at low left corner of Figure 6.4 (a)) identifies the ZnO nanorod crystal growth along the [001] direction, which was confirmed with the result from XRD (Figure 6.3 (a)). The typical EDS spectrum for ZnO-10 nanorods shown in Figure 6.4 (b) indicates that the nanorods are composed of only Zn and O. The Cu and C signals originate from the TEM grid. No evidence of other impurities was found from the spectrum. With further quantitative analysis of EDS, it reveals that the atomic ratio of Zn/O is 43.3:56.7.

### **6-3-2 UV sensing properties of ZnO nanorods**

Taking advantage of the highly mechanical flexibility of the ZnO nanorods/PET substrate, ZnO-10 nanorods could be extremely bent without losing their structural integrity, as shown in Figures 6.5 (a)-(c). Despite the bending radius of 5 mm, the structural integrity was well maintained at convex and concave geometries. Figure 6.5

(d) depicts the current-voltage curves of ZnO-10 nanorods/PET substrate at the bending measurement. It is observed the typical Ohmic behavior and the current of concave, flat and convex structures are 68.5, 63.2 and 61.3 nA at 0.5 V, respectively. The current variation between various structural geometries is negligible difference. It reveals good mechanical stability throughout the bending measurement.

Figure 6.6 (a) depicts I-V characteristics of the ZnO-10 nanorods photodetector measured in the dark environment and under illuminations by changing the DC bias from -5 to +5 V from bottom (the illumination underneath the polymer substrate) to top. During photocurrent measurement, the dark current is about 63.2 nA at a DC bias of 0.5 V. The small dark current is attributed to high resistance of the ZnO-10 nanorods. We are able to neglect the contact resistance between Ag and ZnO buffer layer and the resistance of the electrodes because the resistance of the Ag electrodes ( $16.29 \text{ n}\Omega \cdot \text{m}$  at  $18 \text{ }^\circ\text{C}$ ) is much lower than that of the ZnO-10 nanorods <sup>[6.18]</sup>. With the same DC bias of 0.5 V, the measured currents are 0.66, 0.92 and  $1.55 \text{ }\mu\text{A}$  under 25, 35 and  $70 \text{ }\mu\text{W}/\text{cm}^2$  UV light, respectively. The currents under 25, 35 and  $70 \text{ }\mu\text{W}/\text{cm}^2$  UV illuminations are about 11, 15 and 25 times higher than the dark current at 0.5 V, respectively. The low dark current is caused by the depletion layer formed near the surface by adsorbed oxygen molecules in the dark environment  $[\text{O}_{2(\text{g})} + \text{e}^- \rightarrow \text{O}_{2(\text{ad})}^-]$ . When the ZnO nanorods are exposed under UV illumination, they generate electron-hole pair  $[\text{h}\nu \rightarrow \text{e}^- + \text{h}^+]$ . The trapped electrons are released back to the conduction band when the photo-generated holes reacted with the adsorbed oxygen molecules  $[\text{h}^+ + \text{O}_{2(\text{ad})}^- \rightarrow \text{O}_{2(\text{g})}]$ , to increase the carrier concentration of the ZnO nanorods <sup>[6.19-6.21]</sup>. Consequently, the current under UV illumination is higher than that in the dark environment.

Figure 6.6 (b) shows the time-resolved photocurrent of the ZnO-10 nanorods photodetector in response to turn-on and turn-off the UV illumination with power

densities of 25, 35 and 70  $\mu\text{W}/\text{cm}^2$ , respectively. The photocurrent exponentially increases from 29.2 nA to 1.55  $\mu\text{A}$  within about 100 sec and then gradually saturates when in turn on state with a power density of 70  $\mu\text{W}/\text{cm}^2$ . After the UV light was turned-off, the current decreases to 63.2 nA within 120 sec. Five cycles of photocurrent switching with various power densities clearly demonstrate the response reproducibility of the ZnO-10 nanorods.

The sensitivity of the UV nanorod photodetector is defined as  $I_{\text{UV}}/I_{\text{Dark}}$ , where  $I_{\text{UV}}$  is the current of the nanorods in UV turn-on state and  $I_{\text{Dark}}$  the current of the nanorods in the UV turn-off state. The sensitivity versus time curves under 100 sec illumination of the photodetectors are shown in Figure 6.6 (c), revealing the times of the current recovering to initial value of the ZnO-10, ZnO-20, ZnO-30 and ZnO-60 photodetector are 120, 210, 290 and 470 sec, respectively. The ZnO-10 photodetector has faster recovery rate in comparison with other photodetectors. The possible reason is attributed to that the ZnO-10 nanorods have relatively shorter electron transmission length compared to other larger radius nanorods [6.11, 6.22]. Thus, the photodetector made by the small radius and short ZnO nanorods exhibits shorter recovery time. Figure 6.6 (d) shows the sensitivity under 100 sec illumination of the ZnO-based photodetector as a function of growth time, indicating that the sensitivity of ZnO-based photodetector increases with an increase of UV light power density and a decrease of growth time. However, under longer time illumination (over 150 sec), the longer nanorod (ZnO-60) photodetector exhibits higher sensitivity under 25  $\mu\text{W}/\text{cm}^2$  UV density (Figure 6.6 (e)) because ZnO-60 provides larger surface area.

To further evaluate the photodetector performance of the ZnO-10/ PET structure, the orientation, retention, stability and multi-UV intensity characteristics are measured and demonstrated. As shown in Figure 6.7 (a), the photoresponses are kept the same and without any observable degradation between the measurements of

bottom to top and top to bottom UV light illuminations. Figures 6.7 (b)-(c) depict the retention and stability characteristics of ZnO-10 photodetector, indicating that the photoresponse can be successively and stably operated than 100 h (Figure 6.7 (b)) and the photoresponse at power density of  $25 \mu\text{W}/\text{cm}^2$  is over 20 cycles, which is more stable and reconstructive in comparison with other higher power densities during the cycling measurement. As shown in Figure 6.7 (d), the various UV intensities with 25, 35 and  $70 \mu\text{W}/\text{cm}^2$  are applied to switch the ZnO-10 photodetector into various current states, where the UV illumination is from bottom to top. The cycle width used for all measurements is 220 sec and the cycle number is 10. Therefore, at least four-level current states can be determined here by controlling the UV power density, which is easily implemented in today's sensor design. Based on the results from Figures 6.7 (a)-(d), the ZnO-10/PET photodetector has good performance of nondestructive photoresponse, high reliability and multilevel photoresponse under either the illumination at the single UV or different UV power density. Table (1) summarizes and compares the performance of various ZnO photodetectors. It indicates that our ZnO-10/PET photodetector has faster response and recovery rate under various UV intensity illuminations, higher reliability, excellent orientation properties, multi-level photoresponse in comparison with other reported photodetectors.

#### **6-4. Conclusions**

In this work, we successfully develop a simple method to fabricate high performance ZnO UV photodetector on the flexible PET substrate. Through aqueous solution method, the ZnO nanorods uniformly grow on the PET substrate and the various ZnO nanorods lengths are obtained by adjusting growth time. The ZnO-10/PET structure reveals good mechanical stability through bending test. Upon

UV illumination, the ZnO-10 nanorods photodetector exhibits high sensitivity at low UV power density ( $25 \mu\text{W}/\text{cm}^2$ ), fast recovery time (120 sec), good orientation properties, reproducible photoresponse (20 cycles) and multi-level photoresponse. The ZnO-10/PET photodetector made by a simple process has high potential for practical applications.



**Table 6.1** Comparison of photodetector characteristic for various ZnO nanostructures.

Type of ZnO nanostructures	Substrate	Test UV intensity ( $\mu\text{W}/\text{cm}^2$ )	Response Time (s)	Recovery Time (s)	Reliability	Ref.
Nanoparticles (in $\text{O}_2$ )	Silicon	20	$\approx 10$	$\approx 50$	4 cycles of switching	[6.23]
Nanotubes	Glass	–	$\approx 130$	$\approx 250$	4 cycles of switching	[6.24]
Single-microtube (in $\text{O}_2$ )	–	21700 at 50 cm distance	$\approx 15$	$\approx 1850$	4 cycles of switching	[6.25]
Nanowires	Glass	1000	40	55	–	[6.26]
Nanorods	Paper	–	$\approx 800$	$\approx 600$	5 cycles of switching	[6.10]
Nanorods	Glass	300	$\approx 300$	$\approx 500$	4 cycles of switching	[6.27]
Nanorods	Silicon	16	$\approx 100$	$\approx 150$	12 cycles of switching	[6.28]
In our work (ZnO-10/PET)	PET	25 35 70	100	120	20 cycles of switching Two-fold symmetry characteristic Retention test (1,50 and 100 h) Multilevel photoresponse	

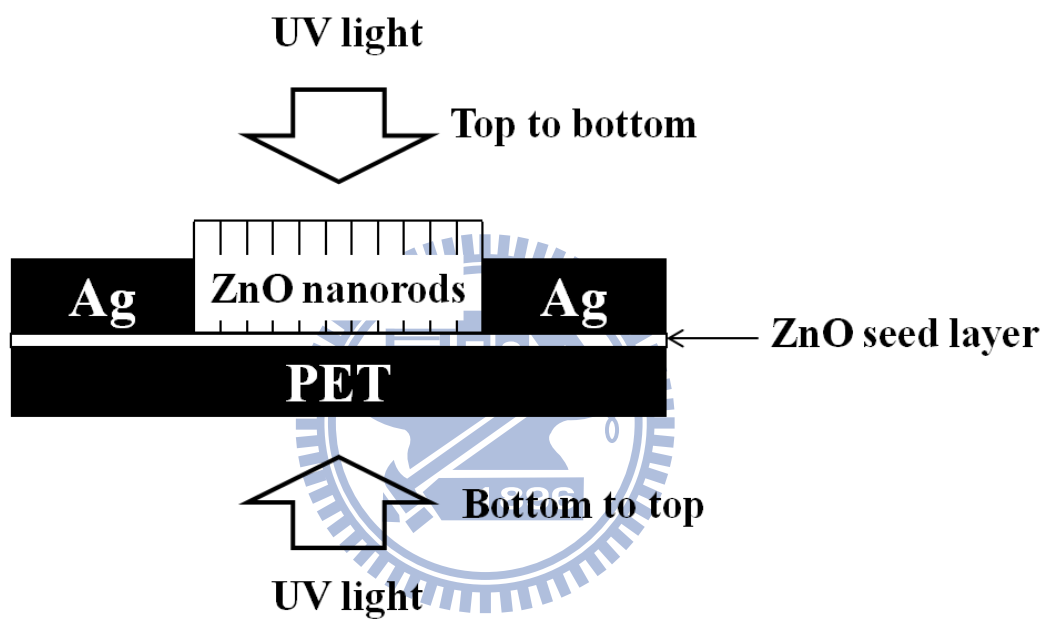


**Figure 6.1** Schematic structure of ZnO nanorod photodetector.

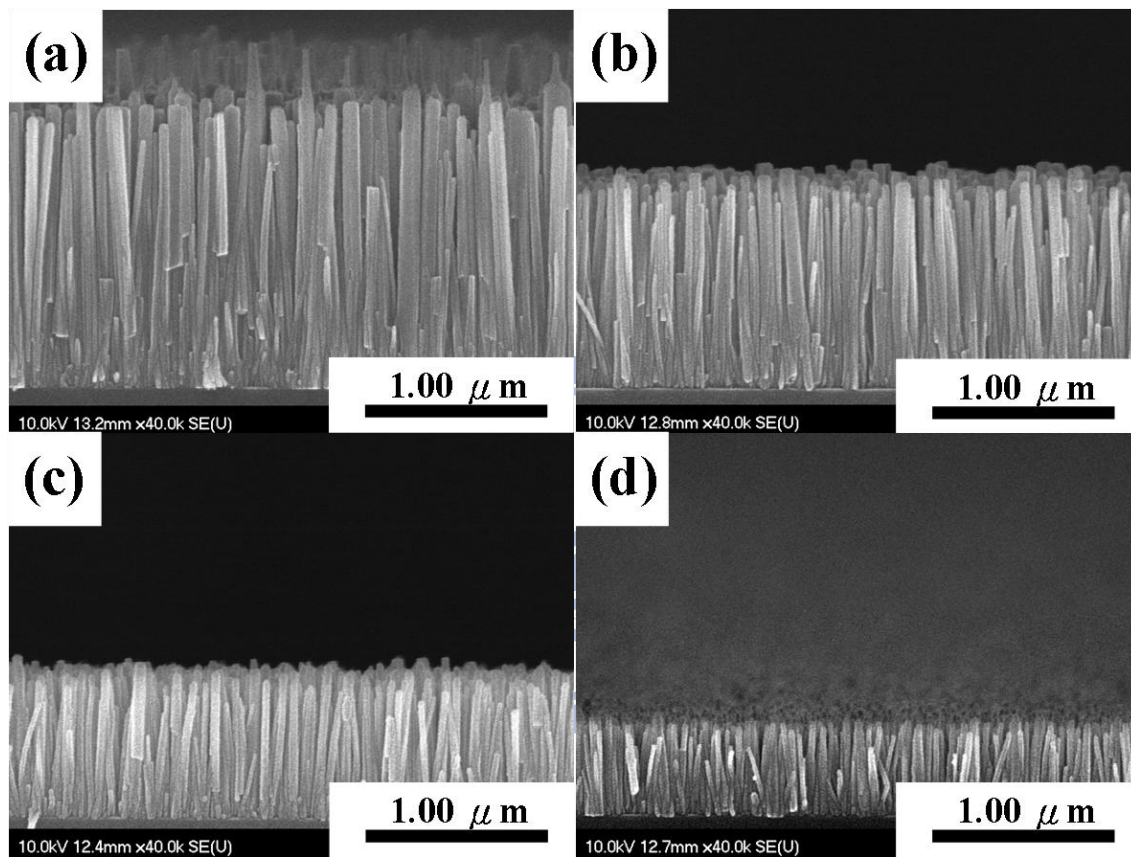


**Figure 6.2** Typical FE-SEM images of (a) ZnO-60, (b) ZnO-30, (b) ZnO-20 and (d) ZnO-10 nanorods, respectively.



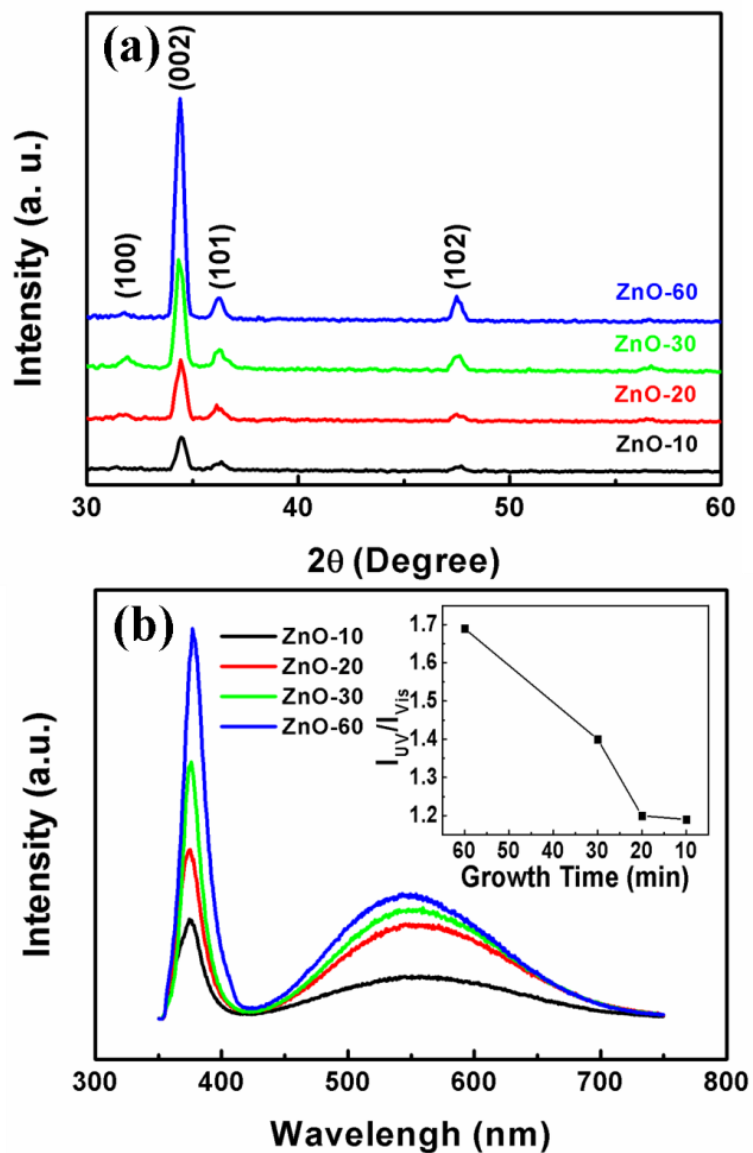


**Figure 6.3** (a) XRD patterns and (b) PL spectra of the ZnO nanorods with various growth times. Inset is the ratios of UV emission to visible light emission as a function of growth time.

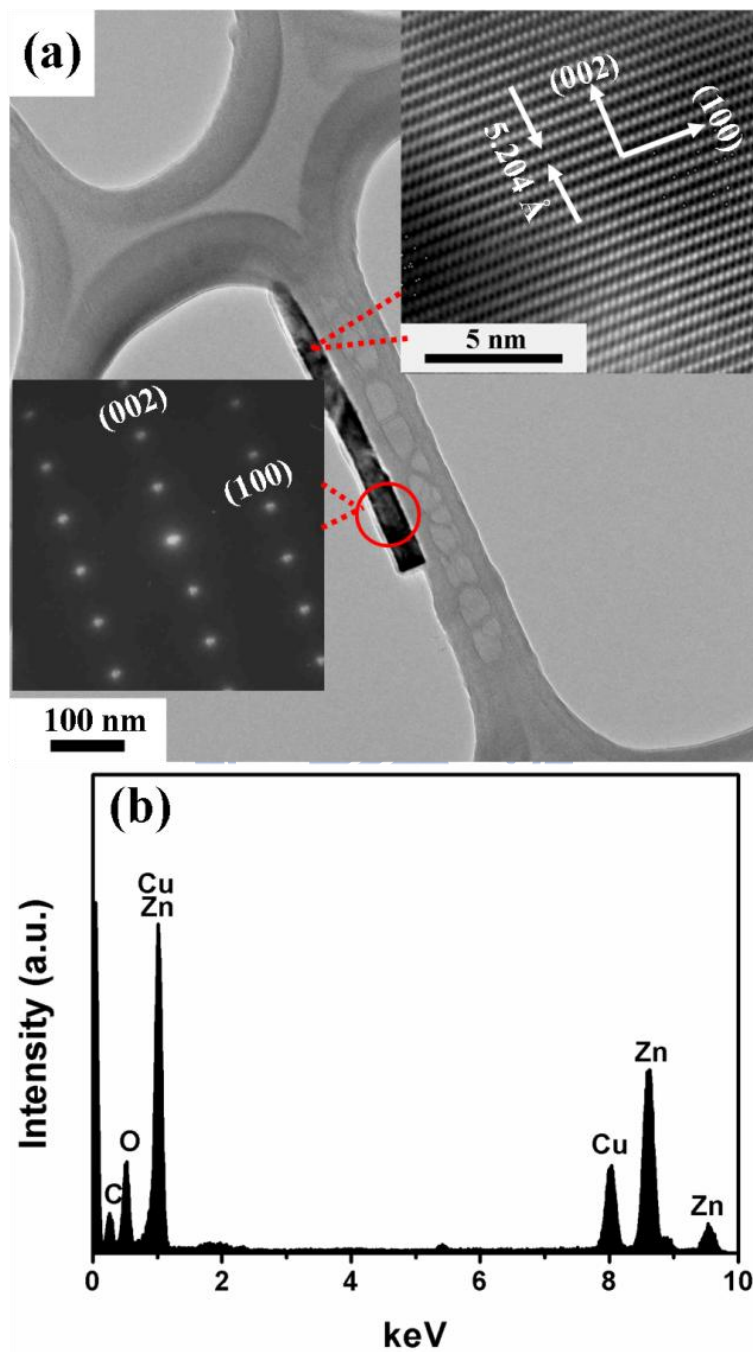


**Figure 6.4** (a) TEM bright image and (b) EDS analysis of the ZnO-10 nanorod. Inset is the SAED pattern and HRTEM image of the ZnO-10 nanorod.

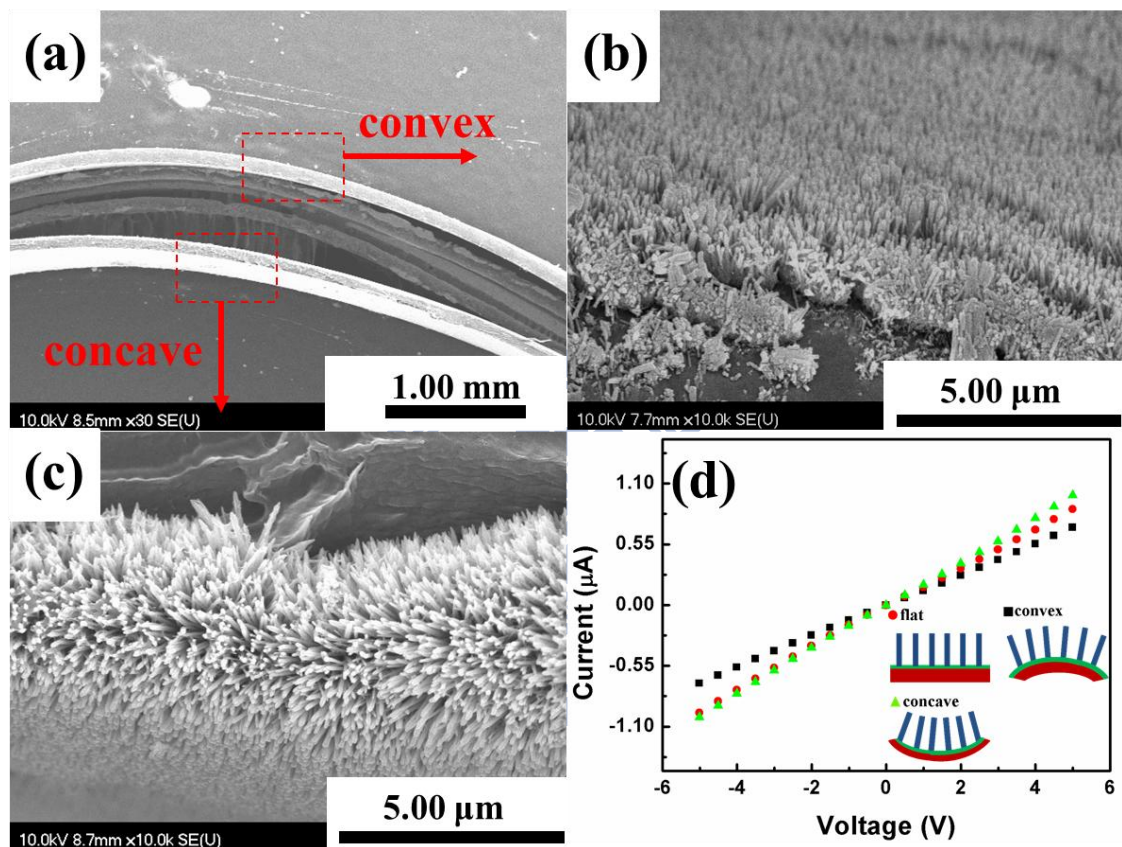


**Figure 6.5** (a) Low magnification SEM image of high bent ZnO-10/PET structure (b) convex and (c) concave geometric side views and (d) I-V characteristics measured at different bending morphologies.

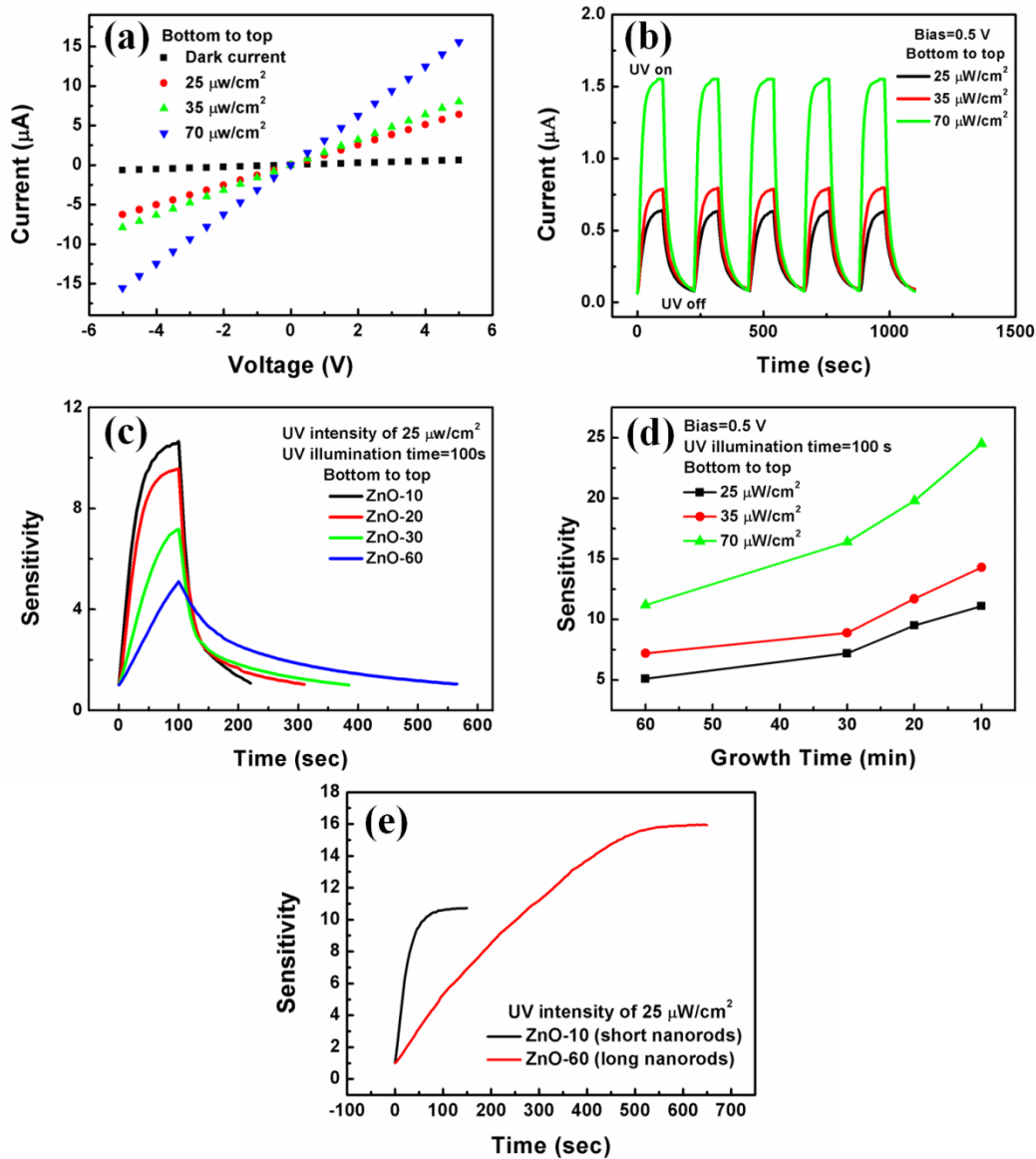


**Figure 6.6** UV photodetective properties (a) I-V plot of ZnO-10 nanorods in the dark environment and under UV illumination (365 nm) with power densities of 25, 35 and 70  $\mu\text{W}/\text{cm}^2$ , respectively. (b) Reversible switching properties of ZnO-10 nanorods. (c) Sensitivity vs time plots under 100 sec illuminations of ZnO nanorods grown with various times at power density of 25  $\mu\text{W}/\text{cm}^2$ . (d) Sensitivity vs growth time curves of the nanorods at 0.5 V bias under 100 sec illuminations. (e) Sensitivity vs time plots of longer (ZnO-60) and shorter (ZnO-10) nanorod photodetectors under longer time illumination.

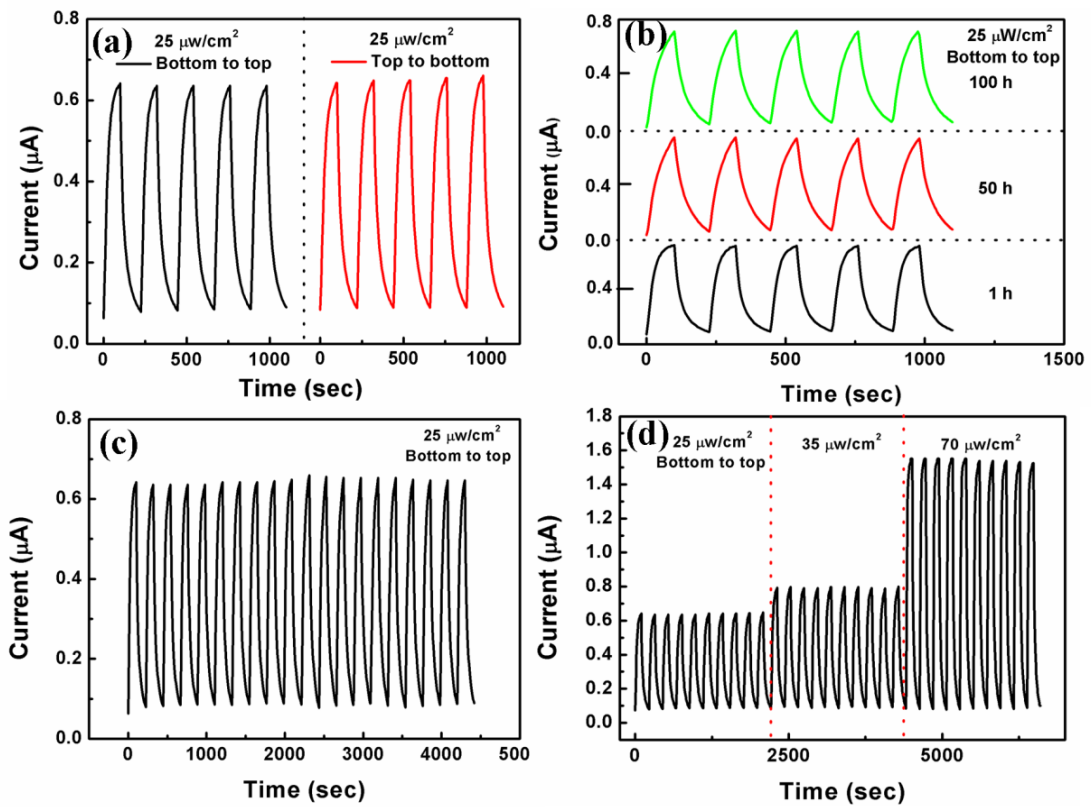


**Figure 6.7** Stability measurements of ZnO-10/ PET photodetector: (a) different orientation UV illumination (b) retention properties, (c) stability characteristics at UV power density of  $25 \mu\text{W}/\text{cm}^2$  and (d) Multilevel photoresponse performed by various UV power density illuminations.

# Chapter 7

## Fabrication and Resistive Switching Characteristics of High Compact Ga-doped ZnO nanorod Thin Film Devices

### 7-1. Introduction

Next-generation nonvolatile memory (NVM) has attracted increasing attention as conventional charge-storage-based flash memories approach their scaling limits. To overcome this significant issue, researchers have examined various emerging NVMs, including ferroelectric random access memory, phase-change random access memory, magnetic random access memory and resistance random access memory (RRAM), as replacements for flash memory. Previous studies have indicated that RRAM is a promising candidate because of its simple structure, high operation speed, and high density integration. Researchers have proposed a number of metal oxides, including  $\text{ZrO}_2$ <sup>[7.1-7.5]</sup>,  $\text{TiO}_2$ <sup>[7.6-7.8]</sup>,  $\text{Pr}_{1-x}\text{Ca}_x\text{MnO}_3$ <sup>[7.9]</sup>,  $\text{SrZrO}_3$ <sup>[7.10-7.11]</sup>,  $\text{ZnO}$ <sup>[7.12-7.13]</sup> and  $\text{NiO}$ <sup>[7.14]</sup> for RRAM applications because of their excellent characteristics. Among these, ZnO-based film is one of the most attractive materials for RRAM applications because of its high transparency, reliability, and stable resistive switching (RS) behavior of the metal-insulator-metal (MIM) structure<sup>[7.12-7.13]</sup>. Chang et al. prepared RS devices by aligning ZnO nanorods on an ITO substrate using a low-temperature chemical solution method<sup>[7.15]</sup>. Yang et al. fabricated a single Sb-doped ZnO nanobelt/SiOx/p-Si device exhibiting RS behavior, as measured by atomic force microscopy (AFM)<sup>[7.16]</sup>. Compared with thin-film RS devices, a 1D nanostructure can provide a localized conducting filament in devices that allow RS operation with a narrow dispersion of operation parameters. However, direct contact between the top and bottom electrodes may cause a short circuit problem if the top electrode is

fabricated on ZnO nanorod resistive switching film with a low packing density. A hybrid RS device consisting of ZnO nanorods embedded in insulating polymethylmethacrylate (PMMA) polymer can avoid such direct contact [7.17]. However, embedding ZnO nanorods in PMMA is a complex and time consuming process. Preparing high-density and high-compact ZnO nanorod thin films without an additional polymer-embedded process is highly advantageous for RS devices.

This study develops a simple process of forming continuous and extremely dense Ga-doped ZnO (GZO) nanorod thin films with a highly preferred orientation on Au/Ti/SiO<sub>2</sub>/p-Si substrates from a low temperature aqueous solution. This study also investigates the RS behavior and conduction mechanisms of nanorod thin films without any embedding. Results demonstrate that the films exhibit excellent bipolar RS behavior, including low operation voltage and good endurance property.

## 7-2. Experimental details

Figure 7.1 shows a schematic view of the GZO nanorod array-based memory device. A  $79.30 \pm 1.54$  nm thick ZnO buffer layer was first deposited on Au/Ti/SiO<sub>2</sub>/Si substrate by radio-frequency (RF) magnetron sputtering. The aqueous solution synthesis of GZO nanorods was subsequently conducted at 90 °C in a sealed kettle placed in a quartz beaker. The ZnO-coated substrates were immersed in precursor solutions of zinc chloride (0.025 M), ammonium hydroxide solution (25%), and gallium chloride (Ga/Zn molar ratios: 0, 6, 8 and 10 %) for 10 min. The chemical composition of the GZO nanorods and the pH value in the deposition solution were controlled by adjusting the Ga/Zn molar ratio (Table 7.1). After the formation reaction, the substrates were removed from the solution, thoroughly rinsed with deionized water, and dried in air. To achieve MIM structure, 80 nm thick Au top electrodes with diameters of 150, 250 and 350  $\mu\text{m}$  were deposited by electron beam evaporation using



a shadow mask. The morphology, size distribution, and crystal structure of the GZO nanorods were examined by field-emission scanning electron microscopy (FE-SEM, Hitachi S-4700I), transmission electron microscope (TEM, JEOL 2100F) and X-ray diffractor (XRD, Bede D1), respectively. The TEM specimen was prepared by a focused ion beam (FIB, FEI Nova 200). To prove the chemical composition, a line-scan mapping was executed by an energy dispersive X-ray spectrometer (EDS, Oxford ISIS300). Photoluminescence (PL) spectroscopy was employed at room temperature using a 325 nm He-Cd laser for the optical characterization of the GZO nanorod thin films with various Ga/Zn molar ratios. The current-voltage (I-V) characteristics of all GZO devices were measured by an Agilent 4155C semiconductor parameter analyzer at room temperature.

## 7-3. Results and discussion

### 7-3-1 Morphology and crystalline structure

Figures 7.2 (a)-(d) show the typical FE-SEM images of GZO nanorod thin films with various Ga/Zn molar ratios synthesized for 10 min using the solution method. The vertically well-aligned nanorods were grown on the Au/Ti/SiO<sub>2</sub>/Si substrate and the diameter of the nanorods increased from 50.9±19.4 to 101.5±26.4 nm as the Ga/Zn molar ratio increased from 0 to 10 % in the deposition solutions (insets in Figures 7.2 (a)-(d), respectively). The thickness of nanorod films was approximately 220 nm. Low packing density nanorod film was formed on the substrate in the solution without Ga doping (Device 1), whereas increasingly dense nanorod array films were formed on the substrates in deposition solutions with Ga/Zn molar ratios increasing from 6 to 10% (Devices 2, 3, and 4, respectively). These different morphologies may arise from different nucleation and growth processes, because of different interfacial energies between ZnO buffer layer and different composition



GZO nanorods<sup>[7,18]</sup>. The direct contact between top and bottom electrodes occurred in the highly porous nanorod film without Ga (Device 1; Figure 7.2 (a)), leading to the short circuit problem. The RS behavior was not observed in this device according to DC voltage sweeping (I-V) measurement.

Figure 7.3 (a) shows the XRD patterns of GZO nanorod thin films with various Ga/Zn molar ratios, indicating that all the nanorod thin films exhibit a single phase with a wurtzite structure and have (002) highly preferred orientation (space group P63mc; JCPDS card NO. 36-1451). These XRD patterns show no peak corresponding to gallium or gallium oxide. The peaks marked with Au (002), (111) and (220) belong to the Au electrode. The XRD pattern of the nanorod film without Ga doping has a higher intensity (002) peak than other nanorod films, indicating that such a nanorod has better crystallinity than Ga-doping nanorods. The lattice constants of GZO (molar ratio=0, 6, 8, and 10 % in deposition solution) nanorods are  $a=b\sim 3.256 \text{ \AA}$ ,  $c\sim 5.204 \text{ \AA}$ ;  $a=b\sim 3.255 \text{ \AA}$ ,  $c\sim 5.198 \text{ \AA}$ ;  $a=b\sim 3.252 \text{ \AA}$ ,  $c\sim 5.194 \text{ \AA}$  and  $a=b\sim 3.252 \text{ \AA}$ ,  $c\sim 5.191 \text{ \AA}$ , respectively (Figure 7.3 (b)). These values can be calculated according to the XRD patterns. As the Ga/Zn molar ratio increased from 0 to 10 % in the solutions, the c-lattice parameter decreased from 5.204 to 5.191  $\text{\AA}$  because of the difference in ionic radii between  $\text{Ga}^{3+}$  (0.62  $\text{\AA}$ ) and  $\text{Zn}^{2+}$  (0.74  $\text{\AA}$ ). The lattice parameters decreased linearly as the gallium concentration in the nanorods increased, indicating that the gallium element was successfully doped into the ZnO lattice based on Vegard's law.

Figure 7.4 (a) shows the cross-section bright-field TEM images of Device 4, showing that the high density GZO nanorod thin film shows no evidence of cracks and holes. The nanorods only compose of Zn, O, and Ga peaks in the EDS spectra of the thin film (inset in Figure 7.4 (a)) and the real Ga/Zn molar ratio of this film is estimated to be  $9.00\pm 0.31 \%$  (Table 7.1). The Cu signal originates from the TEM grid. The corresponding elemental line-scan mapping of the device in Figure 7.4 (b) shows

that this compact GZO nanorod film does not contain a Au signature. Thus, there is no direct contact between the top and bottom electrodes in the devices, making it suitable for further RS memory studies.

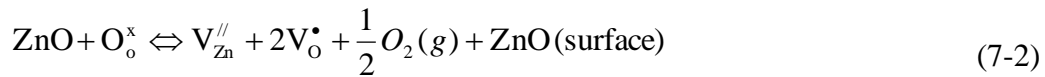
Figure 7.5 presents the room temperature PL spectra of Devices 1, 2, 3 and 4, respectively. This figure shows a strong luminescence peak centered at around 374 nm for all devices, indicating near-band-edge emission. A broader emission band is located in the green emission of the visible spectrum with an emission peak of about 550 nm, which can be attributed to deep level defects (oxygen vacancy and zinc interstitial) in the ZnO crystals [7.19-7.20]. The decrease of green emission peak intensity clearly indicates that the oxygen vacancy concentration decreases with an increasing of Ga/Zn molar ratio in solutions. The inset of Figure 7.5 shows the  $I_{UV}/I_{vis}$  ratio changed with device number, where  $I_{UV}$  and  $I_{vis}$  are the intensity of the UV and visible emission peak, respectively. The  $I_{UV}/I_{vis}$  ratio decreases slightly as the Ga/Zn molar ratio increases, which have the same trend with the XRD results (Figure 7.3 (a)). It is obviously indicated that the ZnO nanorod has better crystallinity than Ga-doping nanorods.

### **7-3-2 Resistive switching properties**

Figure 7.6 (a) indicates that the voltage is swept to a negative voltage above a certain value ( $V_{ON}$ ), and the GZO memory devices change from the OFF state to the ON state. A compliance current of 15 mA is applied to prevent the permanent breakdown of the device. Sweeping the positive voltage over the particular value ( $V_{OFF}$ ) creates abrupt decrease in the current as the device switches from the ON state to the OFF state. The memory devices show successful bipolar RS behaviors from both sides (ON-, OFF+ and ON+, OFF-) as shown in Figure 7.6 (a) and (b) and no unipolar RS properties are observed during the unipolar measurement process. The

device yield shown in Figure 7.6 (c) indicates that the devices with compact GZO nanorod thin films (Devices 3 and 4) achieve higher device yield than the device with porous GZO nanorod thin films (Device 2). Obviously, the devices made by using continuous and highly dense GZO nanorod thin films with a highly preferred orientation without any embedded process show an improved device yield.

Researchers have proposed various RS mechanisms to explain RS behavior. Among the proposed models, the conducting filament formation/rupture had been employed to successfully explain the bipolar RS behavior. Figure 7.7 (a) plots the dependences of the resistance value of ON and OFF states on pattern size. The  $R_{ON}$  and  $R_{OFF}$  seem to be insensitive to the pattern size. Therefore, the formation/rupture of localized conducting filaments is the preferred switching mechanism of the Au/GZO nanorod thin films/ZnO/Au devices. According to the filamentary model<sup>[7.21-7.22]</sup>, the localized conducting filaments consist of defects such as oxygen vacancies between the top and bottom electrodes, leading to transition from the OFF state to the ON state. The similarity in ionic radii between  $Ga^{3+}$  (0.62 Å) and  $Zn^{2+}$  (0.74 Å) suggests that the gallium ion can substitute for the zinc ion. The possible defect equations of this substitution can be expressed as the following:



where  $Ga_{Zn}^{\bullet}$  denotes the gallium ion with a single positive charge in the zinc

site, the  $V_o^\bullet$  and  $V_o^{\bullet\bullet}$  are the oxygen vacancies with single and double positive charges, respectively,  $O_o^x$  indicates the neutral oxygen ion in the lattice site,  $V_{Zn}^{//}$  is the zinc vacancy with the double negative charge, and  $e'$  denotes the electron with a single negative charge for compensation. According to equation (7-1), incorporating gallium into the ZnO nanorods generates ionic defects ( $V_{Zn}^{//}$ ) associated with a  $Zn^{2+}$  site substituted by a  $Ga^{3+}$  ion. Furthermore, the generated defects change the equilibrium of the system. Based on equations (7-2)-(7-5), and Le Chatelier principle [7.23], the system tends to shift in the direction that reduces the change in conditions (i.e., the reactions shift toward the left-hand side as oxygen vacancies are reduced). As a result, both  $V_{Zn}^{//}$  and  $e'$  suppress the formation of oxygen vacancies as the Ga/Zn molar ratios in the nanorods increase. This shows the same trend as the results of PL studies. The mobility of defects at the surface of the film is substantially higher than that in the single crystal material (Figure 7.7 (b)) [7.14], which suggest that  $V_o^{\bullet\bullet}$  or  $V_o^\bullet$  can easily assemble to form conducting filaments at the surface of the single crystalline GZO nanorod. By applying negative voltage for the devices, many positive ionic defects of  $V_o^{\bullet\bullet}$  or  $V_o^\bullet$  are expected to assemble and form conducting filaments at the interface between GZO nanorods (grain boundary). The injected electrons are simultaneously transported from the top to the bottom electrode and the device switches from the OFF state to the ON state (Figure 7.7 (c)). Applying a positive voltage on the top electrode to  $V_{OFF}$  releases the positive ionic defects of  $V_o^{\bullet\bullet}$  or  $V_o^\bullet$  in the weakest region (between GZO nanorod interface and ZnO seed layer), and the conducting filament ruptures at the interface. These results in switching to the OFF state (Figure 7.7 (d)). Applying a negative voltage to  $V_{ON}$  causes  $V_o^{\bullet\bullet}$  or  $V_o^\bullet$  to

re-assemble, forming conducting filaments and switching the memory state back to the ON state again (Figure 7.7 (c)). The formation and rupture of conducting filaments between GZO nanorod grain boundaries and ZnO seed layer induces bipolar RS behavior.

Figures 7.8 (a)-(c) show that the values of  $V_{ON}$  and  $V_{OFF}$  values of Devices 2, 3, and 4 are close, but Device 2 only has 55 successful switching cycles, which is substantially less than Devices 3 and 4 (with over 100 successive RS cycles each). This phenomenon demonstrates that the short circuit between the top and bottom electrodes easily occurs in porous nanorod thin films (i.e., Device 2) during RS operation.

Figures 7.9 (a)-(c) show the endurance characteristics of Devices 2, 3, and 4 and their resistance ratios of ON/OFF state, which are approximately 3, 9, and 10 times, respectively. Devices 3 and 4 with compact nanorod thin films, exhibited significantly greater endurance than Device 2, with porous nanorod film, and also provided sufficient memory margins to distinguish the two memory states. The device 2~4 are failure after their 50/100 DC cycles and the failure of device occurs at OFF state. We can deduce that the insufficient non-lattice oxygen ions are hard to recover the electron depleted oxygen vacancies under a  $V_{OFF}$ <sup>[7.24]</sup>.

Based on the PL spectra in Figure 7.5 and the defect equations, Device 2 exhibits much higher oxygen vacancy concentration than Devices 3 and 4, and easily forms conducting filaments along the nanorod surface. However, Device 2 also has porous nanorod film (Figure 7.2 (b)), which causes a large variation in  $R_{ON}$  ( $44.9 \pm 14.3 \Omega$ ) and  $R_{OFF}$  ( $532.0 \pm 143.7 \Omega$ ) to decrease the resistance ratio. Devices 3 and 4 have lower concentrations of oxygen vacancies than device 2, but Devices 3 and 4 exhibit highly compact nanorod thin films. This indicates that Device 3 and 4 still have sufficient oxygen vacancies existed between GZO nanorods (grain boundaries) to easily form

the conducting filaments at the grain boundaries. Moreover, the compact GZO nanorod thin films provide more stable  $R_{ON}$  and  $R_{OFF}$  ( $41.4 \pm 8.1$  and  $840.3 \pm 71.8 \Omega$  for Device 4), larger resistance ratio, higher device yield, and longer RS operation.

Figure 7.10 shows the electrical pulse-induced resistance change properties of Device 4. The device can be successively switched between ON and OFF states by applying -8 and +6 V with a 1  $\mu$ s pulses width. The resistances of both ON and OFF states were measured at 0.1 V. Based on Yu and Wang propose model about pulse-induced measurement<sup>[7,25]</sup>, the pulse width decreases almost exponentially with increasing voltage pulse amplitude. In our experiment, the DC switching curve (I-V) show low ON/OFF switching voltages (Figure 7.6 (a)) with long switching time, but higher voltage is used during pulse measurement for obtaining short pulse width. After more than 60 pulse-induced switches, the resistance ratio of ON/OFF is still kept about 1.5 times. Obviously, highly compact GZO nanorod films (Devices 3 and 4) have reversible and stable bipolar RS properties, providing the potential for NVM applications.

Table 7.2 shows a summary and comparison of the performance of various ZnO nanorod RS devices. Results indicate that the our Au/ZnO nanorod films/ZnO/Au RS devices exhibit the same bipolar RS behavior as the other reported nanorod or nanobelt devices , but have low operation voltage, good device yield, and high speed operation (1  $\mu$ s).

#### **7-4. Conclusions**

In summary, this study reports the successful fabricated of compact GZO nanorod thin film devices to avoid the short circuit between top and bottom electrodes without any embedded process. This study also demonstrates the reversible and stable bipolar RS characteristics of the GZO nanorod thin film devices. The formation and

rupture of conducting filaments in the grain boundaries between GZO nanorods and ZnO seed layer can accurately explain the switching mechanism of the GZO nanorod thin film devices. A 1D nanorod provides a straight and extensible conducting filament along the nanorod side wall, resulting in stable RS behavior. The results of this study confirm that the compact GZO nanorod thin films structure is a promising candidate for RRAM applications.



**Table 7.1** Relationship of Ga/Zn molar ratio in solution, pH of the solution and real Ga/Zn atomic ratio in GZO nanorod.

<b>Device #</b>	<b>Ga/Zn molar ratio in solution (%)</b>	<b>pH value of the solution</b>	<b>Real Ga/Zn molar ratio of GZO nanorods based on EDS analyzed results (%)</b>
Device 1	0	7.0±0.2	0
Device 2	6	9.0±0.2	6.06±0.24
Device 3	8	9.3±0.1	7.44±0.47
Device 4	10	9.4±0.1	9.00±0.31



**Table 7.2** Comparison of RS characteristic for various ZnO nanostructure devices.

Device structure	Switching behavior	$ V_{ON} $ (V)	$ V_{OFF} $ (V)	Endurance cycles	Yield (%)	ON speed	OFF speed	Ref.
Single Sb-doped ZnO nanobelts/SiO <sub>x</sub> /p-Si	bipolar	6	2.2	–	–	–	–	(16)
Pt/ZnO nanorods/ ITO	bipolar	0.7	0.6	120	–	–	–	(15)
Al/ZnO nanorods embedded in PMMA/ITO	bipolar	2	1.5	200	–	–	–	(17)
Au/ZnO nanorod thin films/ZnO/Au (Device 4)	bipolar	0.9	0.8	100	55%	1 $\mu$ s	1 $\mu$ s	This work

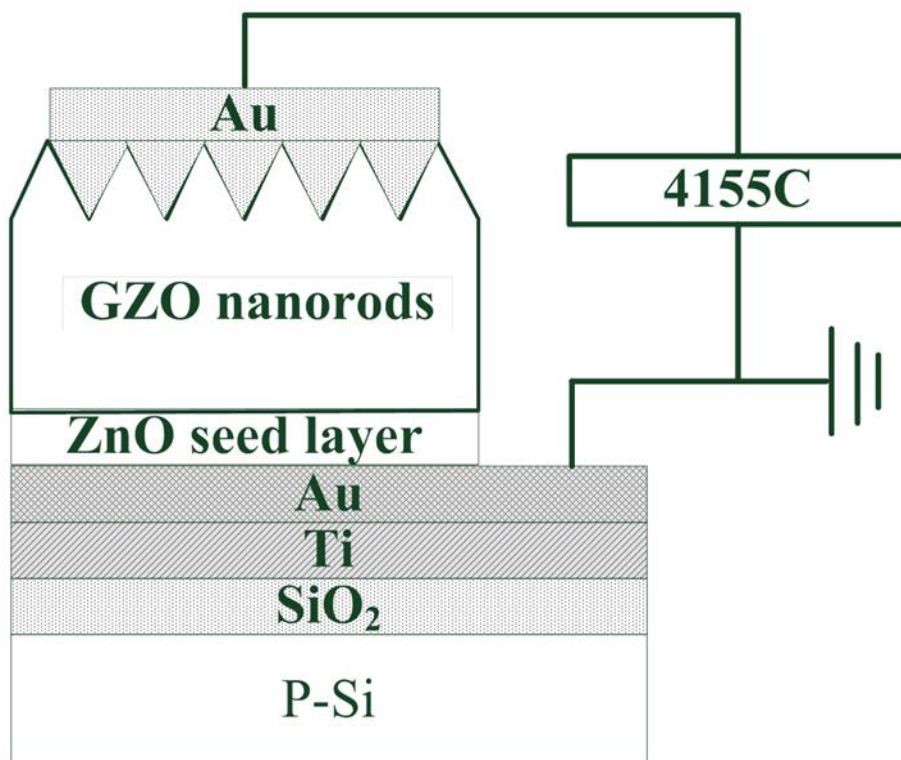


**Figure 7.1** Schematic structure of the Au/GZO nanorod thin films/ ZnO/Au device structure.

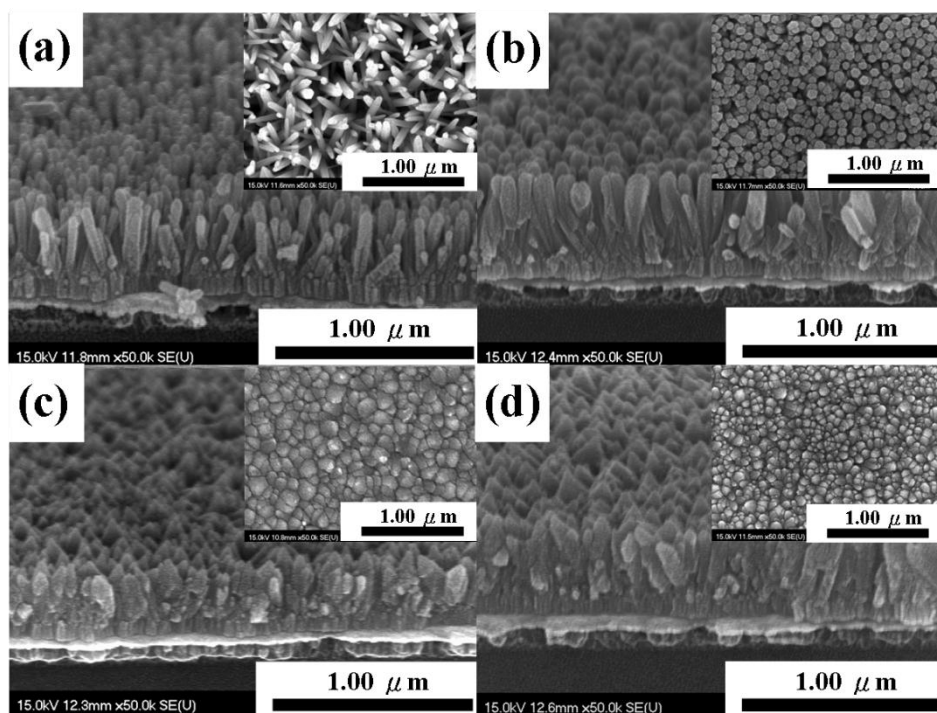


**Figure 7.2** Typical FE-SEM cross sectional images of (a) Device 1, (b) Device 2, (c) Device 3 and (d) Device 4; (insets of (a)-(d) are top view of the Devices 1, 2, 3, and 4, respectively).

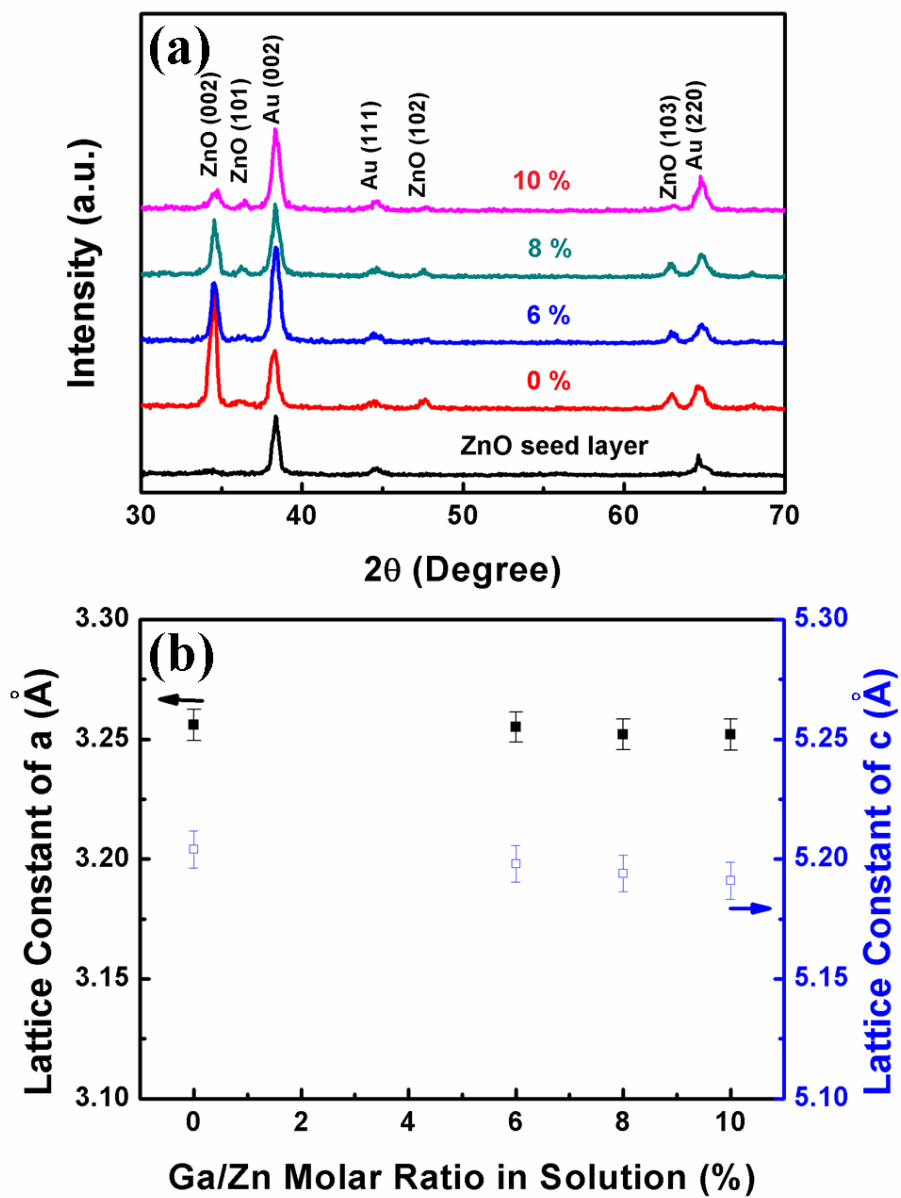


**Figure 7.3** (a) XRD analysis and (b) a-axis and c-axis lattice parameters of the GZO nanorod thin films with various Ga/Zn molar ratios in the solutions.

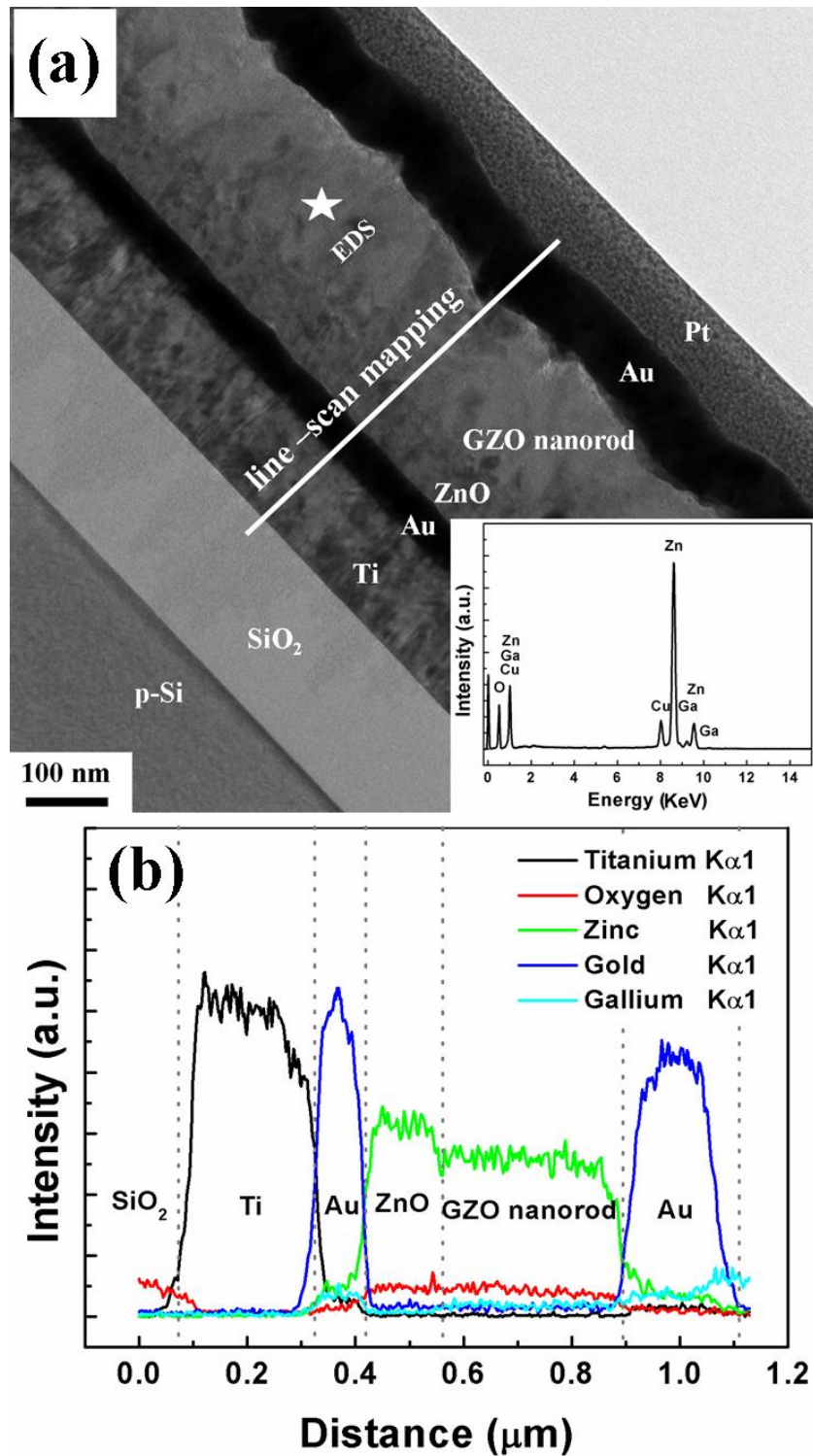


**Figure 7.4** (a) TEM bright field image of Device 4 (the inset is EDS analyzed result of the point indicated) and (b) EDS element line profiles of Device 4.

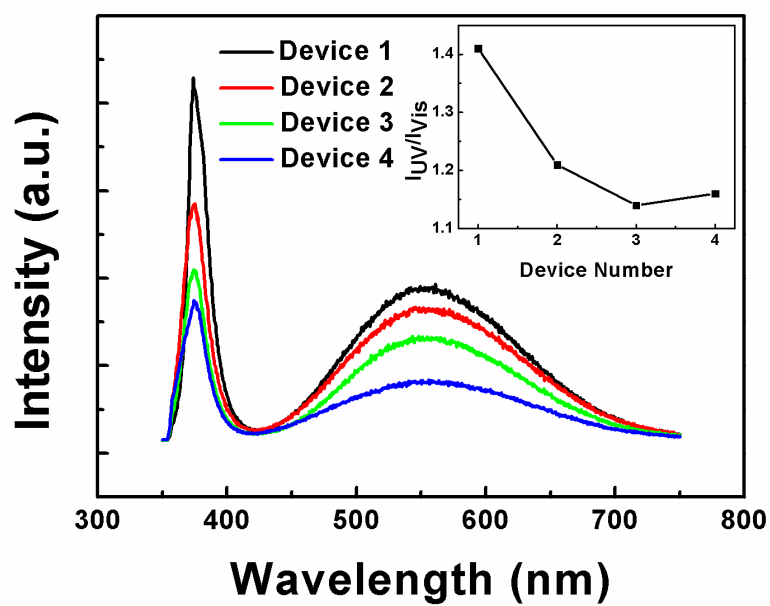


**Figure 7.5** Photoluminescence spectra of the Devices 1, 2, 3, and 4.

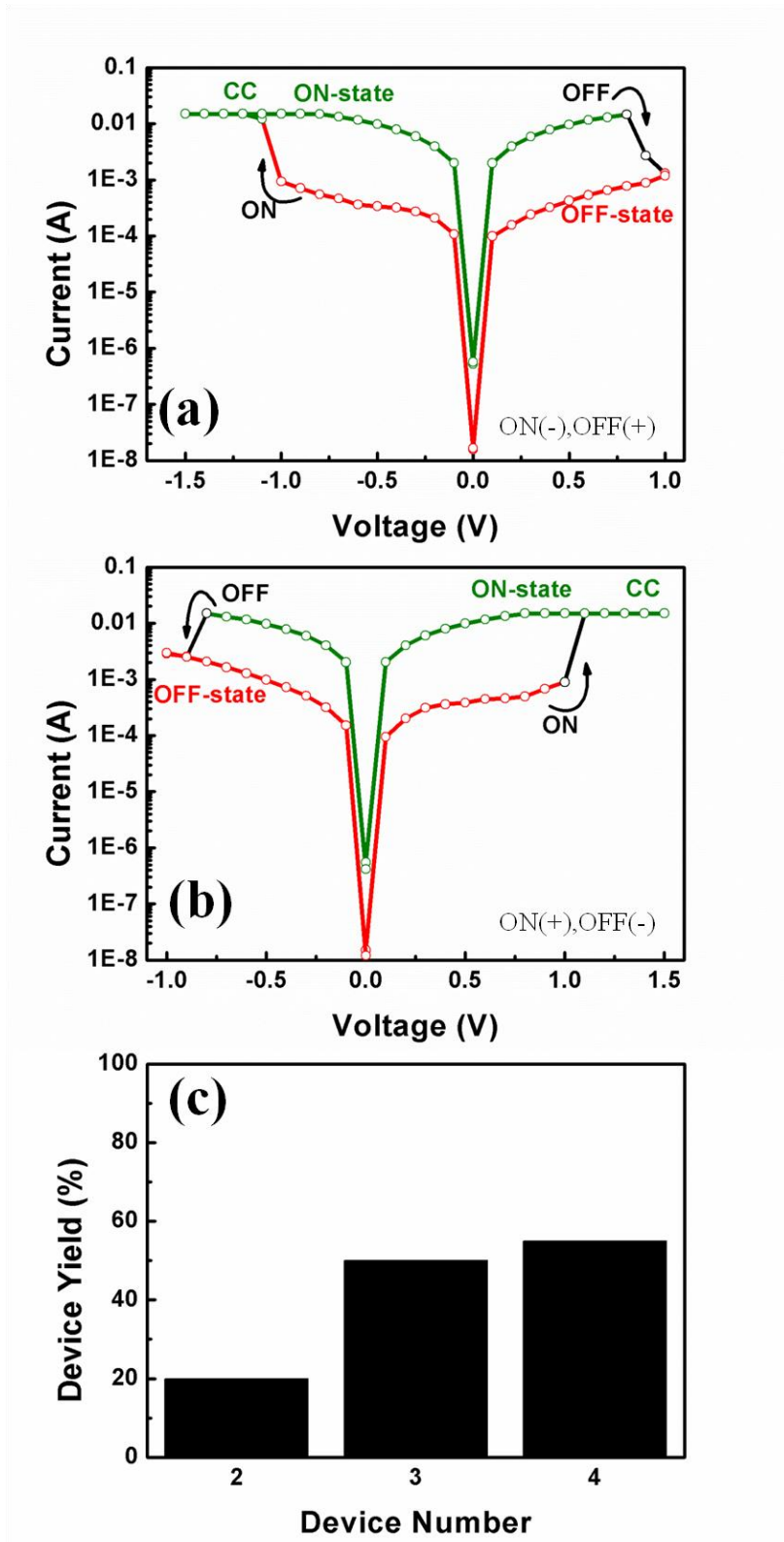


**Figure 7.6** (a) and (b) Typical bipolar RS I-V curve of Device 4. (c) The yield of the Device 2, 3, and 4, respectively.

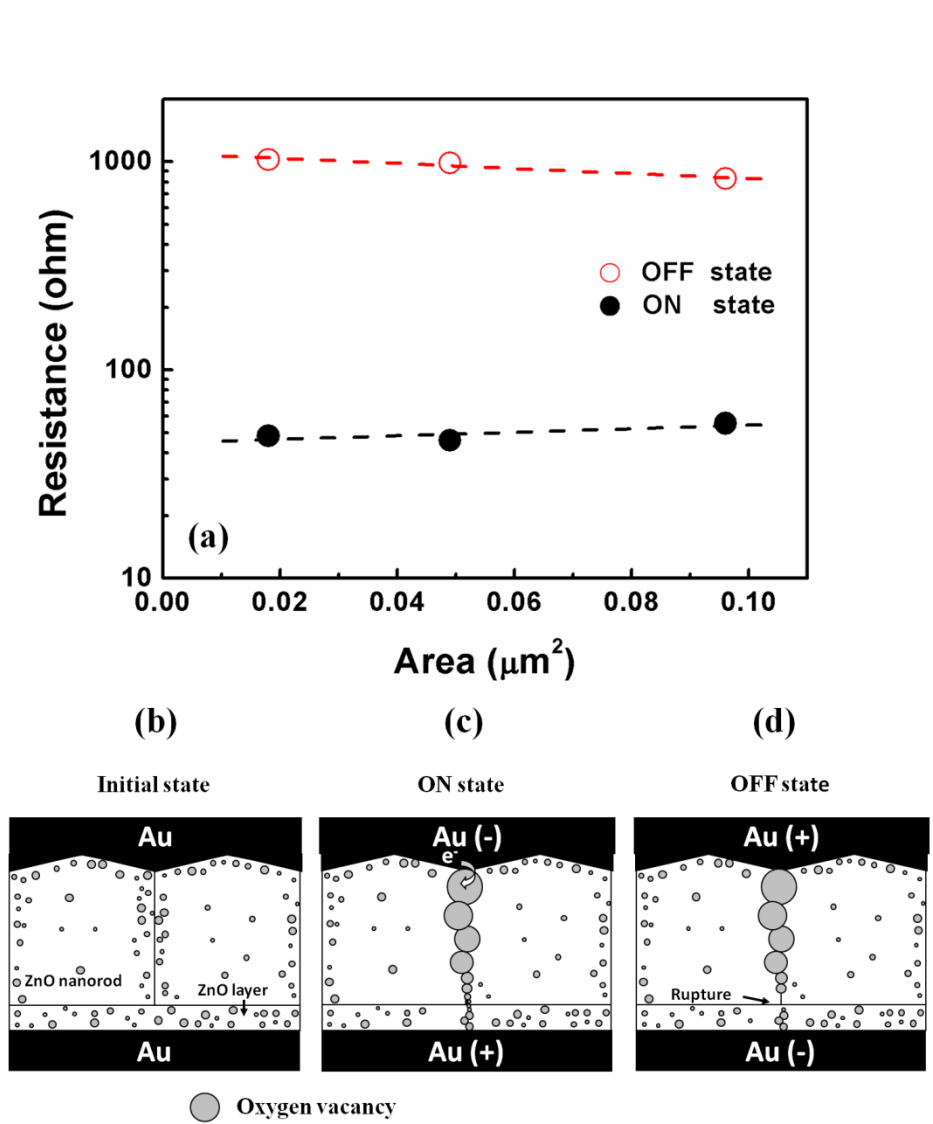


**Figure 7.7** (a) Pattern size dependence of the resistance value in the ON and OFF states. (b)-(d) Schematic diagrams of bipolar RS mechanism of GZO nanorod film devices through the formation/rupture of conducting filaments formed between GZO nanorod side wall and ZnO seed layer.



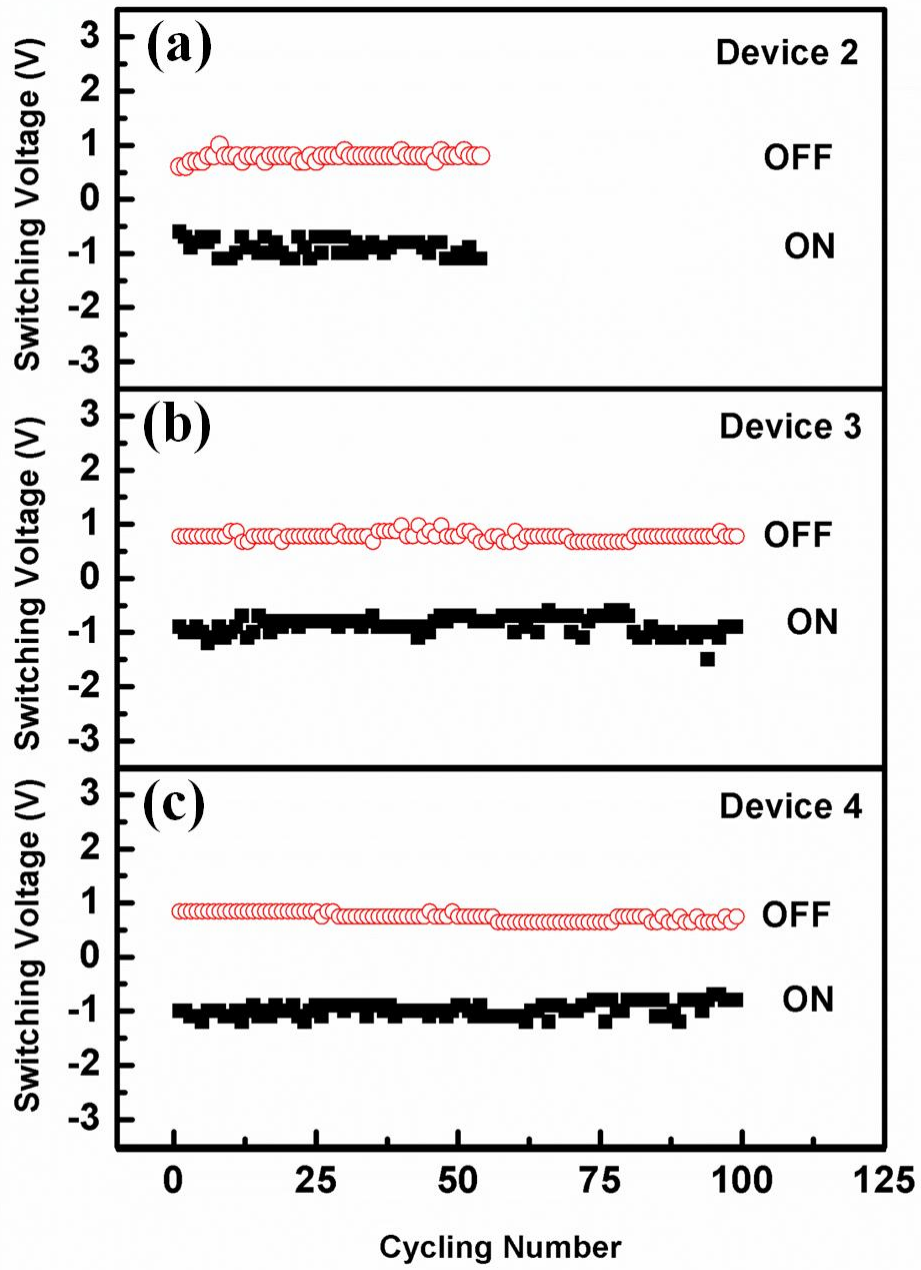


**Figure 7.8** Endurance cycle plots of  $V_{ON}$  and  $V_{OFF}$  of Devices (a) 2, (b) 3, and (c) 4.

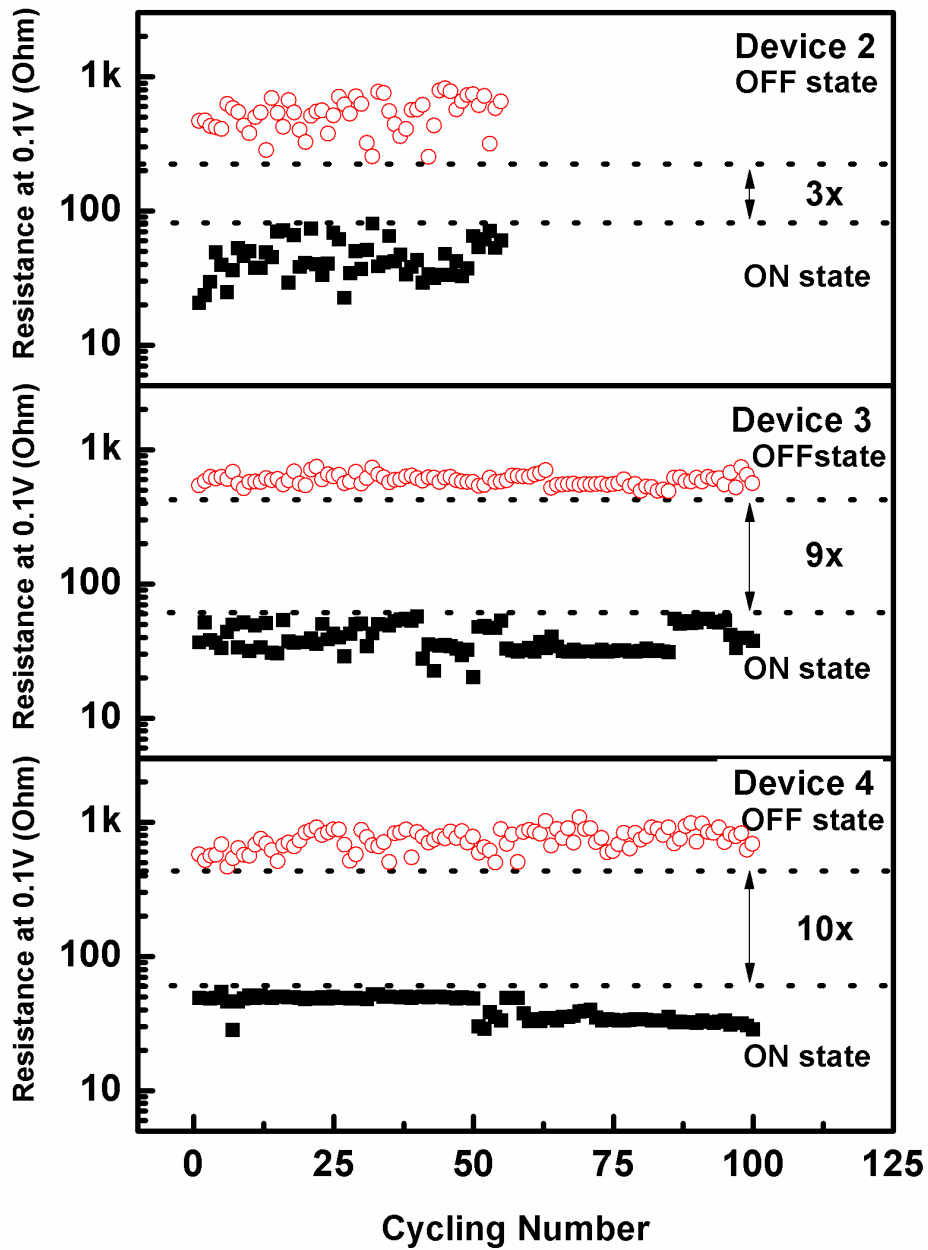


**Figure 7.9** Endurance cycle plots of the ON and OFF resistances of Devices (a) 2, (b) 3, and (c) 4.

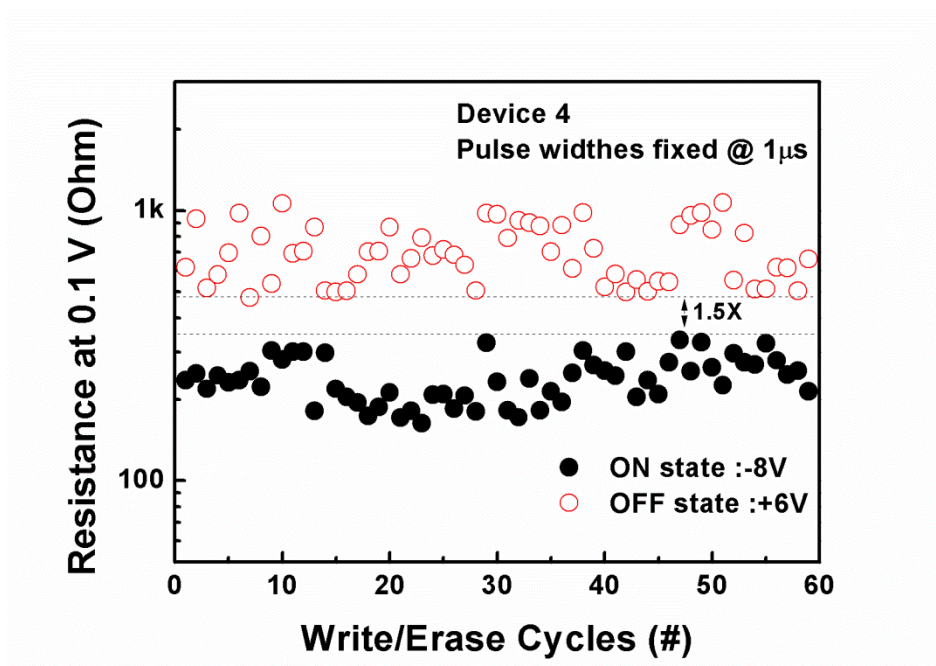


**Figure 7.10** Dynamic pulse-induced resistive switching of Device 4. Applying a -8 V 1 $\mu$ s to switch the memory state to ON state and applying a +6 V 1 $\mu$ s pulse to switch it back to the OFF state.

# Chapter 8

## Summary and Conclusions

The emerging technologies and production methods for the ZnO nanostructures application such as Ar and O<sub>2</sub> plasma etching, spin coating, ultra-fast chemical solution growth, and dense nanorod array, are introduced at first. Some important effects, ZnO nanostructures growth mechanisms, control ZnO nanostructure morphology and ZnO nanostructures application are organized, compared, and discussed as well.

The effects of emitter morphologies on field emission characteristics and mechanism of chemical and plasma etching are studied in Chapter 2. The sharp tip structured ZnO nanorods by employing etching process. Through plasma etching, the 110° tip angle ZnO nanorods were obtained. In order control emitter morphologies, we proposed two-step etching process, a combination of chemical etching process and plasma etching process were able to easily control tip angle of the nanorods. After such plasma etching and two-step etching processes, the field emission properties of ZnO vertically aligned nanorod emitters were significantly enhanced (turn-on field: 1.70 V/μm) and the stability of their turn-on fields was improved (turn-on field: 1.60±0.41 V/μm for 5000 s).

The 85° tip angle ZnO nanorods exhibited lower turn-on field and field emission stability for 5000 s, however, the large dispersion of turn-on field and unknown environmental stability in tip angle (85°) ZnO nanorods limit their development in realizing the practical field emission application. In Chapter 3, the effects of oxygen plasma treatments, at various etching times on the field emission characteristics (turn-on field dispersion and environmental stability) of ZnO nanorod emitters are

demonstrated. The synthesized process is simple, low cost and enable to large scale production. The (002) orientation and tip-structured morphology of the nanorod emitters were proved by XRD pattern, FE-SEM and TEM observations. The PL spectrum reveals that the green emission peak that occurred from oxygen vacancies after oxygen plasma treatment is lowered and obviously this phenomenon is due to reduced the concentration of oxygen vacancies of the nanorod emitters. The tip structured ( $100^\circ$ ) nanorod emitters also can be formed after oxygen plasma treatment. Thus, through oxygen plasma treatment, the tip ( $100^\circ$ ) structured ZnO nanorod emitters have enhanced performance including lower turn-on ( $2.42 \text{ V}/\mu\text{m}$ ) and threshold fields ( $3.61 \text{ V}/\mu\text{m}$ ), higher field enhancement factor (2268), good stability characteristics over  $10^4 \text{ s}$  (turn-on field, threshold field and field enhancement factor are  $2.34\pm 0.21 \text{ V}/\mu\text{m}$ ,  $3.87\pm 0.18 \text{ V}/\mu\text{m}$  and  $2252.8\pm 107.5$ , respectively) at room temperature. In addition, the tip structured ZnO nanorod emitters can successfully and stably operate up to  $100^\circ \text{C}$  without notable degradation of emission properties. Therefore, oxygen plasma treatment could be used improve electron field emission and light emitting applications.

Chemical etching and plasma etching are reported to improve and stabilize field emission behavior of ZnO nanorod emitters, but it requires to carefully controlling the chemical etching conditions such as solution concentration, temperature and etching time to form the convex morphology, which is not appropriate for the field emission application. In Chapter 4, ZnO nanotip ( $20^\circ$ ) emitters were successfully fabricated by employing the combination of chemical solution growth and oxygen plasma treatment. The synthesized process is simple, fast, lower cost and enable to large scale production. The nanotip emitters exhibit the (002) highly preferred orientation and small tip angle morphology proved by XRD patterns, FE-SEM and TEM observations. The nanotip emitters have turn-on field of  $1.07 \text{ V}/\mu\text{m}$ , threshold electric field of  $1.63$

V/ $\mu\text{m}$ , field enhancement factor of 4735 and exhibit stable and reproducible field emission properties at 25-100 °C. Such good performances is attributed to reduced oxygen vacancy concentration, small tip angle of 20°, smooth edge surface of the emitter and a better crystallinity obtained for ZnO nanotip (20°) emitters after the oxygen plasma etching process. The ZnO nanotip emitters have high potential for application in electron field emission and light emitting devices in the future.

The effects of SnO<sub>2</sub> thickness of ZnO-SnO<sub>2</sub> core-shell nanowires on gas sensor characteristics and mechanism of adsorption and desorption are studied in Chapter 5. The ZnO-SnO<sub>2</sub> core-shell nanowires had a single crystal ZnO cores and amorphous SnO<sub>2</sub> shell layer by two-step chemical growth. Through spin coating, the SnO<sub>2</sub> shell layer uniformly coated onto the ZnO nanowires and the various SnO<sub>2</sub> shell layer thickness were obtained by adjusting spin coating times. The H<sub>2</sub> gas sensors were fabricated by these core shell nanowires using silver layer as the electrode. High sensitivity (80 %) at both low H<sub>2</sub> concentration (25 ppm) and low working temperature (250 °C) was obtained. The core shell nanowire sensor with good sensitivity has high potential in gas sensor application.

The effects of length of ZnO nanorods on PET substrate for UV photodetector application and mechanism of adsorption and desorption are studied in Chapter 6. We successfully develop a simple method to fabricate high performance ZnO UV photodetector on the flexible PET substrate. Through chemical solution method, the ZnO nanorods uniformly grow on the PET substrate and the various ZnO nanorods lengths are obtained by adjusting growth time. The ZnO-10/PET structure reveals good mechanical stability through bending test. Upon UV illumination, the ZnO-10 nanorods photodetector exhibits high sensitivity at low UV power density (25  $\mu\text{W}/\text{cm}^2$ ), fast recovery time (120 sec), good orientation properties, reproducible photoresponse (20 cycles) and multi-level photoresponse. The ZnO-10/PET

photodetector made by a simple process has high potential for practical applications.

The resistive switching behavior of Ga-doped ZnO (GZO) nanorod thin films with various Ga/Zn molar ratios are investigated in Chapter 7. We successfully fabricated compact GZO nanorod thin film devices to avoid the short circuit between top and bottom electrodes without any embedded process and demonstrate the reversible and stable bipolar RS characteristics. The formation and rupture of conducting filaments in the grain boundaries between GZO nanorods and ZnO seed layer can accurately explain the switching mechanism of the GZO nanorod thin film devices. A 1D nanorod provides a straight and extensible conducting filament along the nanorod side wall, resulting in stable RS behavior. The results of this study confirm that the compact GZO nanorod thin film structure is a promising candidate for RRAM applications.



# Chapter 9

## Future Works and Suggestion

The metal oxide nanostructures, especially ZnO material have potentials for much field application such as field emission display, optical emission and resistance random access memory. Furthermore, the studies of ZnO nanostructures are still narrow focus on the electric and optical applications. In the future, there are many kinds of subjects could be study wick will increase the speed of commercialize. About the ZnO nanostructures, there are some suggestions to study in the future as follow:

- (1) Establishing new ZnO nanotips field emission device and improve screen effect. Improving the screening effect which could focus on the convenient lithography process (polystyrene (PS) nanosphere or nanoimprint lithography). Figure 9.1 shows a schematic view of the new ZnO nanotips field emission device.
- (2) Studying other structure of GZO nanorod memory devices. The new structure employ the metal oxide/GZO nanorods double layer RRAM which have opportunity to reveal unipolar RS behaviors in the future. The device structure shown in Figure 9.2
- (3) Attempting the single ZnO nanowire device which will offer any kinds of potentials for application (sensor, generator and RRAM) in the future. The prodcution methods involve focus ion beam (FIB) or e-beam lithography. Figure 9.3 show the single ZnO nanowire devices.
- (4) Studying other metal oxide nanostructures that could find many new applications in each field of the nanotechnology.



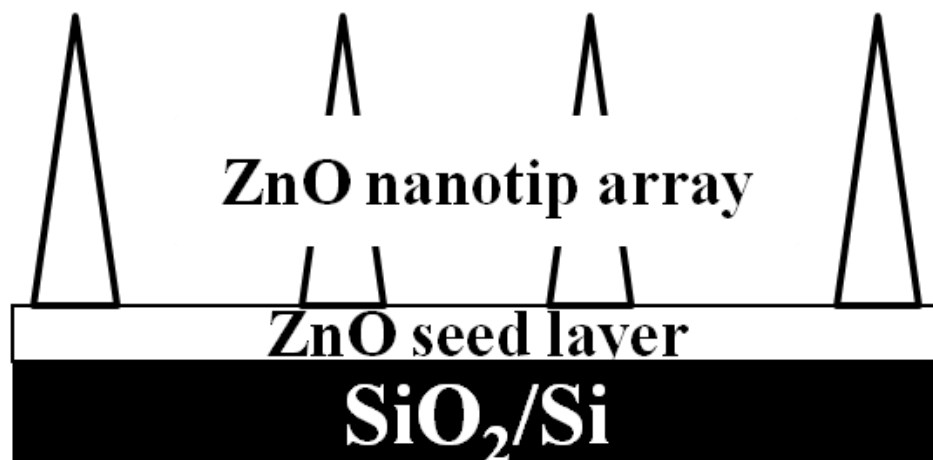


**Figure 9.1** The illustration of the new ZnO nanotip field emission device.

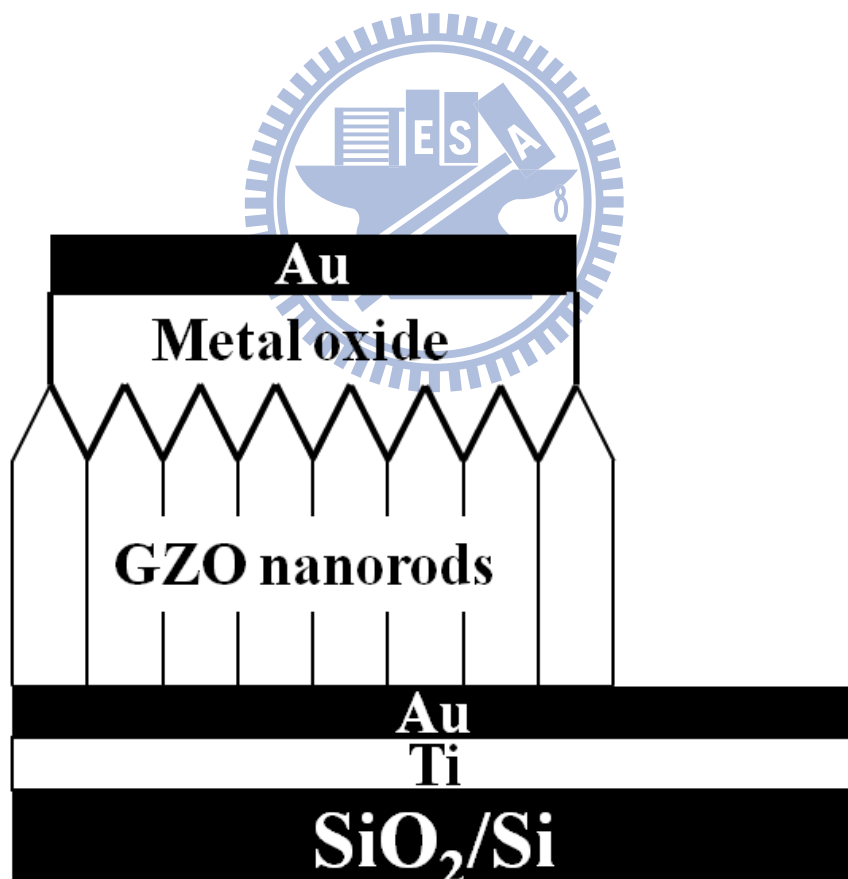


**Figure 9.2** The schematic illustration of the metal oxide/GZO nanorods double layer RRAM device.

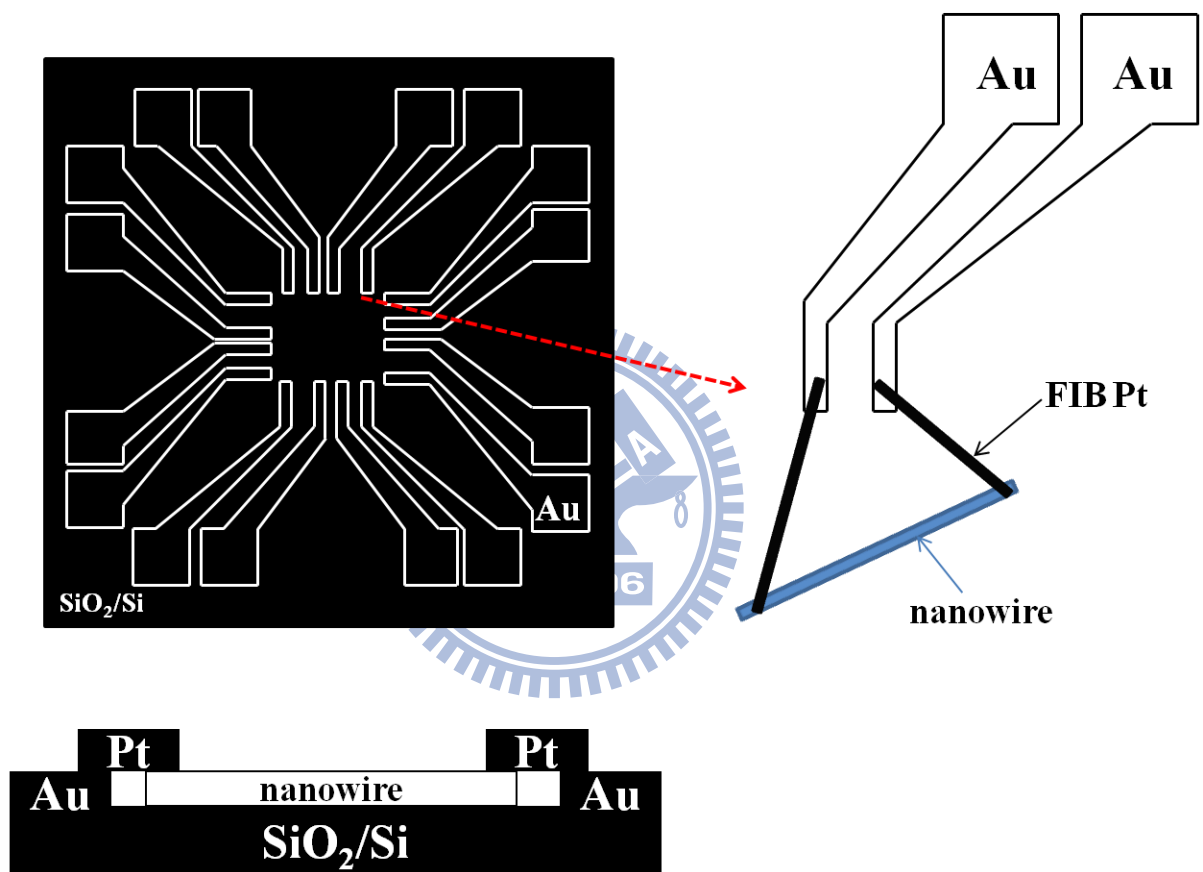


**Figure 9.3** The schematic illustration of the single ZnO nanowire device.

## References

### Chapter 1

- [1.1] NRC Report, "Small Wonders, Endless Frontiers: Review of the National Nanotechnology Initiative," National Research Council, 2002.
- [1.2] R. Waser, *Nanoelectronics and Information Technology*, Wiley, Germany, 2003.
- [1.3] H. Weller, "Quantized semiconductor particles: A novel state of matter for materials science," *Adv. Mater.*, Vol. 5, pp. 88-95, 1993.
- [1.4] Y. J. Xiong, and Y. N. Xia, "Shape-controlled synthesis of metal nanostructures: The case of palladium," *Adv. Mater.*, Vol. 19, pp. 3385-3391, 2007.
- [1.5] Y. C. Shiang, C. C. Huang, and H. T. Chang, "Gold nanodot-based luminescent sensor for the detection of hydrogen peroxide and glucose," *Chem. Comm.*, Vol. 45, pp. 3437-3439, 2009.
- [1.6] T. Seto, Y. Kawakami, N. Suzuki, M. Hirasawa, and N. Aya, "Laser synthesis of uniform silicon single nanodots," *Nano Lett.*, Vol. 1, pp.315-318, 2001.
- [1.7] W. Shi, Q. Wang, Y. Long, Z. Cheng, S. Chen, H. Zheng, and Y. Huang, "Carbon nanodots as peroxidase mimetics and their applications to glucose detection," *Chem. Comm.*, Vol. 47, pp. 6695-6697, 2011.
- [1.8] Z. L. Wang, "Zinc oxide nanostructures: growth, properties and applications," *J. Phy. :Condens. Matter*, Vol. 16, pp. R829-R858, 2004.
- [1.9] S. Iijima, and T. Ichihashi, "Single-shell carbon nanotubes of 1-nm diameter," *Nature*, Vol. 363, pp. 603-605, 1993.
- [1.10] S. Xu, Y. Qin, Y. Wei, R. Y. Yang, and Z. L. Wang, "Self-powered nanodevices," *Nature Nanotechnology*, Vol. 5, pp. 366-374, 2010.
- [1.11] B. Wang, L. F. Zhu, Y. H. Yang, N. S. Xu, and G. W. Yang, "Fabrication of a SnO<sub>2</sub> nanowire gas sensor and sensor performance for hydrogen," *J. Phys. Chem. C*, vol. 112, pp. 6643-6647, 2008.
- [1.12] W. A. Heer, A. Chatelain, D. Ugarte, "A carbon nanotube field-emission electron source," *Science*, Vol. 270, pp. 1179-1180, 1995.
- [1.13] C. Soci, A. Zhang, X. Y. Bao, H. Kim, and D. Wang, "Nanowire photodetectors," *J. Nanosci. & Nanotechnol.*, Vol. 10, pp.1-20, 2010.
- [1.14] J. Zhang, M. K. Li, L. Y. Yu, L. L. Liu, H. Zhang, and Z. Yang, "Synthesis and piezoelectric properties of well-aligned ZnO nanowire arrays via a simple solution-phase approach," *Appl. Phys. A*, Vol. 97, pp. 869-876, 2009.
- [1.15] A. Yamada, B. Sang, and M. Konagai, "Atomic layer deposition of ZnO transparent conducting oxides," *Appl. Surf. Sci.*, Vol. 112, pp.216-222, 1997.
- [1.16] D. C. Look, B. Claflin, Y. I. Alivov, and S. J. Park, "The future of ZnO UV light emitters," *Phys. Stat. Sol. A*, Vol. 201, pp. 2203-2211, 2004.

- [1.17] R. Janisch, P. Gopal, N. A. Spaldin, "Transition metal-doped TiO<sub>2</sub> and ZnO-present status of the field," *J. Phy.: Condens. Matter*, Vol. 17, pp. R657-R689, 2005.
- [1.18] S. J. Pearton, D. P. Norton, K. Ip, Y. W. Heo, and T. Steiner, "Recent process in processing and properties of ZnO," *Prog. In Mater. Sci.*, Vol. 50, pp. 293-340, 2005.
- [1.19] D. S. Kang, S. K. Han, J. H. Kim, S. M. Yang, J. G. Kim, S. K. Hong, D. Kim, and H. Kim, "ZnO nanowires prepared by hydrothermal growth followed by chemical vapor deposition for gas sensors," *J. Vac. Sci. Technol. B*, Vol. 27, pp. 1667-1672, 2009.
- [1.20] T. J. Hsueh, Y. W. Chen, S. J. Chang, S. F. Wang, C. L. Hsu, Y. R. Lin, T. S. Lin, and I. C. Chen, "ZnO nanowire-based Co sensor prepared at various temperatures," *J. Electro. Soc.*, Vol. 154, pp. J393-396, 2007.
- [1.21] H. W. Ra, D. H. Choi, S. H. Kim, and Y. H. Im, "Formation and characterization of ZnO/a-C core-shell nanowires," *J. Phys. Chem. C*, Vol. 113, pp. 3512-3516, 2009.
- [1.22] X. Wang, C. J. Summers, and Z. L. Wang, "Large scale hexagonal-patterned growth of aligned ZnO nanorods for nano-optoelectrics and nanosensor arrays," *Nano Let.*, Vol. 4, pp. 423-426, 2004.
- [1.23] S. Panigrahi, and D. Basak, "Core-shell TiO<sub>2</sub>-ZnO nanorods for efficient for ultraviolet photodetection," *Nanoscale*, Vol. 3, pp. 23362341, 2011.
- [1.24] D. F. Liu, Y. J. Xiang, Q. Liao, J. P. Zhang, Z. X. Zhang, L. F. Liu, W. J. Ma, J. Shen, W. Y. Zhou, and S. S. Xie, "A simple route to scalable fabrication of perfectly ordered ZnO nanorod arrays," *Nanotechnology*, Vol. 18, pp. 405303-1-5, 2207.
- [1.25] W. D. Yu, X. M. Li, and X. D. Gao, "Self-catalytic synthesis and photoluminescence of ZnO nanostructure on ZnO nanocrystal substrates," *Appl. Phys. Lett.*, Vol. 84, pp. 2658-2660, 2004.
- [1.26] Y. Dai, Y. Zhang, Z. L. Wang, "The octa-twin tetraleg ZnO nanostructures," *Solid State Comm.*, Vol. 126, pp. 629-, 2003
- [1.27] H. Yan, R. He, J. Pham, and P. Yang, "Morphogenesis of one-dimensional ZnO nano- and microcrystals," *Adv. Mater.*, Vol. 15, pp.402-405, 2003.
- [1.28] B. D. Yao, Y. F. Chan, and N. Wang, "Formation of ZnO nanostructures by a simple way of thermal evaporation," *Appl. Phys. Lett.*, Vol. 81, pp. 757-759, 2002.
- [1.29] Y. J. Xing, Z. H. Xi, X. D. Zhang, J. H. Song, and R. M. Wang, "Thermal evaporation synthesis of zinc oxide nanowires," *Appl. Phys. A*, Vol. 80, pp. 1527-1530, 2005.

- [1.30] Y. Zhang, L. Wang, X. Liu, Y. Yan, C. Chen, and J. Zhu, "Synthesis of nano/micro zinc oxide rods and arrays by thermal evaporation approach on cylindrical shape substrate," *J. Phys. Chem. B*, Vol. 109, pp. 13091-13093.
- [1.31] H. Lv, D. D. Sang, H. D. Li, X. B. Du, D. M. Li, and G. T. Zou, "Thermal evaporation synthesis and properties of ZnO nano/microstructures using carbon Group elements as the reducing agents," *Nanoscale Res. Lett.*, Vol. 5, pp. 620-624, 2010.
- [1.32] D. Calestani, M. Z. Zha, L. Zanotti, M. Villani, and A. Zappettini, "Low-temperature thermal evaporation growth of aligned ZnO nanorods on ZnO films: a growth mechanism promoted by Zn nanoclusters on polar surfaces," *Cryst. Eng. Comm.*, Vol. 13, pp. 1707-1712, 2011.
- [1.33] W. I. Paek, D. H. Kim, S. W. Jung, and G. C. Yi, "Metalorganic vapor-phase epitaxial growth of vertically well-aligned ZnO nanorods," *Appl. Phys. Lett.*, Vol. 80, pp. 4232-4234, 2002.
- [1.34] W. Park, and G. C. Yi, "Electroluminescence in n-ZnO nanorod arrays vertically grown on p-GaN," *Adv. Mater.*, Vol. 16, pp. 87-90, 2004.
- [1.35] Y. Ishikawa, Y. Shimizu, T. Sasaki, and N. Koshizaki, "Preparation of zinc oxide nanorods using pulsed laser ablation in water media at high temperature," *J. Coll. and Inter. Science*, Vol. 300, pp.612-615, 2006.
- [1.36] H. He, W. Cai, Y. Lin, and B. Chen, "Surface decoration of ZnO nanorod arrays by electrophoresis in the Au colloidal solution by laser ablation in water," *Langmuir*, Vol. 26, pp. 8925-8932, 2010.
- [1.37] Y. Zhao, and Y. Uk Kwon, "Templateless hydrothermal synthesis of aligned ZnO nanorods," *Chem. Lett.*, Vol. 33, pp. 1578-1579, 2004.
- [1.38] B. Liu, and H. C. Zeng, "Hydrothermal synthesis of ZnO nanorods in the diameter regime of 50 nm," *J. Am. Chem. Soc.*, Vol. 125, pp. 4430-4431, 2003.
- [1.39] O. Akhavan, M. Mehrabian, K. Mirabbaszadeh, and R. Azimirad, "Hydrothermal synthesis of ZnO nanorod arrays for photocatalytic inactivation of bacteria," *J. Phys. D. Appl. Phys.*, Vol. 42, pp. 225305-1-10, 2009.
- [1.40] M. Guo, P. Diao, and S. Cai, "Hydrothermal growth of perpendicularly oriented ZnO nanorod array film and its photoelectrochemical properties," *Appl. Surface Sci.*, Vol. 249, pp. 71-75, 2005.
- [1.41] A. Huczko, "Template-based synthesis of nanomaterials," *Appl. Phys. A*, Vol. 70, pp. 365-376, 2000.
- [1.42] G. C. Yi, C. Wang, and W. II Park, "ZnO nanorods: synthesis characterization and application," *Semicond. Sci. Technol.*, Vol. 20, pp. s22-s44, 2005.

- [1.43] S. Cho, H. Jeong, D. H. Park, S. H. Jung, H. J. Kim, and K. H. Lee, "The effect of vitamin on ZnO crystal formation," *Cryst. Eng. Comm.*, Vol. 12, pp. 968-976, 2010.
- [1.44] Y. Wei, Y. Dong, C. Li, S. Xu, J. H. Ryo, R. Dupuis, A. K. Sood, D. L. Polla, and Z. L. Wang, "Growth of vertically aligned ZnO nanobelt arrays on GaN substrate," *J. Phys. Chem. C*, Vol. 112, pp. 18935-18937, 2008.
- [1.45] C. S. Lao, J. Liu, P. Gao, L. Zhang, D. Davidovic, R. Tummala, and Z. L. Wang, "ZnO nanobelt/nanowire schottky diodes formed by dielectrophoresis alignment across Au electrodes," *Nano Lett.*, Vol. 6, pp. 263-266, 2006.
- [1.46] B. Liu, and H. C. Zeng, "Direct growth of enclosed ZnO nanotubes," *Nano Res.*, Vol. 2, pp. 201-209.
- [1.47] J. Han, F. Fan, C. Xu, S. Lin, M. Wei, X. Duan, and Z. L. Wang, "ZnO nanotube-based dye-sensitized solar cell and its application in self-powered devices," *Nanotechnology*, Vol. 21, pp. 405203-1-7, 2010.
- [1.48] P. X. Gao, Y. Ding, and Z. L. Wang, "electronic transport in superlattice-structured ZnO nanohelices," *Nano Lett.*, Vol. 9, pp. 137-143, 2009.
- [1.49] H. Gao, X. Zhang, M. Zhou, E. Zhou, E. Zhang, and Z. Zhang, "Super-uniform ZnO nanohelices synthesized via thermal evaporation" *Solid state Comm.*, Vol. 140, pp. 455-458, 2006.
- [1.50] W. L. Hughes, and Z. L. Wang, "Controlled synthesis and manipulation of ZnO nanorings and nanobows," *Appl. Phys. Lett.*, Vol. 86, pp.043106-1-3, 2005.
- [1.51] X. Y. Kong, Y. Ding, R. Yang, and Z. L. Wang, "Single-crystal nanorings formed by epitaxial self-coiling of polar nanobelts," *Science*, Vol. 303, pp. 1348-1351, 2004.
- [1.52] S. K. Park, J. H. Park, K. Y. Ko, S. Yoon, K. S. Chu, W. Kim, and Y. R. Do, "Hydrothermal-electrochemical synthesis of ZnO nanorods," *Cryst. Growth Des.*, Vol. 9, pp. 3615-3620, 2009.
- [1.53] R. Chander, and A. K. Raychaudhuri, "Electrodeposition of aligned arrays of ZnO nanorods in aqueous solution," *Solid State Comm.*, Vol. 145, pp. 81-85, 2008.
- [1.54] R. S. Wagner, and W. C. Ellis, "Vapor-liquid-solid mechanism of single crystal growth," *Appl. Phys. Lett.*, Vol. 4, pp. 89-90, 1964.
- [1.55] S. Barth, F. H. Ramirez, J. D. Holmes, and A. R. Rodriguez, "Synthesis and applications of one-dimensional semiconductors," *Prog. In Mater. Sci.*, Vol. 55, pp. 563-627, 2005.
- [1.56] L. Chen, L. Luo, Z. Chen, M. Zhang, J. A. Zapfen, C. S. Lee, and S. T. Lee, "ZnO/Au composite nanowires as substrates for surface-enhanced raman scattering detection," *J. Phys. Chem. C*, Vol. 114, pp. 93-100, 2010.

- [1.57] S. Y. Li, C. Y. Lee, and T. Y. Tseng, "Copper-catalyzed ZnO nanowires on silicon (100) grown by vapor-liquid-solid process," *J. Cryst. Growth*, Vol. 247, pp. 357-362, 2003.
- [1.58] C. Geng, Y. Jiang, Y. Yao, X. Meng, J. A. Zapien, C. S. Lee, Y. Lifshitz, and S. T. Lee, "Well-aligned ZnO nanowire array fabricated on silicon substrate," *Adv. Funct. Mater.*, Vol. 14, pp. 589-594, 2004.
- [1.59] P. Yang, H. Yan, S. Mao, R. Russo, J. Johnson, R. Saykally, N. Morris, J. Phan, R. He, and H. J. Choi, "Controlled growth of ZnO nanowires and their optical properties," *Adv. Funct. Mater.*, Vol. 12, pp. 323-331, 2002.
- [1.60] Z. R. Dai, Z. W. Pan, and Z. L. Wang, "Novel nanostructures of functional oxides synthesized by thermal evaporation," *Adv. Funct. Mater.*, Vol. 13, pp. 9-24, 2003.
- [1.61] Z. L. Wang, "Nanostructures of zinc oxide," *Material Today*, Vol. 7 pp. 26-33, 2004.
- [1.62] C. H. Liu, W. C. Yiu, F. C. K. Au, J. X. Ding, C. S. Lee, and S. T. Lee, "Electrical properties of zinc oxide nanowires and intramolecular p-n junctions," *Appl. Phys. Lett.*, Vol. 83, pp. 3168-3170, 2003.
- [1.63] C. Y. Lee, S. Y. Li, P. Lin, and T. Y. Tseng, "ZnO nanowires hydrothermally grown on PET polymer substrate and their characteristics," *J. Nanosci. & Nanotech.*, Vol. 5, pp. 1088-1094, 2005.
- [1.64] L. Vayssieres, "On the design of advanced metal oxide nanomaterials," *Inter. J. Nanotech.*, Vol. 1, pp. 1-41, 2004.
- [1.65] L. Vayssieres, "Growth of arrayed nanorods and nanowires of ZnO from aqueous solutions," *Adv. Mater.*, Vol. 15, pp. 464-466, 2003.
- [1.66] M. A. Verges, A. Mifsud, and C. J. Serna, "Formation of rod-like zinc oxide microcrystals in homogeneous solutions," *J. Chem. Soc., Faraday Trans.*, Vol. 86, pp. 959-963, 1990.
- [1.67] L. E. Greene, M. Law, J. Goldberger, F. Kim, J. C. Johnson, Y. Zhang, R. J. Saykally, and P. Yang, "Low-temperature wafer-scale production of ZnO nanowire arrays," *Angew. Chem. Int. Ed.*, Vol. 42, pp. 3031-3034, 2004.
- [1.68] L. L. Xing, C. H. Ma, Z. H. Chen, Y. J. Chen, and X. Y. Xue, "High gas sensing performance of one-step-synthesized Pd-ZnO nanoflowers due to surface reactions and modifications," *Nanotechnology*, Vol. 22, pp. 215501-1-7, 2011.
- [1.69] Y. C. Chang, and L. J. Chen, "ZnO nanoneedles with enhanced and sharp ultraviolet cathodoluminescence peak," *J. Phys. Chem. C*, Vol. 111, pp. 1268-1272, 2007.
- [1.70] Y. Sun, D. J. Riley, and M. N. R. Ashfold, "Mechanism of ZnO nanotube growth by hydrothermal methods on ZnO film coated Si substrates," *J. Phys.*



- Chem. B*, Vol. 110, pp. 15186-15192, 2006.
- [1.71] F. Xu, Z. Y. Yuan, G. H. Du, M. Halasa, and B. L. Su, "High yield synthesis of single-crystalline ZnO hexagonal nanoplates and accounts of their and photocatalytic properties," *App. Phys. A*, Vol. 86, pp. 181-185, 2007.
- [1.72] Y. Sun, D. J. Riley, and N. R. Ashfold, "Mechanism of ZnO nanotube growth by hydrothermal methods on ZnO film-coated Si substrates," *J. Phys. Chem. B*, Vol. 110, pp. 15186-15192, 2006.
- [1.73] Z. Chen, and L. Gao, "A facile route to ZnO nanorod arrays using wet chemical method," *J. Cryst. Growth*, Vol. **293**, pp. 522-527, 2006.
- [1.74] H. Zhang, D. Yang, D. Li, X. Ma, S. Li, and D. Que, "Controllable growth of ZnO microcrystals by a capping-molecule-assisted hydrothermal process," *Cryst. Growth. Des.*, Vol. 5, pp. 547-550, 2005.
- [1.75] Z. Wang, Z. F. Qian, J. Yin, and Z. K. Zhu, "Large-scale fabrication of tower-like, flower-like, and tube-like ZnO arrays by a simple chemical solution route," *Langmuir*, Vol. **20**, pp. 3441-3448, 2004.
- [1.76] Q. Li, V. Kumar, Y. Li, H. Zhang, J. T. Mark, and R. P. H. Chang, "Fabrication of ZnO nanorods and nanotubes in aqueous solutions," *Chem. Mater.*, Vol. **17**, pp. 1001-1006, 2005.
- [1.77] S. Ma, G. Fang, C. Li, S. Sheng, L. Fang, Q. Fu, and X. Zhao, "Controllable synthesis of vertically aligned ZnO nanorod arrays in aqueous solution," *J. Nanosci. & Nanotech.*, Vol. 6, pp. 2062-2066, 2006.
- [1.78] T. Maruo, N. Ueno, S. Ichikawa, N. Nishiyama, Y. Egashira, and K. Ueyama, "Transmission electron microscopy study on the growth of zinc oxide crystals under hydrothermal conditions," *Mater. Lett.*, Vol. 63, pp. 2373-2376, 2009.
- [1.79] J. Cembrero, A. Elmanouni, B. Hartiti, M. Mollar, and B. Man, "Nanocolumnar ZnO films for photovoltaic applications," *Thin Solid Films*, Vol. 451-452, pp. 198-202, 2004.
- [1.80] J. Lee, and Y. Tak, "electrodeposition of ZnO on ITO electrode by potential modulation method," *Electrochem. Solid-State Lett.*, Vol. 4, pp. C63-63, 2001.
- [1.81] M. H. Wong, A. Berenov, X. Qi, M. J. Kappers, Z. H. Barber, B. Lilly, Z. Lockman, M. P. Ryan, and J. L. Macmanus-Driscoll, "Electrochemical growth of ZnO nano-rods on polycrystalline Zn foil," *Nanotechnology*, Vol. 14, pp. 968-973, 2003.
- [1.82] Q. Wang, G. Wang, J. Jie, X. Han, and J. G. Hou, "Annealing effect on optical properties of ZnO films fabricated by cathodic electrodeposition," *Thin Solid Films*, Vol. 492, pp. 61-65, 2005.
- [1.83] Z. Liu, Z. Jin, J. Qiu, X. Liu, W. Wu, and W. Li, "Preparation and



- characteristics of ordered porous ZnO films by a electrodeposition method using PS array templates,” *Semicond. Sci. Technol.*, Vol. 21, pp. 60-66, 2006.
- [1.84] L. Li, G. W. Meng, L. D. Zhang, and F. Phillip, “Ordered semiconductor ZnO nanowire arrays and their photoluminescence properties,” *Appl. Phys. Lett.*, Vol. 76, pp. 2011-2013, 2000.
- [1.85] Z. Fan, and J. G. Lu, “Zinc oxide nanostructures: Synthesis and properties,” *J. NanoSci. & Nanotech.*, Vol. 5, pp. 1561-1573, 2005.
- [1.86] C. C. Tang, S. S. Fan, M. L. Chapelle, and P. Li, “Silica –assisted catalytic growth oxide and nitride nanowires,” *Chem. Phys. Lett.*, Vol. 333, pp. 12-15, 2001.
- [1.87] W. Peng, M. Yanagida, L. Hun, and S. Ahmed, “Controlled fabrication of TiO<sub>2</sub> rutile nanorod/anatase nanoparticle composite photoanodes for dye-sensitized solar cell application,” *Nanotechnology*, Vol. 22, pp. 275709-1-5, 2011.
- [1.88] Y. Xi, J. Song, S. Xu, R. Yang, Z. Gao, C. Hu, and Z. L. Wang, “Growth ZnO nanotube arrays and nanotube based piezoelectric nanogenerators,” *J. Mater. Chem.*, Vol. 19, pp. 9260-9264, 2009.
- [1.89] S. H. Sun, G. W. Meng, G. X. Zhang, T. Gao, B. Y. Geng, L. D. Zhang, and J. Zuo, “Raman scattering study of rutile SnO<sub>2</sub> nanobelts synthesized by thermal evaporation of Sn powders,” *Chem. Phys. Lett.*, Vol. 376, pp. 103-107, 2003.
- [1.90] J. Zhou, L. Gong, S. Z. Deng, J. Chen, J. C. She, and N. S. Xu, “Growth and field-emission property of tungsten oxide nanotip arrays,” *Appl. Phys. Lett.*, Vol. 87, pp. 223108-1-3, 2005.
- [1.91] L. X. Zhao, G. W. Meng, X. S. Peng, X. Y. Zhang, and L. D. Zhang, “Synthesis, raman scattering, and infrared spectra of large-scale GaN nanorods,” *J. Cryst. Growth*, Vol. 235, pp. 124-128, 2002.
- [1.92] R. W. Wood, “A new form of cathode discharge and the production of x-rays, together with some notes on diffraction,” *Phys. Rev.*, Vol. 5, pp. 1-5, 1897.
- [1.93] R. H. Fowler, and L. W. Nordheim, “Electron emission in intense field,” *Proc. R. Soc. A*, Vol. 119, pp. 173-181, 1928.
- [1.94] C. Ye, Y. Bando, X. Fang, G. Shen, and D. Golberg, “Enhanced field emission performance of ZnO nanorods by two alternative approaches,” *J. Phys. Chem. C*, Vol. 111, pp. 12673-12676, 2007.
- [1.95] F. M. Charbonnier, W. A. Mackie, R. L. Hartman, and T. Xie, “Robust high current field emitter tips and arrays for vacuum microelectronic devices,” *J. Vac. Sci. Technol. B*, Vol. 19, pp. 1064-1072, 2001
- [1.96] C. J. Edgecombe, and U. Valdre, “Experimental and computational study of field emission characteristics from amorphous carbon single nanotips grown by

- carbon contamination I. Experiments and computation,” *Philos. Mag. B*, Vol. 82, pp. 987-1007, 2002.
- [1.97] V. Filip, D. Nicolasecu, M. Tanemura, and F. Okuyama, “Modeling the electron field emission from carbon nanotube films,” *Ultramicroscopy*, Vol. 89, pp. 39-49, 2001.
- [1.98] H. X. Tang, M. Yan, H. Zhang, S. Z. Li, X. F. Ma, M. Wang, and D. Yang, “A selective NH<sub>3</sub> gas sensor based on Fe<sub>2</sub>O<sub>3</sub>-ZnO nanocomposites at room temperature,” *Sensors Actuators B*, Vol. 114, pp. 910-915, 2006.
- [1.99] T. L. Barr, “An ESCA study of termination of the passivation of elemental metals,” *J. Phys. Chem.*, Vol. 82, pp. 1801-1810, 1978.
- [1.100] P. Esser, and W. Gopel, “Physical adsorption on single crystal zinc oxide,” *Surf. Sci.*, Vol. 97, pp. 309-318, 1980.
- [1.101] M. Batzill, and U. Diebold, “The surface and materials science of tin oxide,” *Prog. In Surf. Sci.*, Vol. 79, pp. 47-154, 2005.
- [1.102] J. F. Chang, H. H. Kuo, I. C. Leu, and M. H. Hon, “The effects of thickness and operation temperature ZnO:Al thin film CO gas sensor,” *Sens. Actuators B*, Vol. 84 pp. 258-264, 2002.
- [1.103] G. S. Trivikrama Rao, and D. Tarakarama Rao, “Gas sensitivity of ZnO based thick film sensor to NH<sub>3</sub> at room temperature,” *Sens. Actuators B*, Vol. 55 pp. 166-169, 1999.
- [1.104] D. A. Lamb, and S. J. C. Irvine, “Growth properties of thin film ZnO deposited by MOCVD with n-butyl alcohol as the oxygen precursor,” *J. Cryst. Growth*, Vol. 273, pp. 111-117, 2004.
- [1.105] S. Mridha, and D. Basak, “Investigation of a p-CuO/n-ZnO thin film heterojunction for H<sub>2</sub> gas-sensor applications,” *Semicond. Sci. Technol.*, Vol. 21, pp. 928-932, 2006.
- [1.106] Y. Jin, J. Wang, B. Sun, J. C. Blakesley, N. C. Greenham, “Solution-processed ultraviolet photodetectors based on colloidal ZnO nanoparticles,” *Nano Lett.*, Vol. 8, pp. 1649-1653, 2008.
- [1.107] W. W. Zhuang, W. Pan, B. D. Ulrich, J. J. Lee, L. Stecker, A. Burmaster, D. R. Evans, S. T. Hsu, M. Tajiri, A. Shimaoka, K. Inoue, T. Naka, N. Awaya, K. Sakiyama, Y. Wang, S. Q. Liu, N. J. Wu, and A. Ignatiev, “Novell colossal magnetoresistive thin film nonvolatile resistance random access memory (RRAM),” *IEDM Tech. Dig.*, pp. 193-196, 2002.
- [1.108] K. Kim, J. H. Choi, and H. S. Jeong, “The future prospect of nonvolatile memory,” *Proc. VLSI-TSA-Tech.*, pp. 88-94, 2005.
- [1.109] R. Moazzami, “Ferroelectric thin film technology for semiconductor memory,” *Semicond. Sci. Technol.*, Vol. 10, pp. 375-390, 1995.

- [1.110] J. M. Slaughter, R. W. Dave, M. Durlam, G. Kerszykowski, K. Smith, K. Nagel, B. Feil, J. Calder, M. DeHerrera, B. Garni, and S. Tehrani, "High speed toggle MRAM with MgO-based tunnel junctions," *IEDM Tech. Dig.*, pp. 873-876, 2005.
- [1.111] N. Yamada, E. Ohno, K. Nishiuchi, N. Akahira, and M. Takao, "Rapid-phasetransitions of GeTe-Sb<sub>2</sub>Te<sub>3</sub> pseudobinary amorphous thin films for an optical disk memory," *J. Appl. Phys.*, Vol. 69, pp. 2849-2856, 1991.
- [1.112] G. H. Buh, I. k Hwang, and B. H. Park, "Time-dependent electroforming in NiO resistive switching devices," *Appl. Phys. Lett.*, Vol. 95, p. 142101, 2009.
- [1.113] A. Odagawa, Y. Katoh, Y. Kanzawa, Z. Wei, T. Mikawa, S. Muraoka, and T. Takagi, "Eletroforming and resistance-switching mechanism in a magnetite thin film," *Appl. Phys. Lett.*, vol. 91, p. 133503, 2007.
- [1.114] M. H. Lin, M. C. Wu, C. H. Lin, and T. Y. Tseng, "Effects of vanadium doping on resistive switching characteristics and mechanisms of SrZrO<sub>3</sub>-based memory films," *IEEE Trans. Electron Device*, Vol. 57, pp. 1801-1808, 2010.
- [1.115] C. Y. Lin, C. Y. Wu, C. Y. Wu, and T. Y. Tseng, "Modified resistive switching behavior of ZrO<sub>2</sub> memory films based on the interface layer formed by using Ti top electrode," *J. Appl. Phys.*, Vol. 102, pp. 094101-1-4, 2007.
- [1.116] S. M. Sze, "Semiconductor Devices, Physics and Technology, 2<sup>nd</sup> edition, Wiley, New York, 2002.
- [1.117] M. N. Jung, J. E. Loo, S. J. Oh, B. W. Lee, W. J. Lee, S. H. Ha, Y. R. Cho, and J. H. Chang, "Influence of growth mode on the structural, optical, and electrical properties of In doped ZnO nanorods," *Appl. Phys. Lett.*, Vol. 94, pp. 041906-1-3, 2009.
- [1.118] S. Paresh, D. Yang, S. Emeato, A. John, and G. Pu-Xian, "Annealing induced nanostructure and photoluminescence property evolution in solution-processed Mg-alloyed ZnO nanowires," *Appl. Phys. Lett.*, Vol. 97, pp. 103104-1-3, 2010.

## **Chapter 2**

- [2.1] C. Y. Lee, S. Y. Li, P. Lin, and T. Y. Tseng, "Field -emission triode of low-temperature synthesixed ZnO nanowires," *IEEE Trans. On Nanotechnology*, Vol. 5, pp. 216-219, 2006.
- [2.2] K. P. Jayadevan, and T. Y. Tseng, "One-dimensional semiconductor nanostructures as absorber layers in solar cells," *J. Nanosci. & Nanotechnonlgy*, Vol. 5, pp. 1768-1784, 2005.
- [2.3] M. Law, L. E. Greene, J. C. Johnson, R. Saykally, and P. Yang, "Nanowire dye-sensitized solar cells," *Nat. Mate.*, Vol. 4, pp. 455-459, 2005.

- [2.4] S. Y. Li, C. Y. Lee, and T. Y. Tseng, "Copper-catalyzed ZnO nanowires on silicon (1 0 0) grown by vapor-liquid-solid process," *J. Cryst. Growth*, Vol. 247, pp. 357-362, 2003.
- [2.5] D. J. Lee, J. Y. Park, S. Y. Yun, S. Y. Hong, H. J. Moon, T. B. Lee, and S. S. Kim, "Comparative studies on the growth behavior of ZnO nanorods by metalorganic chemical vapor deposition depending on the type of substrates," *J. Cryst. Growth*, Vol. 276, pp. 458-464, 2005.
- [2.6] C. Y. Lee, S. Y. Li, P. Lin, and T. Y. Tseng, "ZnO nanowires hydrothermally grown on PET polymer substrates and their characteristics," *J. Nanosci. & Nanotechnology*, Vol. 5, pp. 1088-1094, 2005.
- [2.7] B. Y. Li, Y. Bando, and D. Golberg, "ZnO nanoneedles with tip surface perturbations: Excellent field emitters," *Appl. Phys. Lett.*, Vol. 84, pp. 3603-3605, 2004.
- [2.8] L. F. Dong, J. Jiao, D. W. Tuggle, J. M. Petty, S. A. Elliff, and M. Coulter, "ZnO nanopencils: Efficient field emitters," *Appl. Phys. Lett.*, Vol. 87, pp. 013110-1-3, 2005.
- [2.9] Q. Wan, K. Yu, T. H. Wang, and C. L. Lin, "Low-field electron emission from tetrapod-like ZnO nanostructures synthesized by rapid evaporation," *Appl. Phys. Lett.*, Vol. 83, pp. 2253-2255, 2003.
- [2.10] D. Banerjee, S. H. Jo, and Z. F. Ren, "Enhanced field emission of ZnO nanowires," *Adv. Mater.*, Vol. 16, pp. 2028-2032, 2004.
- [2.11] H. Zhang, D. R. Yang, X. T. Ma, and D. L. Que, "Synthesis and field emission characteristics of bilayered ZnO nanorod array prepared by chemical reaction," *J. Phys. Chem. B*, Vol. 109, pp. 17055-17059, 2005.
- [2.12] V. Filip, D. Nicolaescu, M. Tanemura, and F. Okuyama, "Modeling the electron field emission from carbon nanotube films," *Ultramicroscopy*, Vol. 89, pp. 39-49, 2001.
- [2.13] F. M. Charbonnier, W. A. Mackie, R. L. Hartman, and T. B. Xie, "Robust high current field emitter tips and arrays for vacuum microelectronics devices," *J. Vac. Sci. Technol B.*, Vol. 19, pp. 1064-1072, 2001.
- [2.14] J. P. Liu, C. X. Xu, G. P. Zhu, Y. P. Cui, Y. Yang, and X. W. Sun, "Hydrothermally grown ZnO nanorods on self-source substrate and their field emission," *J. Phys. D: Appl. Phys.*, Vol. 40, pp. 1906-1909, 2007.
- [2.15] C. J. Lee, T. J. Lee, S. C. Lyu, Y. Zhang, H. Ruh, and H. J. Lee, "Field emission from well-aligned zinc oxide nanowires grown at low temperature," *Appl. Phys. Lett.*, Vol. 81, pp. 3648-3650, 2002.

### **Chapter 3**

- [3.1] J. T. Hu, T. W. Odem, and C. M. Lieber, "Chemistry and physics in one dimension: synthesis and properties of nanowires and nanotubes," *Acc. Chem. Res.*, Vol. 32, pp. 435-445, 1999.
- [3.2] M. H. Huang, S. Mao, H. Feick, H. Yan, Y. Wu, H. Kind, E. Webber, R. Russo, and P. Yang, "Room-temperature ultraviolet nanowire nanolasers," *Science*, Vol. 292, pp. 1897-1899, 2001.
- [3.3] Z. H. Chen, Y. B. Tang, Y. Liu, G. D. Yuan, W. F. Zhang, J. A. Zapien, I. Bello, W. J. Zhang, C. S. Lee, and S. T. Lee, "ZnO nanowire arrays grown on Al:ZnO buffer layers and their enhanced electron field emission," *J. Appl. Phys.*, Vol. 106, pp. 064303-1-6, 2009.
- [3.4] C. C. Chuang, J. H. Huang, C. C. Lee, and Y. Y. Chang, "Fabrication and field emission characteristics of high density carbon nanotube microarrays," *J. Vac. Sci. Technol. B*, Vol. 23, pp. 772-775, 2005.
- [3.5] W. J. Zhang, Y. Wu, C. Y. Chan, W. K. Wang, X. M. Meng, I. Bello, Y. Lifshitz, and S. T. Lee, "Structuring single- and nano-crystalline diamond cones," *Diamond Relat. Mater.*, Vol. 13, pp. 1037-1043, 2004.
- [3.6] C. Y. Lee, M. P. Lu, K. F. Liao, W. W. Wu, and L. J. Chen, "Vertically well-aligned epitaxial Ni<sub>31</sub>Si<sub>12</sub> nanowire arrays with excellent field emission properties," *Appl. Phys. Lett.*, Vol. 93, pp. 113109-1-3, 2008.
- [3.7] C. Y. Lee, S. Y. Li, P. Lin, and T. Y. Tseng, "Field-emission triode of low-temperature synthesized ZnO nanowires," *IEEE Trans. On Nanotechnology*, Vol. 5, pp. 216-219, 2006.
- [3.8] C. Y. Lee, T. Y. Tseng, S. Y. Li, and P. Lin, "Electrical characterizations of a controllable field emission triode based on low temperature synthesized ZnO nanowires," *Nanotechnology*, Vol. 17, pp. 83-88, 2006.
- [3.9] L. F. Banerjee, S. H. Jo, and Z. F. Ren, "Enhanced field emission of ZnO nanowires," *Adv. Mater.*, Vol. 16, pp. 2028-2032, 2004.
- [3.10] Q. Wen, K. Yu, T. H. Wang, and C. L. Lin, "Low-field electron emission from tetrapod-like ZnO nanostructures synthesized by rapid evaporation," *Appl. Phys. Lett.*, Vol. 83, pp. 2253-2255, 2003.
- [3.11] I. C. Yao, P. Lin, and T. Y. Tseng, "Nanotip fabrication of zinc oxide nanorods and their enhanced field emission properties," *Nanotechnology*, Vol. 20, pp. 125202-1-5, 2009.
- [3.12] X. Qian, H. Liu, Y. Guo, Y. Song, and Y. Li, "Effect of aspect ratio on field emission properties of ZnO nanorod arrays," *Nanoscale Res. Lett.*, Vol. 3, pp. 303-307, 2008.
- [3.13] K. Vanhausden, W. L. Warren, C. H. Seager, D. R. Tallant, J. A. Voigt, and B. E. Gnade, "Mechanisms behind green photoluminescence in ZnO phosphor

- powders,” *J. Appl. Phys.*, Vol. 79, pp. 7983-7990, 1996.
- [3.14] Y. P. Wang, W. I. Lee, and T. Y. Tseng, “Degradation phenomena of multilayer ZnO–glass varistors studied by deep level transient spectroscopy,” *Appl. Phys. Lett.*, Vol. 69, pp. 1807-1809, 1996.
- [3.15] S. N. Bai, H. H. Tsai, and T. Y. Tseng, “Structural and optical properties of Al-doped ZnO nanowires synthesized by hydrothermal method,” *Thin Solid Films*, Vol. 516, pp. 155-158, 2007.
- [3.16] V. Filip, D. Nicolaescu, M. Tanemura, and F. Okuyama, “Modeling the electron field emission from carbon nanotube films,” *Ultramicroscopy*, Vol. 89, pp. 39-49, 2001.
- [3.17] F. M. Charbonnier, W. A. Mackie, R. L. Hartman, and T. B. Xie, “Robust high current field emitter tips and arrays for vacuum microelectronics devices,” *J. Vac. Sci. Technol B*, Vol. 19, pp. 1064-1073, 2001.
- [3.18] C. Kittel, *Introduction to Solid State Physics*, 8th ed. Hoboken: Wiley, 2004, pp. 590.

#### **Chapter 4**

- [4.1] S. Y. Li, P. Lin, C. Y. Lee, and T. Y. Tseng, “Field emission and photofluorescent characteristics of zinc oxide nanowires synthesized by a metal catalyzed vapor-liquid-solid process,” *J. Appl. Phys.*, Vol. 95, pp. 3711-3716, 2004.
- [4.2] T. D. Pounds, M. G. Norton, D. N. McIlroy, and L. Wang *Handbook of Nanoceramics and their based nanodevices*, edited by Tseng T Y and Nalwa H S, Am. Scientific Publishers, CA. USA, 2009, vol. 5, pp. 74.
- [4.3] I. C. Yao, P. Lin, and T. Y. Tseng, “Hydrogen gas sensors using ZnO-SnO<sub>2</sub> core-shell nanostructure,” *Adv. Sci. Lett.*, Vol. 3, pp. 548-553, 2010.
- [4.4] Z. L. Wang, “Zinc oxide nanostructures: growth, properties and applications,” *J. Phys.: Condens. Mater.*, Vol. 16, pp. R829-858, 2004.
- [4.5] Z. H. Chen, Y. B. Tang, Y. Liu, G. D. Yuan, W. F. Zhang, J. A. Zapien, I. Bello, W. J. Zhang, C. S. Lee, and S. T. Lee, “ZnO nanowire arrays grown on Al:ZnO buffer layers and their enhanced electron field emission,” *J. Appl. Phys.*, Vol. 106, pp. 064303-1-6, 2009.
- [4.6] S. S. Warule, N. S. Chaudhari, J. D. Ambekart, B. B. Kale, and M. A. More, “Hierarchical nanostructured ZnO with nanorods engendered to nanopencils and pin-cushion cactus with its field emission study,” *ACS Appl. Mater. Interfaces*, Vol. 3, pp. 3454-3462, 2011.
- [4.7] C. Li, Y. Di, W. Lei, Q. Yin, X. Zhang, and Z. Zhao, “Field emission from injector-like ZnO nanostructure and its simulation,” *J. Phys. Chem. C*, Vol. 112, pp. 13447-13449, 2008.



- [4.8] L. C. Chao, C. C. Liao, J. W. Lee, and F. C. Tsai, "Fabrication of zinc nanotip arrays by ion beam sputtering," *J. Vac. Sci. Technol. B*, Vol. 25, pp. 2168-2170, 2007.
- [4.9] J. Yoo, W. II Park, and G. C. Yi, "Electrical and optical characteristics of hydrogen-plasma treated ZnO nanoneedles," *J. Vac. Sci. Technol. B*, Vol. 23, pp. 1970-1974, 2005.
- [4.10] Q. Zhao, T. Cai, S. Wang, R. Zhu, Z. Liao, and D. Yu, "Enhanced near-band-edge emission and field emission properties from plasma treated ZnO nanowires," *Applied Physics A*, Vol. 100, pp. 165-170, 2010.
- [4.11] I. C. Yao, P. Lin, and T. Y. Tseng, "Nanotip fabrication of zinc oxide nanorods and their enhanced field emission properties," *Nanotechnology*, Vol. 20, pp. 125202, 2009.
- [4.12] T. Zhang, W. Dong, K. M. K. Brewer, S. Konar, R. N. Njabon, and Z. R. Tian, "Site-specific nucleation and growth kinetics in hierarchical nanosyntheses of branched ZnO crystallites," *J. Am. Chem. Soc.*, Vol. 128, 10960-10968, 2006.
- [4.13] Y. C. Chang, W. C. Yang, C. M. Chang, P. C. Hsu, and L. J. Chen, "Controlled growth of ZnO nanopagoda arrays with varied lamination and apex angles," *Cryst. Growth Des.*, Vol. 9, pp. 3161-3167, 2009.
- [4.14] V. Filip, D. Nicolaescu, M. Tanemura, and F. Okuyama, "Modeling the electron field emission from carbon nanotube films," *Ultramicroscopy*, Vol. 89, pp. 39-49, 2001.
- [4.15] X. Y. Kong, and Z. L. Wang, "Spontaneous polarization-induced nanohelices, nanosprings, and nanorings of piezoelectric nanobelts," *Nano Lett.*, Vol. 3, pp. 1625-1631, 2003.
- [4.16] K. Vanhausden, W. L. Warren, C. H. Seager, D. R. Tallant, J. A. Voigt, and B. E. Gnade, "Mechanisms behind green photoluminescence in ZnO phosphor powders," *J. Appl. Phys.*, Vol. 79, pp. 7983-7990, 1996.
- [4.17] F. M. Charbonnier, W. A. Mackie, R. L. Hartman, and T. B. Xie, "Robust high current field emitter tips and arrays for vacuum microelectronics devices," *J. Vac. Sci. Technol B*, Vol. 19, pp. 1064-1073, 2001.
- [4.18] L. Nilsson, O. Groening, C. Emmenegger, O. Kuettel, E. Schaller, L. Schlapbach, H. Kind, J. M. Bonard, and K. Kern, "Scanning field emission from patterned carbon nanotube films," *Appl. Phys. Lett.*, Vol. 76, pp. 2071-2073, 2000.

## Chapter 5

- [5.1] H. Hung, C. L. Lee, O. K. Tan, W. Zhou, N. Peng, and Q. Zhang, "High sensitivity SnO<sub>2</sub> single-nanorod sensors for the detection of H<sub>2</sub> gas at low temperature," *Nanotechnology*, Vol. 20, pp. 115501-1-5, 2007

- [5.2] Y. J. Chen, L. Nie, X. Y. Xue, Y. G. Wang, and T. H. Wang, "Linear ethanol sensing of SnO<sub>2</sub> nanorods with extremely high sensitivity," *Appl. Phys. Lett.*, Vol. 88, pp. 083105-1-3, 2006
- [5.3] O. K. Tan, W. Cao, W. Zhu, J. W. Chai, and J. S. Pan, "Ethanol sensors based on nano-sized  $\alpha$ -Fe<sub>2</sub>O<sub>3</sub> with SnO<sub>2</sub>, ZrO<sub>2</sub>, TiO<sub>2</sub> solid solutions," *Sensors Actuators B*, Vol. 93, pp. 396-401, 2003.
- [5.4] D. S. Zhang, H. X. Fu, L. Y. Shi, J. H. Fang, and Q. Li, "Carbon nanotube assisted synthesis of CeO<sub>2</sub> nanotubes," *J Solid State Chem.*, Vol. 180, pp. 654-660, 2007.
- [5.5] K. P. Kalyanikutty, M. Nikhila, U. Maitra, and C. N. R. Rao, "Hydrogel-assisted synthesis of nanotubes and nanorods of CdS, ZnS and CuS, showing some evidence for oriented attachment," *Chem. Phys. Lett.*, Vol. 432, pp. 190-194, 2006.
- [5.6] S. J. Chang, T. J. Hsueh, I. C. Chen, and B. R. Huang, "Highly sensitive ZnO nanowire CO sensors with the adsorption of Au nanoparticles," *Nanotechnology*, Vol. 19, pp. 175502-1-5, 2008.
- [5.7] T. Zhang, Y. Zeng, H. T. Fan, L. J. Wang, R. Wang, W. Y. Fu, and H. B. Yang, "Synthesis, optical and gas sensitive properties of large-scale aggregative flowerlike ZnO nanostructures via simple route hydrothermal process," *J. Phys. D: Appl. Phys.*, Vol. 42, pp. 045103-1-8, 2009.
- [5.8] D. S. Kang, S. K. Han, J. H. Kim, S. M. Yang, J. G. Kim, S. K. Hong, D. Kim, and H. Kim, "ZnO nanowires prepared by hydrothermal growth followed by chemical vapor deposition for gas sensors," *J. Vac. Sci. Technol. B*, Vol. 27, pp. 1667-1672, 2009.
- [5.9] X. F. Song, Z. J. Wang, Y. B. Liu, C. Wang, and L. J. Li, "A highly sensitive ethanol sensor based on mesoporous ZnO-SnO<sub>2</sub> nanofibers," *Nanotechnology*, Vol. 20, pp. 075501-1-5, 2009.
- [5.10] Q. Kuang, Z. H. Jiang, Z. X. Xie, S. C. Lin, Z. W. Lin, S. Y. Xie, R. B. Huang, and L. S. Zheng, "Tailoring the optical property by a three-dimensional epitaxial heterostructure: A case of ZnO/SnO<sub>2</sub>," *J. Am. Chem. Soc.*, Vol. 127, pp. 11777-11784, 2005.
- [5.11] K. M. Li, Y. J. Li, M. Y. Lu, C. I. Kuo, and L. J. Chen, "Direct conversion of single-layer SnO nanoplates to multi-Layer SnO<sub>2</sub> nanoplates with enhanced ethanol sensing properties," *Adv. Funct. Mater.*, Vol. 19, pp. 2453-2456, 2009.
- [5.12] M. S. Wagh, G. H. Jain, D. R. Patil, S. A. Patil, and L. A. Patil, "Modified zinc oxide thick film resistors as NH<sub>3</sub> gas sensor," *Sensors Actuators B*, Vol. 115, pp. 128-133, 2006.
- [5.13] V. S. Vaishnav, P. D. Patel, and N. G. Patel, "Indium Tin Oxide thin film gas



- sensors for detection of ethanol vapours ,” *Thin Solid Films*, Vol. 490, pp. 94-100, 2005.
- [5.14] S. W. Choi, J. Y. Park, and S. S. Kim, “Synthesis of SnO<sub>2</sub>-ZnO core-shell nanofibers via a novel two-step process and their gas sensing properties,” *Nanotechnology*, Vol. 20, pp. 465603-1-6 2009.
- [5.15] G. G. Hiang, C. T. Wang, H. T. Tang, Y. S. Huang, and J. Yang, “ZnO nanoparticle-modified infrared internal reflection elements for selective detection of volatile organic compounds,” *Anal. Chem.*, Vol. 78, pp. 2397-2404, 2006.
- [5.16] J. X. Wang, X. W. Sun, Y. Yang, H. Huang, Y. C. Lee, O. K. Tan, and L. Vayssieres, “Hydrothermally grown oriented ZnO nanorod arrays for gas sensing applications,” *Nanotechnology*, Vol. 17, pp. 4995-4998, 2006.
- [5.17] J. X. Wang, X. W. Sun, Y. Yang, and C. M. L. Wu, “N-P transition sensing behaviors of ZnO nanotubes exposed to NO<sub>2</sub> gas,” *Nanotechnology*, Vol. 20, pp. 465501-1-4, 2009.
- [5.18] W. Y. Wu, J. M. Ting, and P. J. Huang, “Electrospun ZnO nanowires as gas sensors for ethanol detection,” *Nanoscale Res. Lett.*, Vol. 4, pp. 513-517, 2009.
- [5.19] H. X. Tang, M. Yan, H. Zhang, S. Z. Li, X. F. Ma, M. Wang, and D. Yang, “A selective NH<sub>3</sub> gas sensor based on Fe<sub>2</sub>O<sub>3</sub>-ZnO nanocomposites at room temperature,” *Sensors Actuators B*, Vol. 114, pp. 910-915, 2006.
- [5.20] T. L. Barr, “An ESCA study of termination of the passivation of elemental metals,” *J. Phys. Chem.*, Vol. 82, pp. 1801-1810, 1978.
- [5.21] P. Esser, and W. Gopel, “Physical adsorption on single crystal zinc oxide,” *Surf. Sci.*, Vol. 97, pp. 309-318, 1980.
- [5.22] D. M. Wilson, S. Hoyt, J. Janata, K. Booksh, and L. Obando, “Chemical sensors for portable, handheld field instruments,” *IEEE Sensors J.*, Vol. 1, pp. 256-274, 2001.
- [5.23] M. Takata, D. Tsubone, and H. Yanagida, “Dependence of electrical conductivity of ZnO on degree of sintering,” *J. Amer. Ceram. Soc.*, Vol. 59, pp. 4-8, 1976.
- [5.24] Y. Chen, X. Y. Xue, Y. G. Wang, and T. H. Wang, “Synthesis and ethanol sensing characteristics of single crystalline SnO<sub>2</sub> nanorods,” *Appl. Phys. Lett.*, Vol. 87, pp. 233503-1-3, 2005.
- [5.25] E. Comini, G. Faglia, G. Sberveglieri, Z. W. Pan, and Z. L. Wang, “Stable and highly sensitive gas sensors based on semiconducting oxide nanobelts,” *Appl. Phys. Lett.*, Vol. 81, pp. 1869-1871, 2002.

## Chapter 6

- [6.1] C.Y. Lee, T.Y. Tseng, S.Y. Li, and P. Lin, “Electrical characterizations of a

- controllable field emission triode based on low temperature synthesized ZnO nanowires,” *Nanotechnology*, Vol. 17, pp. 83-88, 2006.
- [6.2] I. C. Yao, P. Lin, and T. Y. Tseng, “Nanotip fabrication of zinc oxide nanorods and their enhanced field emission properties,” *Nanotechnology*, Vol. 20, pp. 125202-1-5, 2009.
- [6.3] C. Y. Lee, J. Y. Wang, Y. Chou, C. L. Cheng, C. H. Chao, S. C. Shiu, S. C. Hung, J. J. Chao, M. Y. Liu, W. F. Su, and Y. F. Chen, “White-light electroluminescence from ZnO nanorods/polyfluorene by solution-based growth,” *Nanotechnology*, Vol. 20, pp. 425202-1-5, 2009.
- [6.4] I. C. Yao, P. Lin, and T. Y. Tseng, “Hydrogen gas sensors using ZnO-SnO<sub>2</sub> core-shell nanostructure,” *Adv. Sci. Lett.*, Vol. 3, pp. 548-553, 2010.
- [6.5] H. L. Porter, A. L. Cai, J. F. Muth, and J. Narayan, “Enhanced photoconductivity of ZnO films Co-doped with nitrogen and tellurium,” *Appl. Phys. Lett.*, Vol. 86, pp. 211918-1-3, 2005.
- [6.6] J. Suehiro, N. Nakagawa, S. I. Hidaka, M. Ueda, K. Imasaka, M. Higashihata, T. Okada, and M. Hara, “Dielectrophoretic fabrication and characterization of a ZnO nanowire-based UV photosensor,” *Nanotechnology*, Vol. 17, pp. 2567-2573, 2006.
- [6.7] J. B. K. Law, and T. L. Thong, “Simple fabrication of a ZnO nanowire photodetector with a fast photoresponse time,” *Appl. Phys. Lett.*, Vol. 88, pp. 133114-1-3, 2006.
- [6.8] H. Kind, H. Yan, B. Messer, M. Law, and P. Yang, “Nanowire ultraviolet photodetectors and optical switches,” *Adv. Mater.*, Vol. 14, pp. 158-160, 2002.
- [6.9] H. Huang, Y. C. Lee, and O. K. Tan, in Chapter 5, Handbook of nanoceramics and their based nanodevices, Vol. 5, edited by T. Y. Tseng, H. S. Nalwa, Stevenson Ranch, American Scientific Publishers, CA 2009.
- [6.10] A. Manekkathodi, M. Y. Lu, C. W. Wang, and L. J. Chen, “Direct growth of aligned zinc oxide nanorods on paper substrates for low-cost flexible electronics,” *Adv. Mater.*, Vol. 22, pp. 4059-4063, 2010.
- [6.11] Y. Jin, J. Wang, B. Sun, J. C. Blakesley, and N. C. Greenham, “Solution-processed ultraviolet photodetectors based on colloidal ZnO nanoparticles,” *Nano Lett.*, Vol. 8, pp. 1649-1653, 2008.
- [6.12] Y. K. Su, S. M. Peng, L. W. Ji, C. Z. Wu, W. B. Cheng, and C. H. Liu, “Ultraviolet ZnO nanorod photosensors,” *Langmuir*, Vol. 26, pp. 603-606, 2010.
- [6.13] C. Y. Lee, S. Y. Li, P. Lin, and T. Y. Tseng, “ZnO nanowires hydrothermally grown on PET polymer substrates and their characteristics,” *J. Nanosci. & Nanotech.*, Vol. 5, pp. 1088-1094, 2005.
- [6.14] K. Vanhausden, W. L. Warren, C. H. Seager, D. R. Tallant, J. A. Voigt, and

- B. E. Gnade, "Mechanisms behind green photoluminescence in ZnO phosphor powders," *J. Appl. Phys.*, Vol.79, pp. 7983-7990, 1996.
- [6.15] Y. P. Wang, W. I. Lee, and T. Y. Tseng, "Degradation phenomena of multilayer ZnO–glass varistors studied by deep level transient spectroscopy," *Appl. Phys. Lett.*, Vol. 69, pp. 1807-1809, 1996.
- [6.16] S. N. Bai, H. H. Tsai, and T. Y. Tseng, "Structured and optical properties of Al-doped ZnO nanowires synthesized by hydrothermal method," *Thin Solid Films*, Vol. 516, pp. 155-158, 2007.
- [6.17] C. W. Chen, K. H. Chen, C. H. Shen, A. Ganguly, L. C. Chen, J. J. Wu, H. I. Wen, and W. F. Pong, "Anomalous blueshift in emission spectra of ZnO nanorods with sizes beyond quantum confinement regime," *Appl. Phys. Lett.*, Vol. 88, pp. 241905-1-3, 2006.
- [6.18] Handbook of Chemistry and Physics, 61<sup>st</sup> edition (CRC Press, Florida, 1981).
- [6.19] K. Keem, H. Kim, G. Kim, J. Lee, B. Min, K. Cho, M. Sung, and S. Kim, "Photocurrent in ZnO nanowires grown from Au electrodes," *Appl. Phys. Lett.*, Vol. 84, pp. 4376-4378, 2004.
- [6.20] C. Soci, A. Zhang, B. Xiang, S. A. Dayeh, D. P. R. Aplin, J. Park, X. Y. Bao, Y. H. Lo, and D. Wang, "ZnO nanowire UV photodetectors with high internal gain," *Nano Lett.*, Vol. 7, pp. 1003-1009, 2007.
- [6.21] D. H. Wilson, S. Hoyt, J. Janata, K. Booksh, and L. Obando, "Chemical sensors for portable, handheld field instruments," *IEEE sensors*, Vol. 1, pp. 256-274, 2001.
- [6.22] H. Wang, S. Baek, J. Song, J. Lee, and S. Lim, "Microstructural and optical characteristics of solution-grown Ga-doped ZnO nanorod arrays," *Nanotechnology*, Vol. 19, pp. 075607-1-6, 2008.
- [6.23] W. Yen, N. Mechau, H. Hahn, and R. Krupke, "Ultraviolet photodetector arrays assembled by dielectrophoresis of ZnO nanoparticles," *Nanotechnology*, Vol. 21, pp. 115501-1-7, 2010.
- [6.24] N. Chantarat, Y. W. Chen, S. Y. Chen, and C. C. Lin, "Enhanced UV photoresponse in nitrogen plasma ZnO nanotubes," *Nanotechnology*, Vol. 20, pp. 395201-1-5, 2009.
- [6.25] J. Cheng, Y. Zhang, and R. Guo, "ZnO microtube ultraviolet detectors," *J. Cryst. Growth*, Vol. 310, pp. 57-61, 2008.
- [6.26] C. C. Lin, W. H. Lin, and Y. Y. Li, "Synthesis of ZnO nanowires and their applications as an ultraviolet photodetector," *J. Nanosci. & Nanotech.*, Vol. 9, pp. 2813-2819, 2009.
- [6.27] Y. Li, X. Dong, C. Cheng, X. Zhou, P. Zhang, J. Gao, and H. Zhang,

“Fabrication of ZnO nanorod array-based photodetector with high sensitivity to ultraviolet,” *Physica B*, Vol. 404, pp. 4282-4285, 2009.

[6.28] D. Park, and K. Yong, “Photoconductivity of vertically aligned ZnO nanoneedle array,” *J. Vac. Sci. Technol. B*, Vol. 26, pp. 1933-1936, 2008.

## **Chapter 7**

[7.1] C. Y. Lin, C. Y. Wu, C. Y. Wu, T. C. Lee, F. L. Yang, C. Hu, and T. Y. Tseng, “Effect of top electrode material on resistive switching properties of ZrO<sub>2</sub> film memory devices,” *IEEE Electron Device Lett.*, Vol. 28, pp. 366-368, 2007.

[7.2] Q. Liu, S. Long, W. Wang, Q. Zuo, S. Zhang, J. Chen, and M. Liu, “Improvement of resistive switching properties in ZrO<sub>2</sub>-based ReRAM with implanted Ti ions,” *IEEE Electron Device Lett.*, Vol. 30, pp. 1335-1337, 2009.

[7.3] C. Y. Lin, C. Y. Wu, C. Y. Wu, T. Y. Tseng, and C. Hu, “Modified resistive switching behavior of ZrO<sub>2</sub> memory films based on the interface layer formed by using Ti top electrode,” *J. Appl. Phys.*, Vol. 102, pp. 094101-1-5, 2007.

[7.4] S. Y. Wang, D. Y. Lee, T. Y. Tseng, and C. Y. Lin, “Effects of Ti top electrode thickness on the resistive switching behaviors of rf-sputtered ZrO<sub>2</sub> memory films,” *Appl. Phys. Lett.*, Vol. 95, pp. 112904-1-3, 2009.

[7.5] M. C. Wu, Y. W. Lin, W. Y. Jang, C. H. Lin, and T. Y. Tseng, “Low-power and highly reliable multilevel operation in ZrO<sub>2</sub> 1T1R RRAM,” *IEEE Electron Device Lett.*, Vol. 32, pp. 1026-1028, 2011.

[7.6] D. Panda, A. Dhar, and S. K. Ray, “Nonvolatile memristive switching characteristics of TiO<sub>2</sub> films embedded with nickel nanocrystals,” 2011 *IEEE Trans. Nanotech.*, Vol. 11, pp. 51-55, 2011.

[7.7] K. M. Kim, B. J. Choi, D. S. Jeong, C. S. Hwang, and S. Hun, “Influence of carrier injection on resistive switching of TiO<sub>2</sub> thin films with Pt electrodes,” *Appl. Phys. Lett.*, Vol. 89, pp. 162912-1-3, 2006.

[7.8] B. J. Choi, S. Choi, K. M. Kim, Y. C. Shin, C. S. Hwang, S. Y. Hwang, S. S. Cho, S. Park, and S. K. Hong, “Study on the resistive switching time of TiO<sub>2</sub> thin films,” *Appl. Phys. Lett.*, Vol. 89, pp. 012906-1-3, 2006.

[7.9] A. Sawa, T. Fujii, M. Kawasaki, and Y. Tokura, “Hysteretic current–voltage characteristics and resistance switching at a rectifying Ti/Pr<sub>0.7</sub>Ca<sub>0.3</sub>MnO<sub>3</sub> interface,” *Appl. Phys. Lett.*, Vol. 85, pp. 4073-4075, 2004.

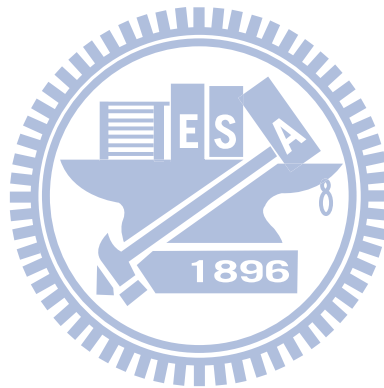
[7.10] M. H. Lin, M. C. Wu, C. H. Lin, and T. Y. Tseng, “Resistive switching characteristics and mechanisms of Pt-embedded SrZrO<sub>3</sub> memory devices,” *J. Appl. Phys.*, Vol. 107, pp. 124117-1-4, 2010.

[7.11] M. H. Lin, M. C. Wu, C. H. Lin, and T. Y. Tseng, “Effect of vanadium doping on resistive switching characteristics and mechanism of SrZrO<sub>3</sub>-based

- memory films,” *IEEE Trans. Electron Device*, Vol. 57, pp. 1801-1808, 2010.
- [7.12] N. Xu, L. F. Liu, X. Sun, Y. Wang, D. D. Han, X. Y. Liu, R. Q. Han, J. F. Kang, and B. Yu, “Bipolar switching behavior in TiN/ZnO/Pt resistive nonvolatile memory with fast switching and long retention,” *Semicond. Sci. Technol.*, Vol. 23, pp. 075019, 2008.
- [7.13] M. C. Chen, T. C. Chang, C. T. Tsai, S. Y. Hung, S. C. Chen, C. W. Hu, M. S. Simon, and M. J. Tsai, “Influence of electrode material on the resistive memory switching property of indium gallium zinc oxide thin films.” *Appl. Phys. Lett.*, Vol. 96, pp. 262110-1-3, 2010.
- [7.14] D. Panda, A. Dhar, and S. K. Ray, “Nonvolatile and unipolar resistive switching characteristics of pulsed laser ablated NiO films,” *J. Appl. Phys.*, Vol. 108, pp. 104513-1-7, 2010.
- [7.15] W. Y. Chang, C. A. Lin, J. H. He, and T. B. Wu, “Resistive switching behaviors of ZnO nanorod layers,” *Appl. Phys. Lett.*, Vol. 96, pp. 242109-1-3, 2010.
- [7.16] Y. Yang, J. Qi, W. Guo, Z. Zin, and Y. Zhang, “Electrical bistability and negative differential resistance in single Sb-doped ZnO nanobelts/SiO<sub>x</sub>/p-Si heterostructured devices,” *Appl. Phys. Lett.*, Vol. 96, pp. 093107-1-3, 2010.
- [7.17] Z. L. Tseng, P. C. Kao, M. F. Shih, H. H. Huang, J. Y. Wang, and S. Y. Chu, “Electrical bistability in hybrid ZnO nanorod/polymethylmethacrylate heterostructures,” *Appl. Phys. Lett.*, Vol. 97, pp. 212103-1-3, 2010.
- [7.18] C. Y. Lee, T. Y. Tseng, S. Y. Li, and P. Lin, “Single-crystalline Mg<sub>x</sub>Zn<sub>1-x</sub>O (0 ≤ x ≤ 0.25) nanowires on glass substrates obtained by a hydrothermal method: growth, structure and electrical characteristics,” *Nanotechnology*, Vol. 16, pp. 1105, 2005.
- [7.19] K. Vanhausden, W. L. Warren, C. H. Seager, D. R. Tallant, J. A. Voigt, and B. E. Gnade, “Mechanisms behind green photoluminescence in ZnO phosphor powders,” *J. Appl. Phys.*, Vol. 79, pp. 7983-7990, 1996.
- [7.20] Y. P. Wang, W. I. Lee, and T. Y. Tseng, “Degradation phenomena of multilayer ZnO–glass varistors studied by deep level transient spectroscopy,” *Appl. Phys. Lett.*, Vol. 69, pp. 1807-1809, 1996.
- [7.21] C. Y. Lin, B. C. Tu, C. C. Lin, C. H. Lin, and T. Y. Tseng, “Resistive switching mechanism of V-doped SrZrO<sub>3</sub> memory films,” *IEEE Electron Device Lett.*, Vol. 27 725-727, 2006
- [7.22] Kim D. C., Seo S., Ahn S. E., Suh D. S., Lee M. J., Park B. H., Yoo I. K., Beak I. G., Kim H. J., Yim E. K., Lee J. E., Park S. O., Kim H. S., Chung U. I., Moon J. T., and Ryu B. I., “Electrical observations of filamentary conduction for the resistive memory switching in NiO films,” *Appl. Phys. Lett.*, Vol. 88, pp.

202102-1-3, 2006.

- [7.23] S. S. Zumdahl 1998 *Chemical Principle*, 3<sup>rd</sup> ed. New York: Houghton Mifflin.
- [7.24] H. J. Wan, P. Zhou, L. Ye, and Y. Y. Lin, “Retention-failure mechanism of TaN/Cu<sub>x</sub>O/Cu resistive memory with good data retention capability,” *J. Vac. Sci. Technol. B*, Vol. 27, pp. 2468-2471, 2009.
- [7.25] S. Yu, and H. S. Philip Wong, “A phenomenological model for the reset mechanism of metal oxide RRAM,” *IEEE Electron Device Lett.*, Vol. 31, pp. 1455-1457, 2010.



# Vita

## 【Personal information】

- Name: 姚奕全 / Yao I-Chuan
- Gender: Male
- Date of birth: 1983/07/16
- Nationality: Taiwan (R.O.C)
- Email: penny07161616@yahoo.com.tw

## 【Education】

Degree	Name of School / Major	From	To	Research Advisor
Ph.D	National Chiao Tung University Materials Science and Engineering	Sep. 2007	Apr. 2012	Tseung-Yuen Tseng and Pang Lin
MS	National Taipei University of Technology Materials and Mineral Resources Engineering	Sep. 2005	Jun. 2007	Tseung-Yuen Tseng
BS	National Formosa University Materials Science and Engineering	Sep. 2003	Jun. 2005	
BS	National Hu-wei Institute of Technology Mechanical materials engineering	Sep. 1998	Jun. 2003	

## 【Expertise】

- One dimensional ZnO nanostructure
- Field emission characteristics
- Surface/Physical/Electrical analyses.

## 【Experience】

### ✚ Instrumental assistant:

- FIB/SEM dual guns system in Nano Facility Center of NCTU (2009-2012).
- FETEM (JEOL-2100F) in Nanoscience and Technology Center of NCTU (2009-2012).
- TEM (JEOL-2010) in Nanoscience and Technology Center of NCTU (2009-2012).





# Publications List

## ✚ Thesis of Master degree

非鉛系鈦酸鈹鈉基陶瓷 A、B 位取代對鐵電壓電性能之影響

Study of ferroelectric and piezoelectric properties of  $(\text{Bi}_{0.5}\text{Na}_{0.5})\text{TiO}_3$ -based lead-free ceramics by different substitution in A-site or B-site

## ✚ Dissertation of Ph.D degree

一維氧化鋅奈米結構製備及其應用

Synthesis of one dimensional zinc oxide nanostructure and their applications

## ✚ International journal papers

- **I-Chuan Yao**, Pang Lin and Tseung-Yuen Tseng, “Nanotip fabrication of zinc oxide nanorods and their enhanced field emission properties,” *Nanotechnology*, Vol. 20, pp. 125202-1-5, 2009.
- **I-Chuan Yao**, Pang Lin and Tseung-Yuen Tseng, “Hydrogen gas sensors using ZnO-SnO<sub>2</sub> core-shell nanostructure,” *Advanced Science Letters*, Vol. 3, pp. 548-553, 2010.
- **I-Chuan Yao**, Pang Lin and Tseung-Yuen Tseng, “ZnO nanowires grown on polymer substrates as UV photosensors,” *Sensors and Actuators A: Physical*, Vol. 178, pp. 26-31, 2012.
- **I-Chuan Yao**, Dai-Ying Lee, Tseung-Yuen Tseng and Pang Lin, “Fabrication and resistive switching characteristics of high compact Ga-doped ZnO nanorod thin film devices,” *Nanotechnology*, Vol. 23, pp. 145201-1-8, 2012.
- **I-Chuan Yao**, Pang Lin, Sheng-He Huang and Tseung-Yuen Tseng,

“Electrical properties and reliability of ZnO-based nanorod current emitters,”  
*IEEE Transactions on Components, Packaging and Manufacturing Technology*, Accepted.

- **I-Chuan Yao**, Pang Lin and Tseung-Yuen Tseng, “Field emission properties and reliability of ZnO nanorod, nanopagoda, and nanotip current emitters,”  
*IEEE Transactions on nanotechnology*, Accepted.
- Dai-Ying Lee, **I-Chuan Yao** and Tseung-Yuen Tseng, “Bottom electrode modification of ZrO<sub>2</sub> resistive switching memory device with Au nanodots,”  
*Japanese Journal of Applied Physics*, Accepted.
- **Yi-Quan Yao**, Tseung-Yuen Tseng, Chen-Chia Chou and Haydn H. D. Chen, “Phase transition and piezoelectric property of (Bi<sub>0.5</sub>Na<sub>0.5</sub>)<sub>0.94</sub>Ba<sub>0.06</sub>Zr<sub>y</sub>Ti<sub>1-y</sub>O<sub>3</sub> (y=0–0.04) ceramics,” *Journal of Applied Physics*, Vol. 102, pp. 094102, 2007.

#### International Conference

- **I-Chuan Yao**, Pang Lin and Tseung-Yuen Tseng, “Field emission properties of zinc oxide nanorods grown on ZnO/Si substrates by using plasma treatment” **2009** International Conference on Metallurgical Coating and Thin Films.
- **I-Chuan Yao**, Pang Lin and Tseung-Yuen Tseng, “Controllable synthesis of well-ordered ZnO nanorod arrays by nanosphere lithography and their field emission properties” **2010** International Conference on Metallurgical Coating and Thin Films.
- **I-Chuan Yao**, Tseung-Yuen Tseng and Pang Lin, “Characterizations of ZnO-CeO<sub>2</sub> core-shell nanostructures grown by hydrothermal method” **2010** 218th Electrochemical Society (ECS) Meeting.
- C. Y. Huang, **I-Chuan Yao**, M. Lin, Pang Lin, and Tseung-Yuen Tseng, “Improvements of resistive switching properties of Pt/ZrO<sub>2</sub>/Pt device using pyramid-like metal array” **2010** 218th Electrochemical Society (ECS) Meeting.
- **I-Chuan Yao**, Tseung-Yuen Tseng and Pang Lin, “Field emission and optical properties of sharp zinc oxide nanorods by oxygen plasma treatment” **2011** 220th Electrochemical Society (ECS) Meeting.

## Local Conference

- 陳映璉, 姚奕全, 顏宏全, 曾俊元, 林鵬, “不同蝕刻方式對氧化鋅奈米陣列之場發射特性之研究,” 2008年材料年會.
- 楊千蕙, 顏宏全, 姚奕全, 曾俊元, 林鵬, “濕式蝕刻氧化鋅奈米柱陣列之研究,” 2008年 材料年會.

## Patent

- 曾俊元, 姚奕全, 顏宏全, 林鵬, 周明德, 莫啟能: 用以製備氧化鋅奈米柱陣列場發射組件的方法. 深圳華映顯示科技有限公司, 中華映管股份有限公司. Apr, 20 2011: CN102024637.

